# Reduction of Computational Complexity and Hardware Implementation of Restoration Based Algorithm for Weather Degraded Images and Videos

**THESIS**

Submitted in partial fulfilment

of the requirements for the degree of

**DOCTOR OF PHILOSOPHY**

by

**APURVA KUMARI**

**ID. No. 2012PHXF532H**

Under the Supervision of

**Prof. SUBHENDU KUMAR SAHOO**


**BIRLA INSTITUTE OF TECHNOLOGY AND SCIENCE - PILANI HYDERABAD CAMPUS**

**2016**

**BIRLA INSTITUTE OF TECHNOLOGY AND SCIENCE -**

**PILANI HYDERABAD CAMPUS**

# CERTIFICATE

This is to certify that the thesis entitled, Reduction of Computational Complexity and Hardware Implementation of Restoration Based Algorithm for Weather Degraded Images and Videos and submitted by APURVA KUMARI ID No. 2012PHXF532H for award of Ph.D. of the institute embodies original work done by her under my supervision.

---

*Supervisor*

Prof. SUBHENDU KUMAR SAHOO

Associate Professor,

BITS-Pilani, Hyderabad Campus

Date:

# Acknowledgements

As I am reaching the end of a long journey with ups and downs. I wish to acknowledge the remarkable individuals who stood with me in my ups and downs. I want to give thanks to God for sustaining me and guiding me through this arduous journey.

At an outset, I would like to express my deep sense of gratitude and thanks to **Prof. Subhendu Kumar Sahoo**, my thesis supervisor. I will always be indebted to him for his valuable guidance and constant encouragement.

I am indebted to **Prof. Souvik Bhattacharyya**, Vice-Chancellor, **Prof. G Sundar**, Director, **Prof. Vidya Rajesh**, Associate Dean, Academic Research Division, BITS Pilani, Hyderabad Campus for giving me an opportunity to carry out research at the Institute.

I would like to thank my Doctoral Advisory Committee members, **Prof. BVVSN Prabhakar Rao** and **Dr. Prasant Kumar Pattnaik** for their inspiring support and invaluable scientific suggestions from time to time. They always extended helpful hands towards me whenever I needed them.

My sincere thanks to **Prof. Y. Yoganandam**, Head of department Electrical & Electronics Engineering, BITS Pilani, Hyderabad campus, for his encouragement, and moral support during various phases of research work.

I express my sincere thanks to all the faculty members of Electrical & Electronics Engineering, BITS Pilani, Hyderabad campus for their kind help and encouragement in carrying out my research work.

I would like to thank **Dr. Chandra Shekhar**, Director CSIR-CEERI Pilani and **Mr. Raj Singh**, Group Leader, IC Design Group, and **Dr. Ravi Saini** for their support and invaluable scientific suggestions from time to time.

Constant moral support extended to me by my friends and well wishers are gratefully acknowledged. I have a special word of thanks for my friends **Shivani** and **Priyanka** for their love and support. I am really fortunate for sharing a wonderful friendship with them. Writing this thesis would be extremely difficult for me without their enormous support. I gratefully acknowledge the support of my labmates during the different phases of my doctoral research work. I want to thank **Mr. G. Ganesh Kumar** for his kind support during my research work. I would like to thank **Ms. Poorna Lakshmi U** and **Mr. Balasubramanian M.** for their valuable suggestion during my thesis writing. I want to thank to the students who involved in the projects of this area.

Financial assistance from BITS Pilani, Hyderabad is gratefully acknowledged. I appreciate the unending love and affection from my sisters and sister in law, **Anamika**, **Asmita**, **Ankita** and my brother and brother in law, **Ashwini**, **Rajesh Ranjan** and my sister daughter **Aanya**. Love you all for your everlasting supports extended towards me.

Words are inadequate to express thanks and appreciation to my husband, **Varun** for all his love and support when I was irritable and depressed. His patience and sacrifice will remain my inspiration throughout my life.

My heart felt regard goes to mother in law and my father in law, **Sh. B. B. Singh** and **Smt. Shashi Singh** for their love and moral support. Last but not the least, the undying love and sacrifice of my parents, **Sh. Arvind Pratap Singh** and **Smt. Sumitra Devi**, can never be completely expressed with words alone. They have given up many things for me. I have no phrases to praise them. Their blessings have helped me in reaching this goal.

**Apurva Kumari**

# Abstract

Imaging in poor weather is often severely degraded by scattering due to suspended particles in the atmosphere such as haze and fog. Haze and fog are typical phenomena caused by minute aerosol particles and tiny water droplets suspended in the air. In a foggy and hazy scene, visible light is subjected to scattering, refraction and absorption. The presence of this haze and fog leads to considerable distortion of the scene, thereby reducing its visibility drastically at times. Hence defogging and dehazing is highly required for computer vision systems.

But haze and fog removal is a quite challenging problem due to its mathematical uncertainty, typically when the input is only a single image. Most recently, researchers have concentrated on the real-time approaches for removing fog and haze from image/video. However, these approaches fail to maintain a good tradeoff between the perceptual quality and the real-time processing. Real-time image/video deweathering algorithm is important for many applications such as surveillance systems, intelligent vehicles, remote sensing and driver assistance systems. A real-time deweathering algorithm has a big advantage for road sign recognition and lane marking. Development of road sign recognition and lane marking in real-time can be used by camera based driver assistance system that assist the driver to navigate vehicle by providing road signs and lane marking information. This also can be embedded into an unmanned vehicle. These systems must be robust to any change of weather conditions. This robustness can be achieved by using a deweathering system as preprocessing unit.

Accordingly, in this thesis we present an effective method for removing haze and fog from image/video which is also suitable for real-time processing. In this work, we discuss the problems encountered when considering the contrast enhancements for fog and haze removal. We present a new fog and haze removal method based on enhancement technique. Here, we have used gamma correction using look-up-table method. The use of look-up-table (LUT) in these

images/videos makes our approach appreciably faster. We extend the static image to real-time video deweathering.

Next, we provide an analysis and method based on physical models to observe how physical characteristics affect the quality of image/video. For improving the contrast and color, we have presented new restoration based techniques that utilize the estimation of atmospheric light and transmission map. We have presented a combination of thresholding and median dark channel prior based method for estimating and refining the atmospheric light and transmission map.

We have proposed a novel and simple restoration-based approach for accurately and effectively estimating the transmission depth. The transmission map has been refined using gamma transformation and for smoothening, median filtering is used. Among them, we have chosen the best restoration based technique which removes the artifacts and maintains the perceptual quality of the image/video. And finally, we have designed a hardware implementation of this restoration method which verifies the suitability of real-time deweathering. The design consists of 9-stage pipelined hardware accelerator which can obtain real-time performance.

# Contents

# List of Figures

# List of Tables

# Chapter 1

# Introduction

Research in the area of image processing and computer vision began almost 60 years ago. Computer graphics and computer vision techniques deal with observing and understanding the visual world around us, which is a multidisciplinary research program with a wide spectrum of applications that can impact our daily lives. With the expansion of CCD (Charged Coupled Device) techniques, today cameras are ubiquitous and the amount of images and videos generated is immense. Fields which traditionally used analog imaging are now switching to digital systems, for their affordability and flexibility. Important examples are film and video production, photography, security monitoring and underwater imaging. These and other sources produce huge volumes of digital image data every day, more than could ever be examined manually. So, computer based processing is adopted in many applications like remote sensing, intelligent vehicles, object recognition and surveillance systems.

Computer vision systems work in two types of environment indoor and outdoor. Indoor environments offer greater control of parameters such as scene light and depth maps. Also, they are immune to the effects of weather degradations. Indoor image processing applications such as image retrieval and automatic event detection systems based on image enhancement techniques

give acceptable results with minimum processing time. Therefore, computer vision systems have enjoyed great success in real time processing for indoor environments. Outdoor environments are susceptible to many natural conditions such as ambient light and weather conditions. This translates to greater uncertainity in scene light and depth maps. Therefore image enhancement based techniques have lower reliability for computer vision systems in outdoor environments. This is because enhancement based techniques are not based on mathematical analyses and do not account for unknown depth discontinuities in the scene. Image restoration based techniques give better perceptual image quality but at the cost of large processing time. Hence, unfortunately most computer vision systems have not enjoyed success when deployed in uncontrolled real time outdoor environments.

Studies on improving vision in a bad weather conditions began in the late 90s. Bad weather conditions such as fog, haze and rain greatly reduce the visual quality of outdoor systems. The performance of outdoor systems such as object detection, obstacle detection and video surveillance are adversely affected by the bad weather conditions. As an example for application of an outdoor surveillance system, vehicle driving can be considered. These systems are to assist in providing safest and least stressful driving. The tremendous growth in processing power has enabled the application of computer vision systems for real-time application. The camera based systems used in vehicle driving can automatically detect the critical situations and inform drivers to avoid accidents or to reduce their extremity. However, these systems are easily influenced by bad weather conditions.

Therefore, clear visibility is essential for these systems. In fact, most of the current vision systems are also designed to perform well with clear visibility. So, the poor visibility is a major challenge for many applications of computer vision. It is greatly influenced by the characteristics of light, such as its intensity and color. Intensity and color are altered by its interactions with the atmosphere. These interactions can be broadly classified into three categories, namely, scattering,

TABLE 1.1: **Weather conditions and associated particle types, sizes and concentrations [1]**

| **Condition** | **Particle Type** | **Radius($\mu$m)** | **Concentration** ($cm^{-3}$) |
|---|---|---|---|
| Air | Molecule | $10^{-4}$ | $10^{9}$ |
| Haze | Aerosol | $10^{-2} - 1$ | $10^{3} - 10$ |
| Fog | Water Droplet | $1 - 10$ | $100 - 10$ |
| Cloud | Water Droplet | $1 - 10$ | $300 - 10$ |
| Rain | Water Drop | $10^{2} - 10^{4}$ | $10^{-2} - 10^{-5}$ |

absorption and emission. Scattering is most significant factor in the case of poor visibility. In general, the exact nature of scattering is highly complex and depends on the types, orientations, sizes and distributions of the particles constituting the atmosphere. Weather conditions differ mainly in the types and sizes of the particles involved and their concentrations in space. Table 1.1 shows the weather conditions and associated particle types, sizes and concentrations [1, 2]. Fig. 1.1 shows 3 images of the same scene captured under different bad weather conditions. Based on the type of the visual effects, bad weather conditions are broadly classified into two categories: Steady and dynamic. In steady bad weather, constituent droplets are very small. Fog and haze are examples of steady weather. In dynamic bad weather, constituent droplets are 1000 times larger than those of the steady weather. Rain and snow represent dynamic weather conditions. Clouds are of less relevance to us as we restrict ourselves to vision at ground level rather than high altitudes. Larger particles produce a variety of weather conditions which we will briefly describe below.


FIGURE 1.1: Images at different bad weather conditions

**Haze:** Haze is constituted of aerosol which is a dispersed system of small particles suspended in gas. Haze has a diverse set of sources including volcanic ashes, foliage exudations, combustion products, and sea salt [3]. The particles produced by these sources respond quickly to changes in relative humidity and act as nuclei (centers) of small water droplets when the humidity is high. Haze particles are larger than air molecules but smaller than fog droplets. Haze tends to produce a distinctive gray hue and is certain to effect visibility.

**Fog:** Fog evolves when the relative humidity of an air parcel approaches a saturation level. Then, some of the nuclei grow by condensation into water droplets. Hence, fog and haze have similar origins and an increase in humidity is sufficient to turn haze into fog. This transition is quite gradual and an intermediate state is referred to as mist. While perceptible haze extends to an altitude of several miles, fog is typically just a few hundred feet thick. A practical distinction between fog and haze lies in the greatly reduced visibility induced by the former. There are many types of fog which differ from each other in their formation processes [4].

**Cloud:** A cloud differs from fog only in existing at high altitudes (troposphere) rather than sitting at ground level. While most clouds are made of water droplets like fog, some are composed of long ice crystals and ice-coated dust grains. Details on the physics of clouds and precipitation can be found in [5].

**Rain:** The process by which cloud droplets turn to rain is a complex one [5]. When viewed up close, rain causes random spatial and temporal variations in images and hence must be dealt with differently from the more stable weather conditions.

The impact of steady bad weather on images is relatively spatially consistent, and usually it leads to loss of image/video contrast and color fidelity. The resulting effect is that many image details are lost or hardly visible. When the light of scene travels to the camera, it can interact with the atmosphere. These interactions can change the characteristics of light, such as intensity

and color. These interactions can be classified into scattering, absorption and emission. Emission, which is negligibly small at optical wavelengths, is neglected. Scattering due to suspended particles is the most pertinent problem.

The image taken with the camera is actually composed by two scattering phenomenon, i.e., attenuation and the airlight. The light beam coming from a scene point gets attenuated because of scattering by atmospheric particles, called attenuation that decreases the contrast of the scene. The attenuation of luminance through the atmosphere was studied by koschmieder [6] who derived an equation relating to apparent luminance under bad weather conditions. The light coming from a source is scattered towards camera and leads to a shift in color which is called airlight. The fog and haze effect is the function of the distance between scene point and camera. The depth information of any foggy and hazy image is measured in terms of airlight and scene depth. If scene depth is known, then the problem of removing fog and haze becomes much easier.

However, image/video dehazing and defogging is a challenging problem because fog and haze are dependent on an unknown scene depth. A traditional image processing techniques such as histogram-based dehazing methods [7–9] have been developed for restoring the scene from the hazy and foggy images. However, these techniques are not appropriate for restoring the scene, because a single hazy and foggy image can barely produce much information. A number of methods have been presented for removing haze and fog from images. But most of the methods that rely on additional information include: multiple foggy and hazy images of the same scene under different weather conditions or different degrees of polarization by rotating polarizing filters attached to a camera. However, this is time consuming process for attaining enough images during rapid changes in the scene.

Recently, significant progresses have been made in single image haze and fog removal based on the physical model. Some single image based algorithms are physically valid and are able to improve the visibility in the presence of bad weather conditions. Although aforementioned approaches can enhance the image contrast, these methods have demonstrated some drawbacks that reduce their practical applicability. Generally, all algorithms have a problem with preserving color fidelity. So enhancement of foggy and hazy images and videos are a challenge due to the complexity in recovering the luminance and chrominance while maintaining the color fidelity. However, typically these methods take 5 to 7 min and 10 to 20 s of processing time with Intel Pentium Dual-Core Processor for image size $600 \times 400$. Therefore, this is also not suitable for real-time applications. To apply these methods for real-time applications hardware accelerator have to be designed which is a tedious task.

## 1.1 Aim and Objectives of the Research

The main aim of this thesis is to develop techniques based on enhancement and restoration for improving the interpretability or perception of quality in the foggy and hazy image/video. Many algorithms have been presented for improving the contrast of the foggy and hazy images. Even though these algorithms are increasing the contrast of weather degraded images, they fail to maintain the color fidelity. These methods take a huge amount of data manipulation which expand the computational complexity. Due to expansion of processing time, these algorithms are not acceptable for real-time deweathering. To address these issues, it is highly desirable to develop the techniques which will work for real-time processing and also maintain the color fidelity. Such techniques have been presented and experimentally verified in this thesis.

The objectives of this thesis are as follows:

1. To review the state-of-the art techniques for real-time dehazing and defogging of the images and videos.

2. To develop image enhancement based technique which creates a balance between high levels of visual quality and low computational cost. The developed method will be compared with respect to the state-of-the art techniques.

3. To develop image restoration techniques for weather degraded image/video which has good perceptual quality while preserving color contrast and also suitable for real time application. The developed method will be compared with respect to the state-of-the art techniques.

4. To implement the developed restoration technique using field programmable gate arrays (FPGA) and the performance will be tested.

## 1.2 Organization of the Thesis

The present research work is presented in six chapters. In addition to the current chapter, there are five other chapters that cover mathematical and theoretical analysis of current work. These chapters are as follows:

Chapter 1: The aims and objectives of the proposed research have been set in this chapter that will be covered in this thesis. Finally the organization adopted in the thesis have been highlighted.

Chapter 2: In this chapter, a survey of the literature on real time deweathering of image/video is done in detail. The literature study starts with details of atmospheric scattering mechanism and optical model. Later, deweathering algorithms have been discussed in detail that are more

ubiquitous for current thesis. Various real-time image and video deweathering algorithms along with experimental results are discussed. Based on the literature survey, the chapter concludes highlighting the research gaps that are being taken forward in the successive chapters.

Chapter 3: This chapter explains a fast and efficient technique for deweathering of image and video. In this chapter a detailed discussion of our proposed work on real-time approach for enhancing the contrast of the weather degraded images and videos are presented that is followed by comparison and experimental results.

Chapter 4: In this chapter, physical characteristics of removing haze and fog from an image and video are discussed. The description of physical characteristics starts with details of the atmospheric dichromatic model followed by contrast restoration for foggy and hazy image and video. In this chapter a detailed explanation of the proposed method for restoring the visibility of foggy and hazy images and videos are given. Then, detailed discussion of the experimental results are discussed. The details of the experimental work evaluate the different proposed approaches for real-time deweathering of the images and videos.

Chapter 5: In this chapter, we have presented our method for estimation of transmission map. A proper depth map is essential for restoring the visibility of foggy and hazy images. To meet the requirement of real time applications, a 9-stage pipeline hardware accelerator has been implemented with field programmable gate arrays (FPGA). For layout optimization UMC 65-nm technology is used.

Chapter 6: Finally, this chapter summarizes the specific contributions of the current study and conclusions gained from this research. Further, future scope and directions for research in this area has also been presented.

# Chapter 2

# Literature Review

This chapter reviews the state of the art of haze and fog removal from images and videos which are relevant to this work. The content of this chapter is focused on real time deweathering of the images and videos that have been extensively researched and developed over the past few years. All algorithms are analyzed in terms of their image quality enhancement and processing time based on extensive simulation results.

## 2.1 Introduction

Generally, bad weather conditions always affect the visibility of images. Under bad weather conditions, the contrast and color of the images are drastically degraded. To improve the contrast of weather degraded images generally used image processing methods are histogram equalization, unsharp masking and contrast stretching. But, the effects of weather cannot be completely removed by these techniques. In other words, it is simply not possible to expect consistent success without studying and modeling of the atmospheric conditions. So for deweathering of

images it is essential to consider both of these methods (enhancement and physical methods) which can significantly remove the weather effects from the images.

Imaging in poor weather is often severely degraded by scattering due to suspended particles in the atmosphere such as haze and fog [1, 10, 11]. Based on the type of the visual effects, bad weather conditions are broadly classified into two categories: steady and dynamic. In steady bad weather, constituent droplets are very small (1-10 $\mu$m) steadily float in the air. Fog, mist, and haze are examples of steady weather. The intensity produced at a pixel is due to the aggregate effect of the large numbers of the droplets within the pixel's solid angle. In dynamic bad weather, constituent droplets are 1000 times larger (0.1-10 mm) than those of the steady weather. Rain and snow represent dynamic weather conditions. As the image quality degradation dependents on size of suspended particle, the image restoration methods and algorithms also differ for steady weather condition and dynamic weather condition.

The literature review in this chapter is organized into seven parts including introduction. In the second part of this chapter, the scattering mechanism, which degrades the image/video is discussed. Based on the scattering mechanism, the optical model which acts as the basis of the development of image restoration algorithms is discussed in the third part. The fourth part covers the existing deweathering algorithms for image and video. The fifth part of the literature review discusses the various existing methods for real time processing of weather degraded image and video. In sixth part, the best approaches with respect to real-time application are extensively simulated and then compared based on simulation results. Finally the concluding remarks are given in the seventh part.

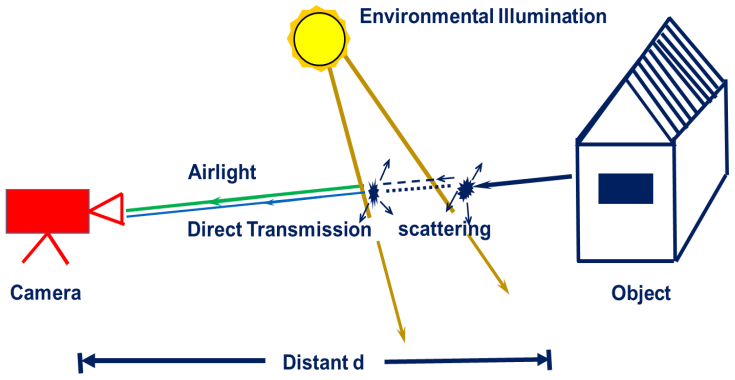


FIGURE 2.1: The pictorial description of the optical model

## 2.2 Atmospheric scattering mechanisms

Atmospheric scattering is the cause of image degradation in bad weather condition. It is the redirection of electromagnetic energy by particles suspended in the atmosphere or by large molecules of atmospheric gases. Poor weather caused by atmospheric particles, such as fog, haze, etc., may significantly reduce the visibility and distort the colors of the scene. In general, the exact nature of scattering is highly complex and depends on the types, orientation, size and distributions of particles constituting the media, as well as wavelengths, polarization states, and directions of the incident light. In this section we summarize two models of atmospheric scattering i.e. attenuation and airlight, followed by the discussion on wavelength dependency of scattering [10].

### 2.2.1 Attenuation and Airlight

The pictorial description of the optical model describing image capturing in the presence of atmospheric particles is shown in Fig. 2.1. Here, the reflected light beam coming straight from an object point to the camera is called direct transmission (or direct light). The reflected light

beam coming from an object point, gets attenuated due to scattering by atmospheric particles. The attenuation model describes the way light gets attenuated as it traverses from an object point to the camera. This phenomenon is termed as attenuation, which reduces contrast in the scene. As shown in Fig. 2.1, small amount of Light coming from the environmental illumination is scattered by the atmospheric particles, and coming toward camera. This leads to the change in color of the object. This phenomenon is termed as airlight. The image taken with the camera depends both on attenuation and airlight. The environmental illumination can have several light sources, including, direct sunlight and light reflected from the ground, etc. In steady bad weather conditions, attenuation is represented as:

$$I_{att}(x, y) = I_o(x, y)e^{-\beta d(x,y)} \tag{2.1}$$

where, $I_{att}(x, y)$ is the attenuated image intensity at pixel $(x, y)$ in presence of fog. $I_o(x, y)$ is the image intensity in absence of fog. $\beta$ is the scattering coefficient and $d$ is the distance of the object from the viewer or camera. Airlight is represented as:

$$A(x, y) = I_\infty(1 - e^{-\beta d(x,y)}) \tag{2.2}$$

where, $I_\infty$ is the global atmospheric constant.

### 2.2.2 Wavelength Dependence of Scattering

Due to the atmospheric particle, different wavelengths of light are scattered differently. The blueness of the sky and the bluish haze of distant mountains are examples of the wavelength selective behavior of atmospheric scattering [12, 13]. Over the visible spectrum, Rayleighs law of atmospheric scattering provides the relationship between the scattering coefficient $\beta$ and the

wavelength $\lambda$ as [14]:

$$\beta(\lambda) \propto \frac{1}{\lambda^{\alpha}} \tag{2.3}$$

where, $\alpha$ is a constant varies between 0 to 4 depending on the exact particle size distribution in the atmosphere. For fog, $\alpha \approx 0$; all wavelengths are scattered equally and we see grayish (or white) fog. A wide gamut of atmospheric conditions arises from aerosols whose particle sizes range between minute air molecules ($10^{-4}\mu m$) and large fog droplets ($1 - 10\mu m$) [11].

## 2.3 Optical Model

The optical model usually used in dealing with bad weather, particularly in computer vision, is described as:

$$I(x,y) = \underbrace{I_o(x,y)e^{-\beta d(x,y)}}_{\textbf{Attenuation}} + \underbrace{I_{\infty}(1 - e^{-\beta d(x,y)})}_{\textbf{Airlight}} \tag{2.4}$$

The first term is the direct attenuation, and the second term is the airlight. Equation (2.4) is in principle based on the Lambert-Beer law for transparent objects, which states that light travels through a material will be absorbed or attenuated exponentially [1]. When the atmosphere is homogenous, the transmission of the reflected light, which is determined by the distance between the object point and the camera is called as transmission map and can be expressed as:

$$T(x,y) = e^{-\beta d(x,y)} \tag{2.5}$$

Hence, an optical model equation can be described as:

$$I(x,y) = I_o(x,y)T(x,y) + I_{\infty}(1 - T(x,y)) \tag{2.6}$$

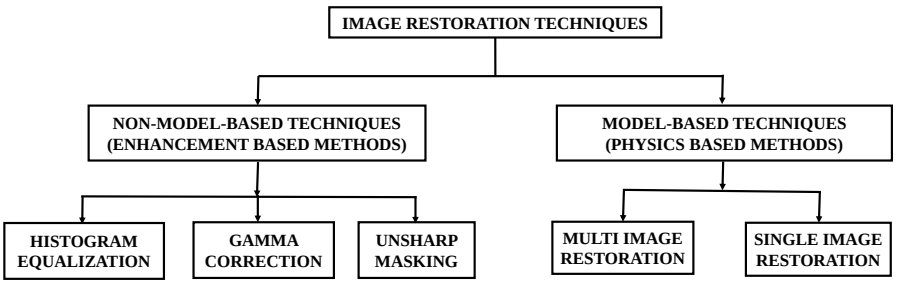


FIGURE 2.2: Image restoration classification techniques

## 2.4 Deweathering Algorithms

Deweathering algorithms can be broadly classified into two categories based on the approach they use to restore the image. Fig. 2.2 shows the classification of image restoration techniques. One is based on image enhancement technique, without considering the cause of degradation. This uses only image processing algorithms. The other set of algorithm considers the physical phenomenon of cause of image degradation due to bad weather. This uses the optical model which is discussed in the previous section to predict the pattern of image degradation and restore image. In this section all important deweathering algorithms belonging to both non-model based and model based techniques are analysed. These two techniques are discussed in this section for better understanding of real time processing which is the combination of both techniques.

### 2.4.1 Non-Model-Based Techniques

The most commonly used non-model-based techniques are histogram equalization, gamma correction and unsharp masking methods. Histogram equalization is an image enhancement process that attempts to spread out the most frequent intensity in an image. This is one of the most commonly used non-model-based technique which is applied directly on the weather degraded images to enhance the image quality by equally distributed pixel values [8, 15–17]. The


FIGURE 2.3: 'ny12', 'ny17', 'y01', 'Stadium', 'Mountain', 'Road', From left to right (a) Original image (b) Histogram Equalization (c) Gamma Correction (d) Unsharp Masking method.

histogram equalization of color images is performed separately for Red, Green and Blue (RGB) color channel. But this leads to undesirable change in hue. So, first convert the image to the Hue, Saturation and Intensity (HSI) because hue represents most dominant color as perceived by an observer. Then apply histogram equalization to the intensity component only [18]. This is one of the method for improving the contrast of the weather degraded images. Other method is Gamma Correction (GC) method. Most imaging system produces output intensity which is proportional to input intensity. Sometimes, this output and input relation are subjected to a nonlinear transfer function. GC is a process of compensating the nonlinearity in order to achieve correct reproduction of relative luminance [15]. These two methods are used for enhancement of the contrast. But, if we want to improve the enhancement of the contrast and sharpness of an image, we need a method for sharpness enhancement. The method used for this called unsharp masking. Some researchers had noticed that when a proportional amount of edge information is superimposed on the original image, the resulting contrast could be increased [19]. The essence of the procedure is to extract edges and then properly adjust its magnitude before addition to the original image. The unsharp masking procedure can be described by,

$$v(x, y) = u(x, y) + \delta z(x, y) \tag{2.7}$$

where, $v(x, y)$ is the enhanced pixel value, $u(x, y)$ is the input image pixel, $\delta$ is the enhancement gain factor, $z(x, y)$ is the edge pixel magnitude. Other non-model-based methods are retinex theory [20–23] and wavelet-based methods [24, 25]. These two methods are also image enhancement methods. But, we are not discussing in detail as the processing time taken by them are more.

The effect of three important deweathering algorithms are experimented on six standard images and shown in Fig. 2.3. The original image is given in Fig. 2.3 (a). The resulting images are given in Fig. 2.3 (b), Fig. 2.3 (c) and Fig. 2.3 (d) respectively. It can be seen that the restored

image by using histogram equalization improves the picture quality. However, this method does not fully maintain color fidelity. Next, the image is enhanced using gamma correction method giving better results. But this method is highly dependent upon the adjustment factor. Finally, unsharp masking is used for image enhancement. The edges are more clear by using this method, but the colors look over-saturated. Generally, all non-model-based methods have a problem with maintaining color fidelity. Also, Halo artifacts cannot be removed using these methods. This can only be eliminated with model based techniques.

### 2.4.2 Model-Based Techniques

Model-based techniques use physical models for image restoration. This model based technique can be categorized as multi image restoration and single image restoration based on number of images required to enhance the image as shown in Fig 2.2. The details of these two techniques are discussed in the following subsection.

### 2.4.3 Multiple image restoration

The basic idea of this approach is to exploit the differences of two or more images of the same scene that have different properties of the participating medium. Narasimhan et al. [1, 10, 11] proposed a method which requires multiple images of the same scene taken under different weather conditions.

In another multiple image technique based on polarization is proposed by Schechner et al. [26] use two input images taken with two differently polarized filters, one after another, to produce a deweathering image. This technique makes use of the fact that the airlight is at least partially polarized, whereas the direct transmission of the object is unpolarized. The main idea

of this approach is to exploit two or more images of the same scene that have different degrees of polarization (DOP), which are obtained by rotating a polarizing filter attached to the camera.

Multi image deweathering methods in general give qualitatively great results. But this tends to be unsuitable for real-time image deweathering as it processes two images taken under different weather conditions. So, development of an effective method for restoring the scene contrast from a single image is essential.

### 2.4.4 Single image restoration

In the past few years, many algorithms have been proposed for the removal of fog, mist and haze which use a single image. These algorithms estimate the depth information using an assumption or prior knowledge. This prior knowledge can be estimated automatically or given by the user. Here we will discuss three important algorithms which are basically dealing with single image restoration techniques.

Robby T. Tan has proposed an automated method that only requires a single input image [27]. His proposed method is based on the optical model:

$$I(x,y) = I_o(x,y)T(x,y) + I_\infty(1 - T(x,y)) \tag{2.8}$$

Based on this model, Tan focuses on enhancing image visibility. For a patch with uniform transmission $T$, the visibility (sum of gradient) of the input image is reduced by the haze, since $T < 1$ :

$$\sum_{(x,y)} \| \bigtriangledown I_o(x,y)\| = T \sum_{(x,y)} \| \bigtriangledown I_o(x,y)\| < \sum_{(x,y)} \| \bigtriangledown I_o(x,y)\| \tag{2.9}$$

Tan has developed a cost function in the framework of Markov random fields (MRF), which can be efficiently optimized by graph-cuts techniques. This algorithm is applicable for both

color and gray images. However, it does not recover the scenes original color. This method is not easily applicable for real-time applications. The computational time for a typical $600 \times 400$ images is approximately five to seven minutes (applying graph-cuts with multiple labels) [27].

Fattal [28] decomposed the scene radiance of an image into the albedo and the shading, and then estimated the scene radiance based on Independent Component Analysis (ICA). The method considered that the shading and object depth are locally uncorrelated. ICA is used to estimate transmission, and then inferred the color of the whole image by MRF. This approach is physics-based and can produce a natural haze-free image together with a good depth map. But, this approach is based on statistically independent assumption on a local patch. So, it requires the independent components varying significantly. Image restoration is based on the color information. So this method cannot be applied to the gray image. Hence fails when there is dense fog, as dense fog is often colorless.

He et al. [29, 30] have proposed a simple but effective dark channel prior method to remove haze from a single input image. The dark channel prior method is a kind of statistics of the haze-free outdoor images. It is based on the key observation that, most local patches in haze-free outdoor images contain some pixels which have very low intensities in at least one color channel. The dark channel prior gives a reliable assumption which provides us additional information to enable us to estimate the airlight $A$ and transmission $t(x)$. It is defined as follows:

$$I^{dark}(x,y) = \min_{c\varepsilon\{r,g,b\}} ( \min_{(x,y)\varepsilon\Omega} (I^c(\Omega))) \tag{2.10}$$

where, $I^c$ is a color channel of $I$, $c\varepsilon\{r,g,b\}$ is color channel index and $\Omega$ is a local patch in image. He et al. show that the transmission map can be estimated by:

$$\tilde{T}(x,y) = 1 - w \min_{c\varepsilon\{r,g,b\}} ( \min_{(x,y)\varepsilon\Omega} \frac{I^c(\Omega)}{I^c_\infty}) \tag{2.11}$$

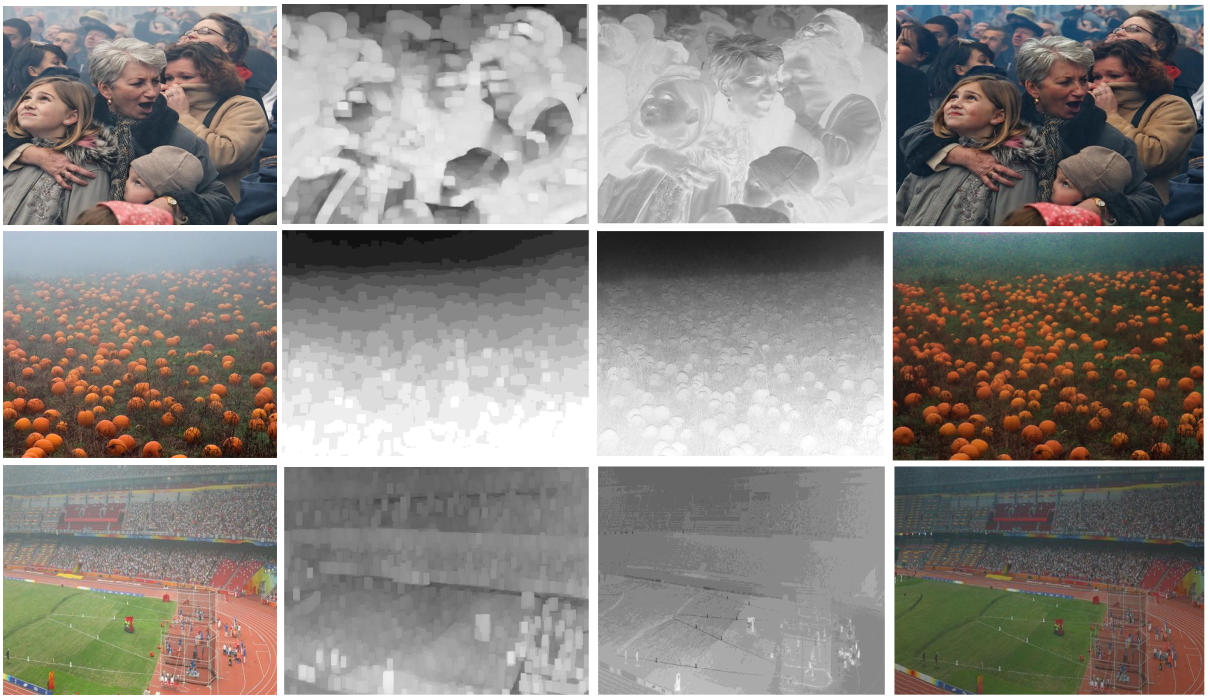


FIGURE 2.4: 'People', 'Pumpkin', 'Stadium', From left to right (a) Input haze image (b) Coarse Transmission map (c) Refined transmission map using soft matting (d) Recovered image

where, $w$ is a weighting factor and its value is application based. The parameter $w$ ($0 < w < 1$) is used to prevent removing the haze thoroughly, it is set to be 0.95. The transmission obtained by equation (2.11) is only a coarse transmission. The recovered image using the coarse transmission contains halo artifacts. Therefore, the transmission map needs to be refined. Transmission map refinement is done by using soft matting. Then finally recover the scene radiance. Results obtained by He et al. using the dark channel prior method for various outdoor haze images demonstrate the power of this method. Fig. 2.4 shows the results of image recovery using He et al. method which shows the effectiveness of the algorithm. Fig. 2.4 (a) shows an input hazy image; Fig. 2.4 (b) shows the coarse transmission map without soft matting; Fig. 2.4 (c) shows the refined transmission map with soft matting; and Fig. 2.4 (d) shows the recovered dehazy images. In the Fig. 2.4 (b), it is clearly visible halo artifacts are present.

Therefore, the transmission map needs to be refined. The refined transmission map tends to eliminate the halo artifacts using the soft matting method. But processing time is high due

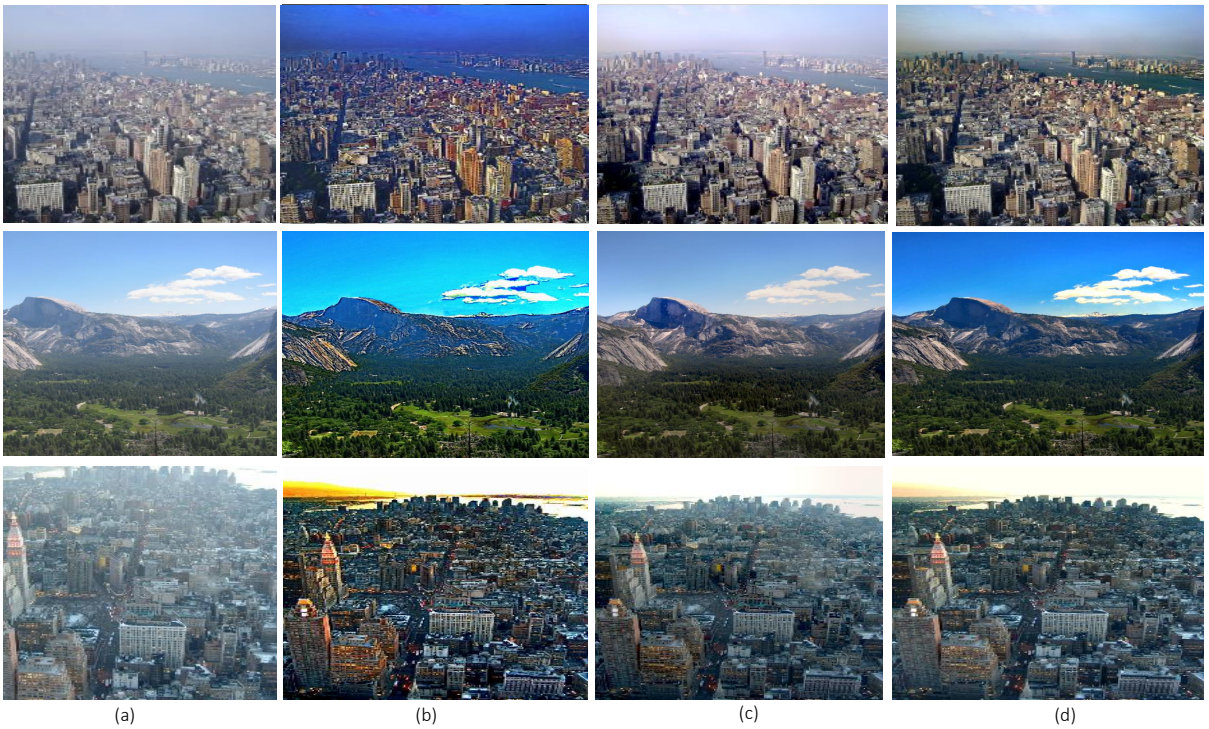


FIGURE 2.5: 'ny17', 'y01', 'ny12', From left to right (a) Input haze image (b) Tan algorithm [27], (c) Fattal algorithm [28], (d) He et al. algorithm [29, 30].

to the soft matting. This algorithm may be invalid if dense fog is present in the images.

These three algorithms are physically valid and are able to improve the visibility in the presence of poor weather conditions. Fig. 2.5 shows dehazed images by Tan [27], Fattal [28] and He et al. [29, 30]. But disadvantages of these algorithms are that, the processing speed is too slow. So, these three methods cannot be suitable for real time processing.

## 2.5 Real-time Image and Video Deweathering Algorithms

Recently few methods have been reported which are applicable for real-time processing of the weather degraded images and videos. This section aims to study different existing methods for real time processing of weather degraded images/videos and recovered scene contrast for period, from 2008 to till date. Verification for real-time deweathering was not reported in earlier work during the above mentioned period.

In 2008, Jisha John and M.Wilscy [31] present a novel method to enhance video sequences degraded by fog. In his work, background and foreground pixels are processed separately by a wavelet fusion method which reduces the computation time. The enhancement method is applied to the background as well as the foreground image separately and then combined to get the resultant video sequence. The experimental results provide better visibility and color fidelity. But the real time video deweathering of this method is not tested and verified.

Tarel and Hautiere [32] proposed an algorithm based on median filter. The algorithm is controlled only by a few parameters such as atmospheric veil inference, image restoration and smoothing and tone mapping. Tarel et al. solved the visibility restoration problem by maximizing the contrast of the resulting images, assuming that the depth map must be smooth except along the edges. Here the following optimization problem with constraint $0 \leq A(x,y) \leq W(x,y)$ was formalized

$$argmax_A \int_{(x,y)} A(x,y) - \Lambda\eta(\| \bigtriangledown A(x,y)\|)^2 \tag{2.12}$$

where, $A(x,y)$ is atmospheric veil and $W(x,y) = min(I(x,y))$ defined as the image of the minimal component of $I(x,y)$ for each pixel. $W$ is the image of the whiteness within the observed image $I(x,y)$. Parameter $\Lambda$ controls the smoothness of the solution and $\eta$ is an increasing concave function. The above formalized optimization is computationally extensive, so this optimization problem is resolved by the linear operation given as:

$$A(x,y) = max(min(p\ C(x,y), W(x,y)), 0) \tag{2.13}$$

$$C(x,y) = B(x,y) - median_{h\times h}(|(W-B)|)(x,y) \tag{2.14}$$

$$B(x,y) = median_{h\times h}(W)(x,y) \tag{2.15}$$

where, factor $p(0 < p < 4)$ control the strength of the visibility restoration and $h \times h$ is the spatial window size. Finally, restored image is obtained as :

$$I_o(x,y) = \frac{I(x,y) - A(x,y)}{1 - \frac{A(x,y)}{I_\infty}} \tag{2.16}$$

The main advantage of this algorithm compared with others is its speed. This fast algorithm allows visibility restoration to be applied for the first time within real-time processing applications such as sign, lane-marking and obstacle detection from an in-vehicle camera. Another advantage is the possibility to handle both color images and gray level images. But the restored image quality is not so good when there are discontinuities in the scene depth.

Zhiyuan Xu, Xiaoming Liu and Xiaonan Chen [16, 33] present a Contrast Limited Adaptive Histogram Equalization (CLAHE) based method to remove fog from video sequences. The CLAHE method applies histogram equalization to a contextual region. This method consists of three steps. In the first step, the background image is extracted from a video sequence degraded by fog and the motion objects are detected in each frame. Then apply some rectangular regions which can just cover the moving objects are selected as the foreground images. In second step is the background and foreground images in each frame are defogged by CLAHE method. The background and foreground images processed in each frame are fused to a new frame. Finally, the new frames are combined together in-order to get the video which has better visibility. This method is applicable for real time application, but it depends upon the maximum value to clipping the histogram level. Foreground extraction is described as:

$$Z_i(x,y) = 1, \|F_i(x,y) - N_{Bi}(x,y)\| > \alpha \tag{2.17}$$

$$0, \|F_i(x,y) - N_{Bi}(x,y)\| \leq \alpha \tag{2.18}$$

Where, $F_i(x, y)$ is the current frame, $N_{Bi}(x, y)$ is the background frame and $\alpha$ is a user set threshold. The CLAHE method is then applied to the background and foreground separately by calculating local histograms. This method is applicable for real time application, but it depends upon the maximum value to clipping the histogram level.

In 2010, Lv et al. [34] and He et al. [35] presented a deweathering algorithms which are based on filtering method. The most effective filtering methods are bilateral filter, cross-bilateral filter and guided filter methods. The bilateral filter [36, 37] is a commonly used filter. When the bilateral filter uses a second image as guidance, it is called joint-bilateral or cross-bilateral filter [34, 38]. The bilateral filter is easy to implement but computational complexity is more as compared to guided image filter. Guided image filter is closely related to laplacian matting and bilateral filtering. Guided image filter [35] is a type of edge-preserving smoothing operator, it generates the filtering output by considering the content of a guiding image, which can be the input image itself or another different image. It is defined as follows:

$$q_i = a_k I_i + b_k, \forall_i \epsilon w_k \tag{2.19}$$

where, $I$ is a guidance image, linear coefficients $a_k$ and $b_k$ are constants in a window $w_k$ centered at pixel k and $q$ is filtering output. The main advantage of this method is its low computational cost. This method does not work when the depth change at the object edge is too abrupt.

From 2010 onwards many researchers came up with different ideas and methods [39–42] for real time processing based deweathering. In these papers, the mainly used method is the guided filter method. This is one of the fastest edge-preserving filter methods to remove haze, fog, rain and snow from images. Fig. 2.6 shows the generalized flowchart of real time processing of image deweathering by using the guided filter method. We obtained weather degraded image/video. Then, estimated the airlight and transmission map using the dark channel prior method. In

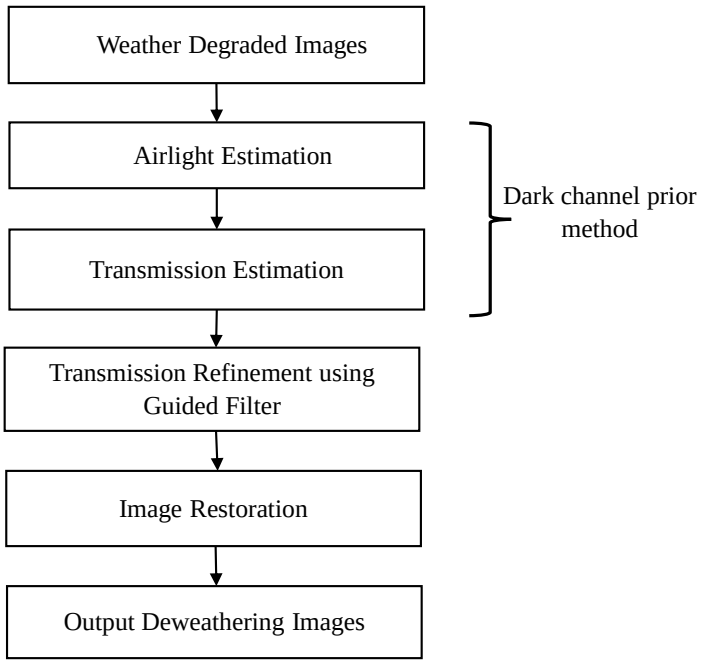


FIGURE 2.6: Flowchart of real time processing of images and videos deweathering

order to further refine the transmission map guided filter is used. Finally, restore the output deweathering image/video.

Kim et al. presented a dehazing algorithm based on the optimized contrast enhancement and extended this algorithm to the real-time video dehazing algorithm, by employing the temporal coherent cost [43]. Kim et al. algorithm first selects the atmospheric light in a hazy image using the quad-tree based subdivision. Then, since a hazy image has low contrast, the proposed algorithm determines transmission values. These values are adaptive to scene depths which increase the contrast of the restored image. Kim et al. solved this low contrast problem by Mean squared error (MSE) contrast method. Mean contrast is expressed as :

$$C_{MSE} = \sum_{(x,y=1)}^{N} \left( \frac{(Ioc(x,y) - \overline{I}_{oc}(x,y))^2}{N} \right) \tag{2.20}$$

where, $c\epsilon(r, g, b)$ is the color channel index, $\overline{I}_{oc}(x, y)$ is the average of $Ioc(x, y)$, and N is the number of pixels in a block. $C_{MSE}$ of the restore block can be rewritten as:

$$C_{MSE} = \sum_{(x,y=1)}^{N} \left( \frac{(Ic(x,y) - \overline{Ic}(x,y))^2}{t^2 N} \right) \tag{2.21}$$

For reducing the information loss, Kim et al. designed the two cost functions. One is contrast cost and second is information loss cost. The contrast cost $I_{contrast}$ is

$$I_{contrast} = - \sum_{c\epsilon(r,g,b)} \sum_{(x,y)\epsilon B} \left( \frac{(Ioc(x,y) - \overline{I}_{oc}(x,y))^2}{N_B} \right) \tag{2.22}$$

where, $N_B$ is the number of pixels in block $B$. Information loss cost $I_{loss}$ for block $B$ is represented as:

$$I_{loss} = \sum_{c\epsilon(r,g,b)} \sum_{(x,y)\epsilon B} \left( (min(0, Ioc(x, y))^2 + ((min(0, Ioc(x, y) - 255)^2 \right) \tag{2.23}$$

Overall cost function is defined as:

$$I = I_{contrast} + \lambda_L I_{loss} \tag{2.24}$$

$\lambda_L$ is a weighting parameter that controls the contrast cost and the information loss cost. Then calculate the transmission map. An edge preserving filter is used for transmission map refinement. So, guided filter is used for transmission map refinement of static image dehazing. Next, Kim et al. proposed an algorithm for real time video dehazing first converts a video sequence into the YUV color space. Where, Y component referred to the luminance of the color, and the U and V components determine the chromaticity. Then process only the luminance (Y) component, without modifying the chrominance (U,V) components, to reduce the computational complexity. For fast transmission refinement of the video sequence, only the luminance component is used to compute the pixel-based transmission values. At each pixel position, extract a temporal sequence

of pixel values through a video clip, then filter the sequence based on the human perception model.

Shiau et al. [44] presented a fast and efficient haze removal method. Many researcher assume airlight is known or picked the top 0.1% brightest pixel from the dark channel and selected a suitable value from these brightest pixels as the atmospheric light. This process takes a lot of time for sorting of the pixel. The execution time will increase with the size of an input image. For resolving this problem Shiau et al. propose an extremum approximation method to extract the atmospheric light. This method employs a 3 x 3 minimum filter to obtain the dark channel and finds the pixel with the maximum value in the dark channel. Thus for an image, dark channel image is defined as:

$$I^{dark'}(x,y) = \min(\min I^R(x,y), \min I^G(x,y), \min I^R(x,y)) \tag{2.25}$$

where min is the minimum operation to find the minimum value among $\min I^R$, $\min I^G$ and $\min I^B$ at (x, y) coordinate. Atmospheric light is determined as:

$$I_\infty^{dark} = \max_{(x,y)\epsilon I}(I^{dark'}(x,y)) \tag{2.26}$$

The refined atmospheric light is generalized by

$$I_\infty^c = \sigma \times (I^c(x,y)) \tag{2.27}$$

Then, the transmission map is estimated by using an edge detection method to find the contour of objects and apply edge-preserving filter and mean filter. Final scene radiance $I_o(x,y)$ is recovered by

$$I_o^c(x,y) = \frac{I^c(x,y) - I_\infty^c}{max(T(x,y), T_O')} + I_\infty^c \qquad \forall_c \epsilon (R,G,B) \tag{2.28}$$

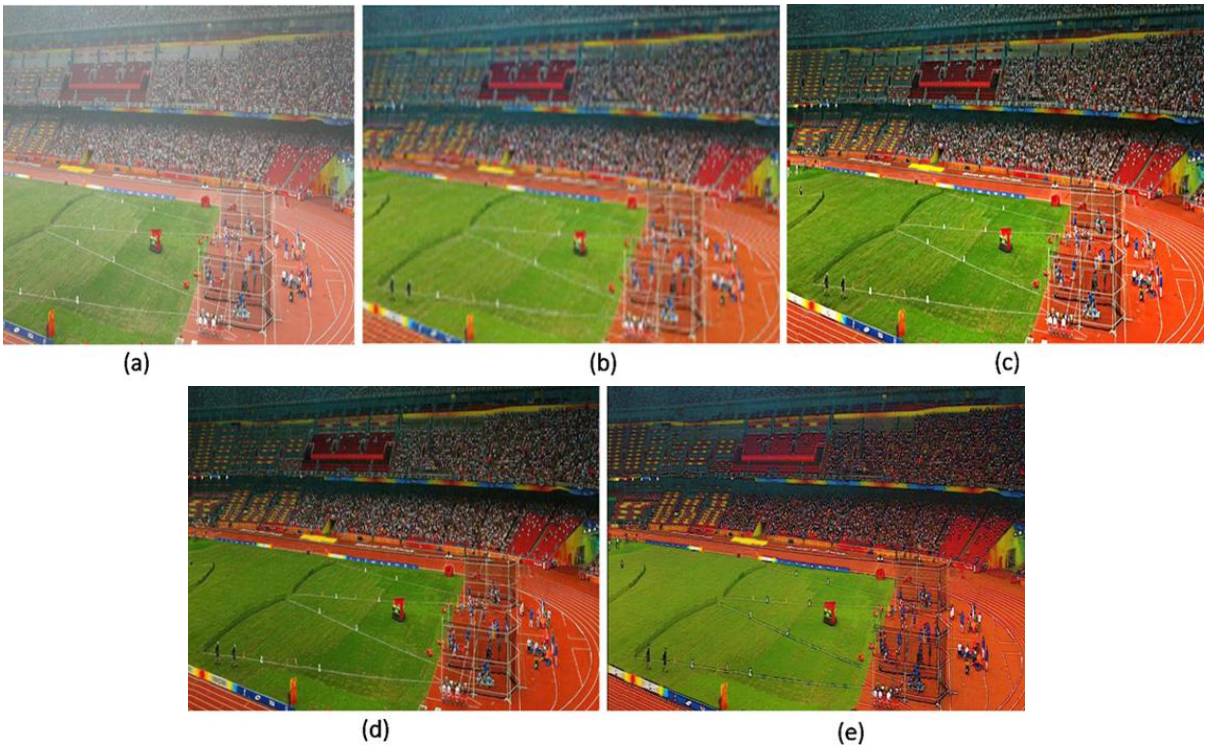


FIGURE 2.7: 'Stadium', From left to right (a) Input haze image. The dehazed images obtained by (b) Tarel et al. algorithm [32] (c) Bilateral filter method [34] (d) Guided filter method [41]and (e) Shiau et al. method [44].

where, $T'_O$ is a low bound of the transmission. Since the color of the recovered scene looks over-saturated. Shiau et al. present a saturation correction method to adjust the scene radiance. This method is also suitable for real-time applications as they designed a low-cost, high performance pipeline hardware architecture for haze removal.

We have discussed different deweathering algorithms using which the estimation of depth and enhancement of the contrast of the images with various assumptions along with advantages and disadvantages were taken into account. Fig. 2.7 shows the haze removal results. In the next section we will compare different algorithms and results in terms of contrast restoration and processing time.

## 2.6 Comparison and Experimental Results

In this section we have compared seven important different deweathering algorithms qualitatively as well as quantitatively in terms of blind contrast restoration assessment method and processing time clearly. The eight algorithms chosen are Tan algorithm [27], Fattal algorithm [28], He et al. algorithm [29], Tarel et al. algorithm [32], Bilateral filter method [34], Guided filter method [41] and Shiau et al. method [44] based on feasibility to real time approach and restoration quality. So, to demonstrate the effectiveness of these eight different algorithms, we collected 200 weather degraded image sets from different image search engine (google.com and flickr.com) and applied these algorithms on them. Two sets of typical images (y16 and Swan input) are selected as representatives of weather degraded images for restoration experiments.

### 2.6.1 Qualitative Results

Qualitative results of selected deweathering algorithms are shown in Figs. 2.8 and 2.9. Figs. 2.8 (a) and 2.9 (a) show the original foggy images. Figs. 2.8 (b) and Fig. 2.9 (b) show deweathering image by Tan [27] algorithm from which it can be seen that haze free images have higher contrast than input hazy images. This algorithm produces acceptable results, but restored images may contain halo artifacts and color distortion is more. Figs. 2.8 (c) and 2.9 (c) show deweathering image by Fattal [28] algorithm. This algorithm yields more natural results as compared to He et al. [29] algorithm. However, this algorithm may fail when dense haze is present. Moreover, this method requires enough color information, otherwise we cannot get a true transmission map. It can be observed from Fig. 2.9 (c). He et al. [29] algorithm gives good results and maintain the naturalness well (as shown in Fig. 2.8 (d)). This method uses a soft matting technique to refine the transmission map. It cannot effectively optimize the transmission near complex regions. Fig. 2.9 (d) shows the recovered image by the method of He et al., which contains halo

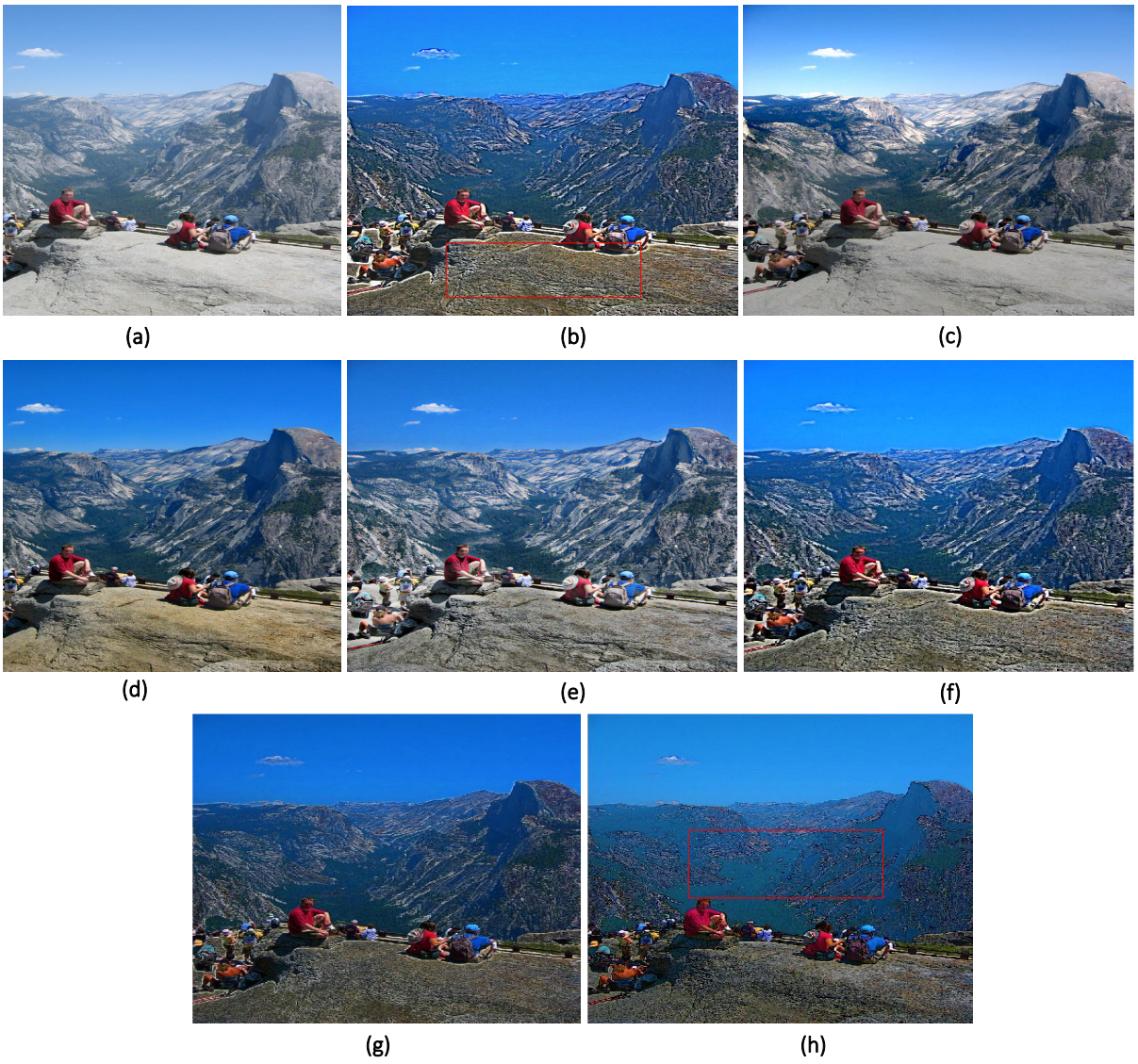


FIGURE 2.8: 'y16', From left to right (a) Input haze image. The dehazed images obtained by (b) Tan algorithm [27] (c) Fattal algorithm [28] (d) He et al. algorithm [29] (e) Tarel et al. algorithm [32] (f) Bilateral filter method [34] (g) Guided filter method [41] (h) Shiau et al. method [44].

artifacts. Figs. 2.8 (e) and 2.9 (e) show deweathering image by Tarel's [32] algorithm. By using this algorithm recovered colors look oversaturated and exhibits halo artifacts. The bilateral filter method suppresses the halo artifacts (as shown in Figs. 2.8 (f) and 2.9 (f)). This method needs to calculate a weighted average of neighboring pixels and is able to preserve the edges of processed images. It is not reliable for dense fog. Figs. 2.8 (g) and 2.9 (g) show deweathering image by guided filter method [41] which gives enhanced image quality. Sometimes this method fails to achieve an appropriate perceptual quality in the sky areas. Shiau et al. [44] method can

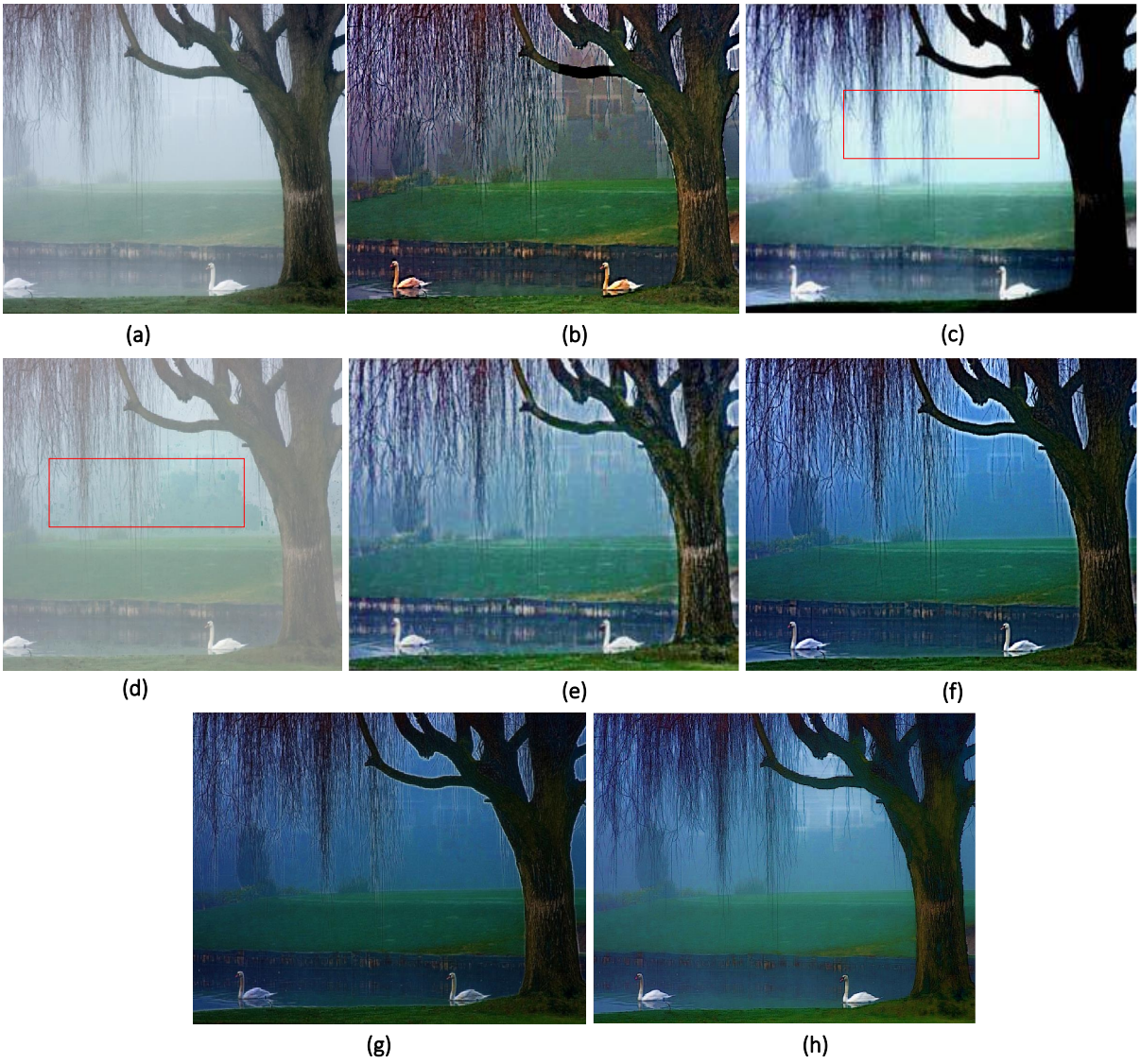


FIGURE 2.9: 'Swan input', From left to right (a) Input haze image. The dehazed images obtained by (b) Tan algorithm [27] (c) Fattal algorithm [28] (d) He et al. algorithm [29] (e) Tarel et al. algorithm [32] (f) Bilateral filter method [34] (g) Guided filter method [41] (h) Shiau et al. method [44].

efficiently avoid the halo artifact generated in the recovered image (as shown in Fig. 2.9 (h)). However, it is not preserving the edges of the image well. It can be observed from Fig. 2.8(h), wherein there is color distortion in the mountain area.

TABLE 2.1: **Quantitative and Processing Time Comparison**

| Indictor | Input | Method | e | r | Time /second |
|---|---|---|---|---|---|
| **Figure 2.3** | ny12, ny17, y01, Stadium, Mountain, Road | Histogram Equalization (a) | -0.405, -0.370, -0.408, 0.415, 0.444, -0.441 | 0.9663, 1.1170, 1.1430, 2.1910, 1.4608, 1.4528 | 0.597, 0.658,0.548, 0.678, 0.587, 0.611 |
| | | Gamma Correction (b) | -0.351, -0.999, -0.998, 0.310, -0.998, -0.997 | 0.7220, 0.8203, 0.7886, 0.9031, 0.6837, 0.8068 | 0.460, 0.499, 0.477, 0.605, 0.522, 0.506 |
| | | Unsharp Masking method (c) | -0.288, -0.352, -0.306, 0.435, -0.998, -0.445 | 1.3610, 1.4887, 1.4915, 1.8354, 1.5828, 1.5199 | 0.470, 0.508, 0.473, 0.627, 0.593, 0.543 |
| **Figure 2.4** | People, Pumpkin, Stadium | He et al. algorithm | 0.487, 0.448, -0.046 | 1.2947, 1.3387, 0.5515 | 65.499, 51.242, 70.366 |
| **Figure 2.5** | ny17, y01, ny12 | Tan algorithm (b) | 0.035, 0.019, -0.047 | 2.0234, 2.2723, 2.1968 | 190.987, 142.085, 140.098 |
| | | Fattal algorithm (c) | 0.012, 0.057, 0.053 | 1.1409, 1.1682, 1.2138 | 3.248, 2.921, 2.914 |
| | | He et al. algorithm (d) | 0.015, 0.014, 0.062 | 1.5448, 1.3740, 1.3659 | 664.427, 97.081, 98.016 |
| **Figure 2.7** | Stadium | Tarel et al. (b) | -0.016 | 1.9184 | 3.425 |
| | | Bilateral filter method (c) | 0.239 | 1.5051 | 17.032 |
| | | Guided filter method (d) | 0.256 | 1.1768 | 6.312 |
| | | Shiau et al. method (e) | -0.100 | 1.3052 | 6.117 |
| **Figure 2.8** | y16 | Tan algorithm (b) | 0.004 | 2.0460 | 140.651 |
| | | Fattal algorithm (c) | -0.062 | 1.1601 | 2.932 |
| | | He et al. algorithm (d) | 0.065 | 1.3338 | 98.116 |
| | | Tarel et al. algorithm (e) | -0.0137 | 1.7426 | 4.934 |
| | | Bilateral filter method (f) | -0.143 | 2.5303 | 25.406 |
| | | Guided filter method (g) | -0.250 | 1.6329 | 6.467 |
| | | Shiau et al. method (h) | -0.173 | 1.1391 | 7.228 |
| **Figure 2.9** | Swan input | Tan algorithm (b) | 0.3221 | 2.5294 | 180.567 |
| | | Fattal algorithm (c) | -0.246 | 1.0200 | 2.985 |
| | | He et al. algorithm (d) | -0.173 | 0.6284 | 106.064 |
| | | Tarel et al. algorithm (e) | -0.198 | 1.3870 | 4.817 |
| | | Bilateral filter method (f) | -0.068 | 2.3329 | 23.467 |
| | | Guided filter method (g) | -0.051 | 1.4645 | 7.993 |
| | | Shiau et al. method (h) | -0.225 | 1.1697 | 7.560 |

### 2.6.2 Quantitative Results

For the quantitative analysis, blind contrast restoration assessment is used. To the best of our knowledge, the widely used blind assessment method in the image dehazing field is the visible edge gradient method proposed by Hautiere et al. [45]. The method defines two parameters for quantitative analysis of the images which are $e$ and $r$. $e$ is the ratio of the number of sets of new

visible edges of the original image and the restored image. They are expressed as:

$$e = \frac{n_r - n_o}{n_o} \tag{2.29}$$

where, $n_r$ and $n_o$ are the numbers of visible edges in the original image and the restored image. The other parameter is the $r$, which is the average gradient ratio of the original image and the restored image

$$r = \frac{g_r}{g_o} \tag{2.30}$$

where, $g_r$ and $g_o$ are the average gradients of the original image and the restored image. For haze removal, greater the $e$ and $r$ , better the dehazing effect.

Table 2.1 demonstrates the quantitative measure of contrast and processing time comparison for the Figs. 2.3 to 2.9. Analyzing the results of Table 2.1, indicator $e$ shows that the eight methods which are depending on the processed image remove some of the visible edges. For the images 'ny12', 'ny17' and 'y01', Fattal algorithm [28], He et al. algorithm [29], are characterized by positive values of the indicator $e$. For the images 'People', and 'Pumpkin', He et al. algorithm [29] and for 'Stadium', Histogram equalization, Gamma correction, Unsharp masking method, Bilateral filter method [34] and Guided filter method [41] are characterized by positive values of the $e$. Next for two images 'y16' and 'Swan input', Tan algorithm [27] and He et al. algorithm [29] are characterized by positive values of the $e$. Bilateral filter method [39], Guided filter method [41] and Shiau et al. method [44] for images (y16 and Swan input) show the negative values of the $e$. Moreover, regarding indicator $r$, the techniques of Tan algorithm [27] and Bilateral filter method [34] increase too strongly the local contrast and as a result, these approaches have higher values of indicator $r$.

Another very important parameter is processing time. Processing time is the execution time taken by algorithms to remove fog, haze and rain from the image. This depends upon

the image input size. Lower processing time indicates faster algorithm. The processing time is a good indicator when we consider real-time fog and haze removal applications. The time complexity of Tan algorithm [27], Fattal algorithm [28], He et al. algorithm [29], Tarel et al. algorithm [32], Bilateral filter method [34], Guided filter method [41] and Shiau et al. method [44] are analyzed for the image size $M \times N$. The processing time for an $M \times N$ images are approximately five to seven minutes by using a Tan algorithm [27]. In the case of the Fattal algorithm [28], the airlight-albedo might differ between every pixel which increases the complexity of the problem. Therefore, it is difficult to find out the exact computation complexity. The approximate computational complexity of this method is O(MN) time. In the case of He et al. algorithm [29], the dark channel can be computed in O(MN) time, but the problem with this method is its soft matting method. It requires some extensive and complex computations, such as huge matrix multiplication/division, sort, exponent, and floating-point operation. The computation complexity of the Tarel et al. algorithm [32] is O(MN $Sv^2 lnSv$) for an image, in which $Sv$ is the template size of the median filter. Tarel et al. Algorithm [32] uses a fast implementation of median filter proposed by S. Perreault and P. Hebert [46]. Due to this reason, complexity is reduced to O(MN) time. This is a linear function of the number of input image pixels, whatever the value of $Sv$. So, this method is applicable for real time processing. However, it sometimes may be failed in processing tiny boundaries when discontinuities are present in the scene depth. In the case of edge preserving filtering method such as the bilateral filter and the guided filter. The guided filter is a superior. The computational complexity of bilateral filter is O($MN^2$). Guided filter method [41] comes with a computational complexity of O(MN), independent of filter radius. So, this property is quite important for real time single image deweathering. The computation complexity of the Shiau et al. method [44] is O(MN) time. This method needs some computations, such as matrix multiplication, addition and division.

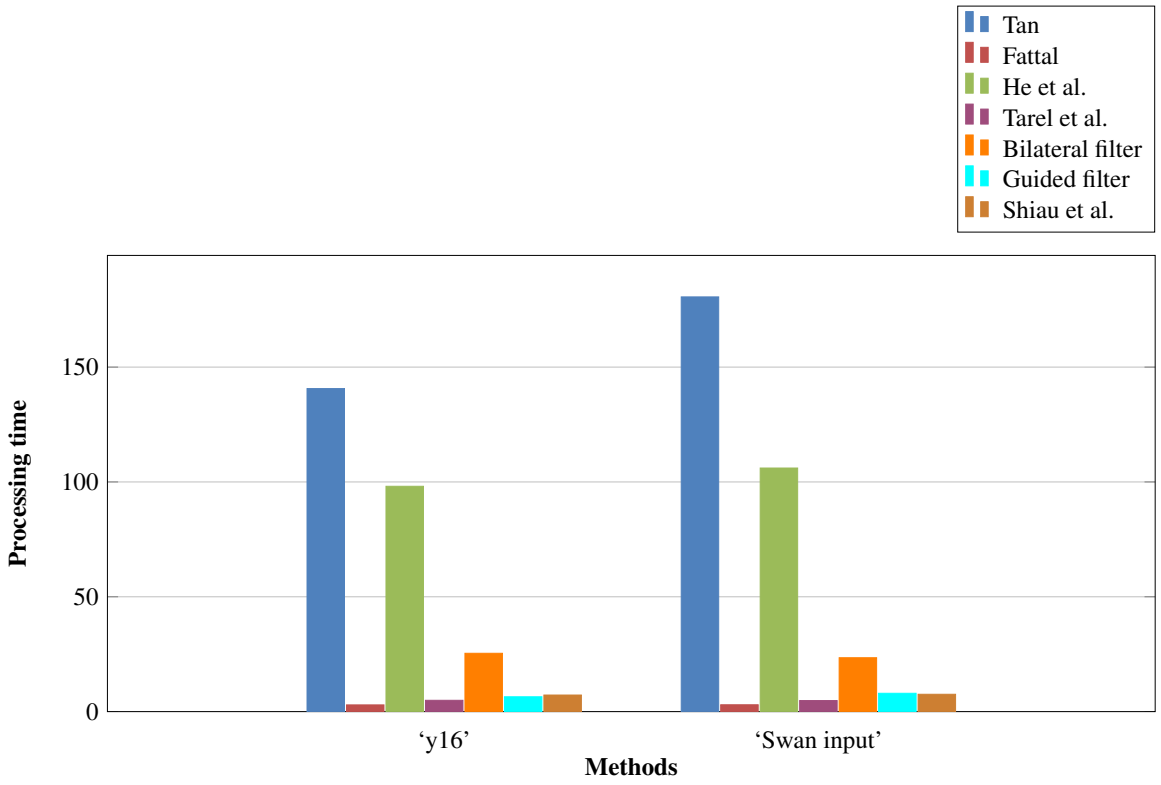


FIGURE 2.10: Processing time comparison chart of different methods for two selective images 'y16' and 'Swan input'

We compare the computational complexity for Tan algorithm [27], He et al. algorithm [29], Fattal algorithm [28], Tarel et al. algorithm [32] and Shiau et al. method [44] with the help of the comparison chart as shown in Fig. 2.10. Here, we have considered images 'y16' and 'Swan for the representation of above discussed methods. We observed that the time taken by Tan algorithm [27] and He et al. algorithm [29] are more. So, these methods are not suitable for real time deweathering of the images and videos. Fattal algorithm [28] takes less processing time, but cannot well handle heavy haze images. Tarel et al. algorithm [32] is computationally less complicated and less processing time as compared to [27] and [29], but it changes color tone and produce the halo effects around the boundary of the image. Bilateral filter method [34] improve the image quality and suppress the halo artifacts. This method is computationally more complicated. Guided filter method [41] and Shiau et al. method [44] reduce the computational complexity. However, these methods do not preserve the details of the images.

## 2.7 Research Gaps

Based on the above review, the following research gaps were identified. The research gaps that are addressed in the thesis are summarized as follows:

(i) The enhancement of bad weather conditions images and videos is a challenge due to the complexity in recovering the luminance and chrominance while maintaining the color fidelity. The existing methods available for enhancement of weather degraded images and videos do not fully maintain color fidelity.

(ii) Image restoration techniques in existing works are not suitable for real time and accurate measurement of unknown scene depth. Therefore, the restored images and videos of the existing techniques have unwanted artifacts.

(iii) For real time implementation the important factors to be considered are power consumption and processing time. The existing methods have not discussed these. Therefore, the suitability for real time implementation is not fully known.

With this study of the state-of-the-art, from the next chapter onwards, attempts to fill the above gaps have been made. Detailed analysis of different proposed approaches for image and video deweathering have been presented.

## 2.8 Conclusion

In this chapter, an extensive study of algorithms for real-time processing of weather degraded images under steady bad weather condition is carried out. Firstly, we have briefed the scattering mechanism, which degrades the image quality. Then we have discussed about deweathering algorithms which are based on non-model and model based techniques. Next, important existing

methods for real-time image and video deweathering are discussed in detail with their advantages and disadvantages. But, we observe certain disadvantages which motivated us to carry out our research in the direction of real-time dehazing and defogging of image and video.

Due to the availability of extremely high computational power at low cost, the real time deweathering of images can be feasible and useful for driving assistance, outdoor surveillance application and in many other applications. So, we propose the algorithms specifically capable of approaching real time requirements in the subsequent chapters.

# Chapter 3

# Contrast Enhancement of Weather Degraded Image and Video

The bad weather conditions including fog and haze make the acquired image contrast lower. This makes computer vision application fail to detect or recognize objects. In this chapter, a fast technique for efficient deweathering of image and video is presented. We proposed an approach of gamma correction using look-up-table method to obtain higher contrast images. The use of look-up-table (LUT) in these images makes our approach appreciably faster. Moreover, we extend the static image to real-time video deweathering. The main advantage of the proposed approach compared with others is its higher speed which allows the real-time video processing.

## 3.1 Introduction

Poor visibility in bad weather is a major problem for many applications such as intelligent vehicles, outdoor object recognition and remote sensing systems etc. The real time deweathering is very important for many such similar applications. Dehazing and defogging methods can be

divided into two categories: image restoration methods and image enhancement methods. The image restoration based algorithms can achieve better results, but these methods are usually complex. As a result, the algorithms will cost much more running time. In contrast with the image restoration based algorithm, the image processing based algorithms simply process the image and enhance the contrast. More importantly, the running time, cost much less than the image restoration based algorithms.

Restoring the weather degraded images requires the physical causes of image degradation and depth estimation for recovering the dehazing the images. Given the importance of restoration based dehazing algorithms, many studies on dehazing have been conducted. Here, we have explained five important restoration techniques [27, 28, 30, 32, 41] for deweathering. Tan [27] maximized the contrast of a hazy image, assuming that a haze-free image has a higher contrast ratio than the hazy image. Tan's algorithm, however, tends to overcompensate for the reduced contrast, yielding halo artifacts. The above conclusion can be observed from Fig. 3.1 (b), wherein there are halo artifacts present in the mountain. Fattal [28] exploits the fact that the transmission and scene albedo are locally uncorrelated to dehaze the image. This approach is physically sound and can produce impressive results. However, it is deeply based on the color and thus cannot deal with a gray level image. He et al. [30] proposed a novel algorithm based on Dark Channel Prior (DCP) which is physically valid and is able to handle distant objects in heavily hazy images. He found that some pixels have very low intensity in at least one color (RGB) channel. His method shows the best quality of result with haze among the image restoration methods (as shown in Fig. 3.1 (d)), where the soft matting algorithm to refine the transmission map was used. This matting algorithm requires numerous data to obtain the exact transmission at discontinuous edge of depth map. Therefore, it is difficult for real time processing. To overcome these problems, Tarel and Hautiere [32] proposed a novel algorithm based on median filter. The algorithm is controlled only by a few parameters such as atmospheric

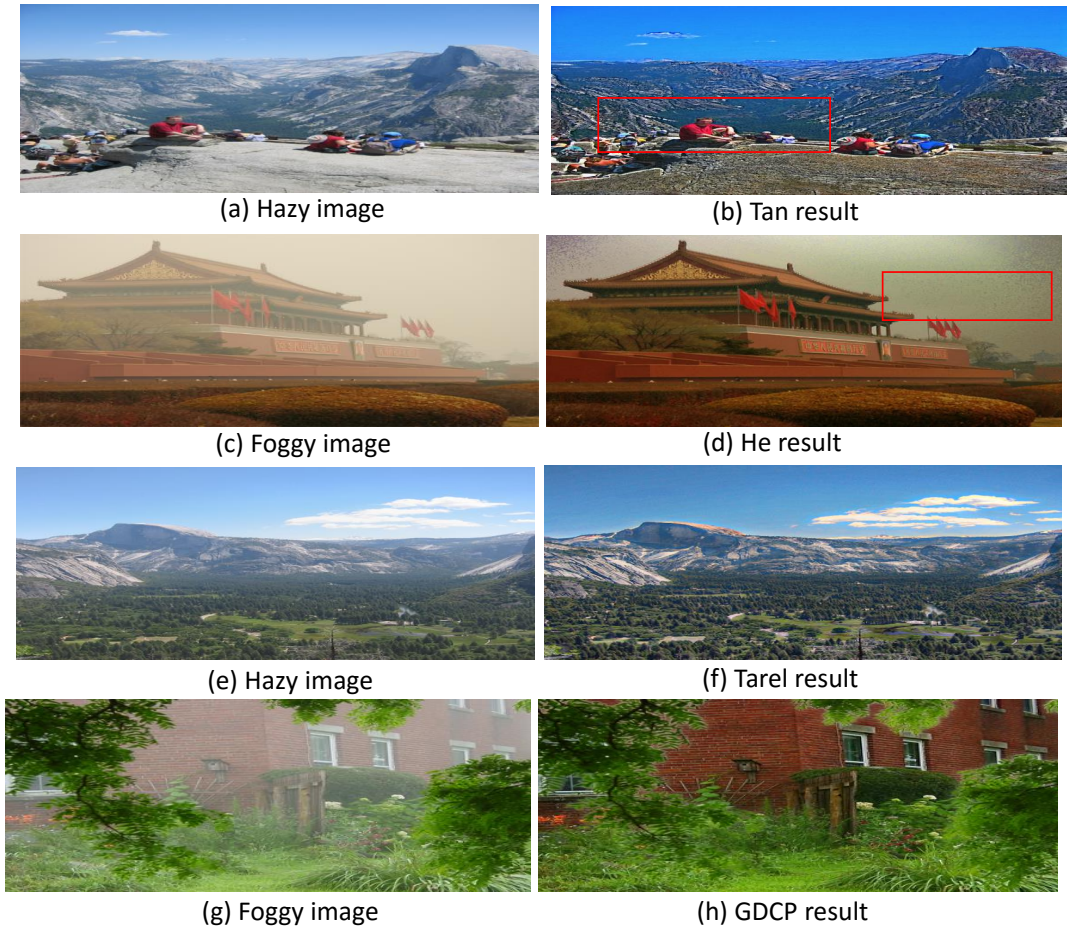


FIGURE 3.1: Limitation of current single image dehazing and defogging algorithms of Tan result, He result, Tarel result and GDCP result.

veil inference, image restoration, smoothing and tone mapping. This is based on the assumption that fog is white. Though Tarel's method is possible for real time processing, but the halos cannot be completely eliminated which can be observed from Fig. 3.1 (f). Recently, He et al. [41] proposed a guided filter, and found that the output of a guided filter could be approximate solution of the soft matting algorithm. This algorithm reduces the time complexity. However, this may lead to image blurring because the original foggy image was chosen as the reference image shown in Fig. 3.1 (h).

Enhancing images represent a fundamental task in many image processing and vision applications. Image enhancement methods tend to increase the dynamic range and contrast of images degraded by haze. This method does not need any scene depth information and avoid complicated atmospheric scattering model. In image processing area, the most commonly used

non-model-based methods are histogram equalization and its variations [8, 16–18]. Though histogram equalization method is simple and suitable for almost all types of images, but it fails to enhance the local features. Wadud et al. [47] has proposed dynamic histogram equalization (DHE) for used in the image contrast enhancement. However, even this method does not fully maintain color fidelity. There are other, non-model-based methods like unsharp masking [48], approaches based on the Retinex theory [20, 22, 49] and wavelet-based methods [24, 25]. Bin-Na Yu et al. [50] has proposed a modified structure of the Retinex algorithm for the image enhancement method. Generally, all non-model-based methods have a problem with maintaining color fidelity. They also distort clear images, which is one of the important limitation for fully automatic operation. Recently, Wang et al. [51] presents a new method for fast single haze image enhancement without using any extra information. This approach simultaneously dehazes image and enhances sharpness by means of individual treatment of the model component and the residual.

We find that although image restoration techniques give better image quality, image enhancement based techniques require much less processing time. There is a need for acceptable perceptual image qualify with less processing costs. Therefore, in this work, we propose the real time approach for enhancing the contrast of the weather degraded images. We will discuss the proposed approach which is based on the enhancement method. This approach removes the haze and fog by simply applying the gamma correction using look-up-table method.

The rest of this chapter is organized as follows: Section 3.2 presents our proposed method in detail for deweathering the images and videos. In section 3.3, the effectiveness of the proposed method is supported by comparing the experimental results obtained through use of our method to those obtained via existing methods. Finally, section 3.4 concludes this work.

## 3.2 Fast Single Image and Video Deweathering using Look-Up-Table Approach

To compensate for the limitations of above discuss methods, a technique must be developed which creates a balance between high levels of visual quality and low computational costs. We have proposed gamma correction using look-up-table based approach. In this section, we are discussing our approach for contrast enhancement of image as well as the same approach for video.

### 3.2.1 Image Dehazing and Defogging using Look-Up-Table Approach

We present, gamma correction using look-up-table method that improves the contrast of the images and reduce the time complexity. Using a look-up-table avoids needless repeated computations. The formula to create a LUT for an 8-bit image is described as:

$$LUT = max\ intensity \times \left( \frac{[0 : max\ intensity]}{max\ intensity} \right)^{\gamma} \tag{3.1}$$

Fig. 3.2 shows the flowchart of the proposed method for real time deweathering of the images. In this approach the weather degraded image is filtered using median filter. This filter is capable of reducing noise and preserving the edges of the input image. The window size of the median filter is used as $3 \times 3$ to have reduced processing time. Edges are scaled by the constant gain factor of value 0.5. For various values of $\gamma$ different levels of enhancements can be obtained. Design procedure for the real time deweathering of the images are carried out as below:

1. Take the hazy and foggy image.

2. Filter the weather degraded image.

3. Extract edges from the difference between the input image and filtered image.

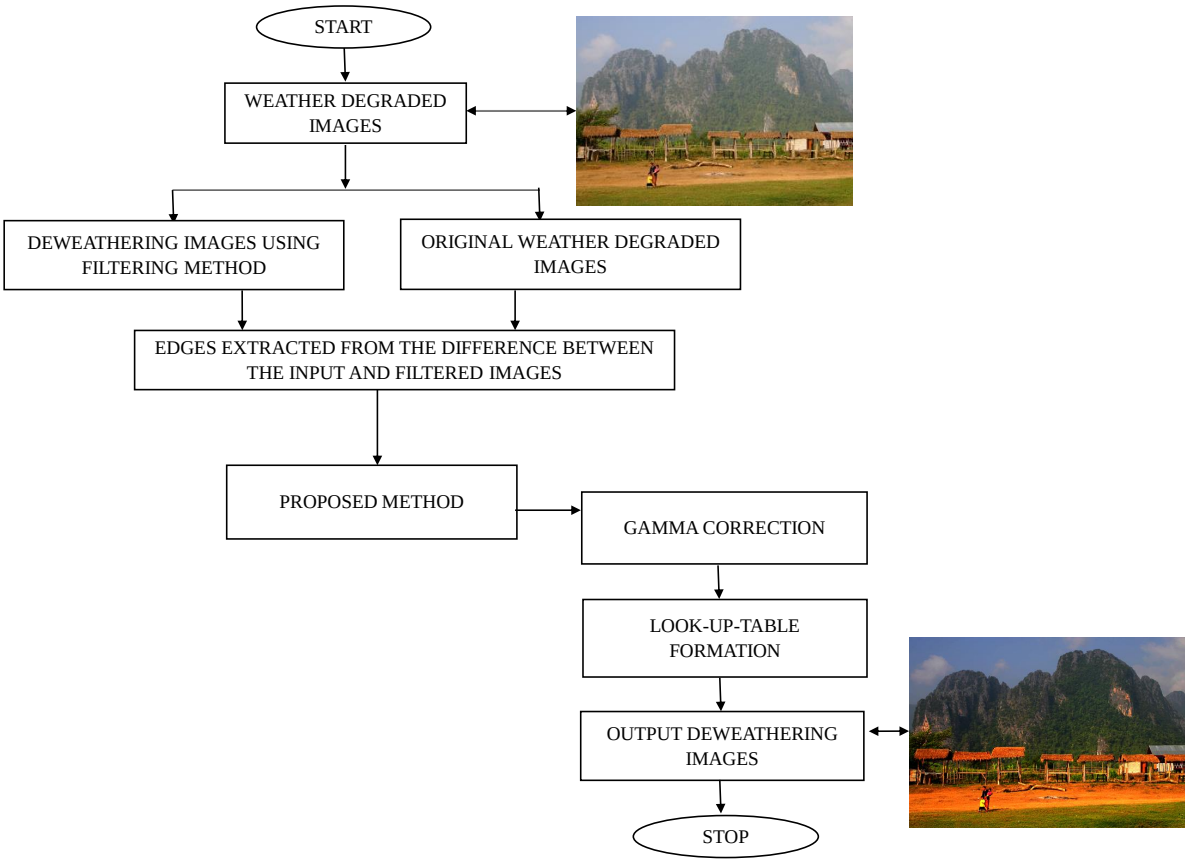


FIGURE 3.2: Flowchart of the proposed algorithm

4. Multiply Constant gain factor with the edges extracted from the difference.

5. Perform image addition of the edge extracted and original image to remove the artifacts present in the images.

6. Calculate the maximum pixel intensity present in the images.

7. Use the gamma correction is used for proper selection of gamma value. Gamma correction allows users to better match the intensity.

8. Look-up-table method is used to get the final enhanced image.

9. Output deweathering image.

The deweathering image recovered by the proposed approach is shown in Figs. 3.3 (d), 3.3 (e) and 3.3 (f) for Figs. 3.3 (a), 3.3 (b) and 3.3 (c). Our proposed method can enhance a color image without generating halo artifacts or distorting the color.

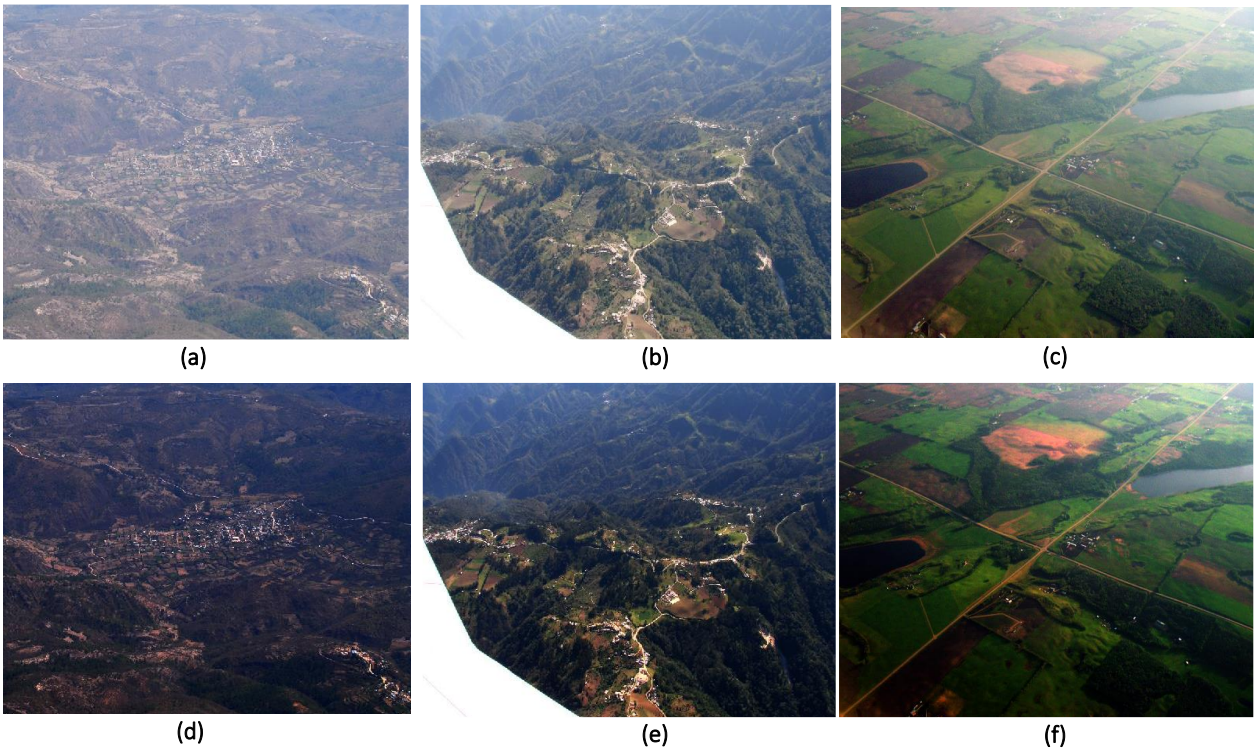


FIGURE 3.3: (a), (b) and (c) Weather degraded images (d), (e) and (f) Restored images by the proposed algorithm

### 3.2.2 Video Dehazing and Defogging using Look-Up-Table Approach

There are only few existing methods to enhance weather degraded video sequences. However, these methods still consumes considerable time, so that it is hard to satisfy real-time requirement for some applications, especially for high video quality applications.

We have extended the same approach for enhancing the weather degraded videos. Our method applies to a series of video frame to enhance a video sequence. Fig. 3.4 shows the flowchart of video deweathering approach. At the beginning of the process, the first incoming frame is the processing frame of the video. Median filter is used for filtering the videos. The size of the window is used as $3 \times 3$ which reduce the time complexity. Here simple frame subtraction has been used to extract the edges of the foreground part. After that the edge extracted from the foreground part and previous frame is added to remove the artifacts present in the video. For the weather degraded video used as input, most of the pixels are densely distributed in the

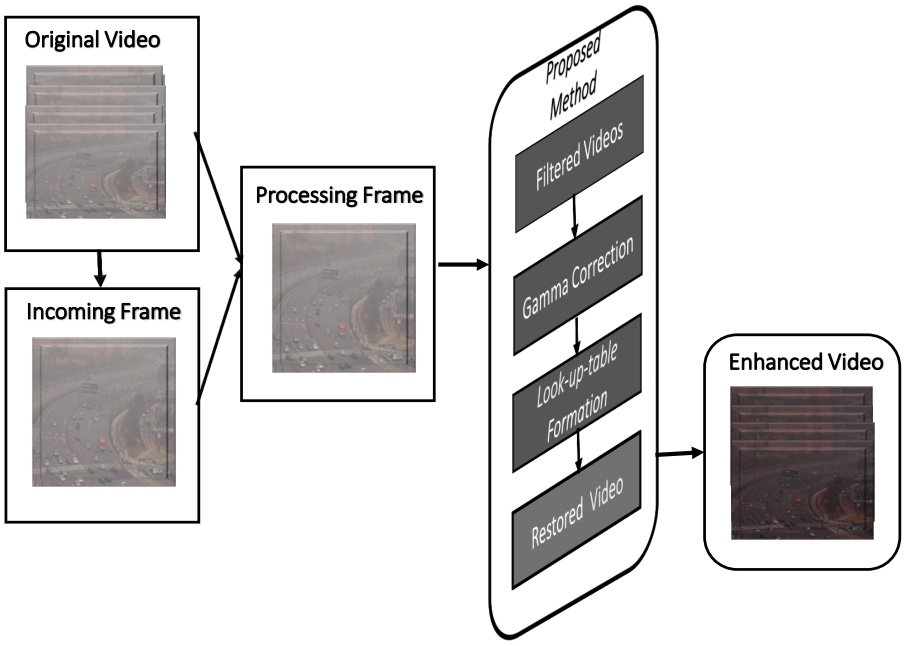


FIGURE 3.4: Video dehazing flow chart.

low-level region. So, gamma correction method is used to enhance a video without generating artifacts or distorting the color. At last, LUT method is used to get the final enhanced video. By applying our method, the processing rate is greatly improved and color distortion is avoided.

## 3.3 Comparison and Experimental Results

In order to demonstrate the effectiveness and robustness of our proposed algorithm, we have experimented with our method as well with best reported algorithms (Tan [27], Fattal [28], He et al. [30], Tarel et al. [32] and Wang et al. [51]) on a large set of weather degraded images and videos. Initially we have done the qualitative assessment extensively based on visual appearance for image followed by video. Next we considered the important quantitative parameters in terms of blind contrast restoration assessment [45] method ($e$, $r$), PSNR (peak signal to noise ratio) and processing time for both image and also for video. Processing time is the time taken by a processor to process an image or video using a particular algorithm. The time taken to process depends on the processor, the simulator, image sizes and time complexity of the algorithm itself.

Processing time is an important performance metric while considering a real time application. We have analyzed the effect of different size of images on processing time and compared our approach with the best reported fast algorithms i.e. Tarel et al. [32] and Wang et al. [51] method.

### 3.3.1 Qualitative Evaluation for Image and Video

In this subsection we have compared with five methods (Tan [27], Fattal [28], He et al. [30], Tarel et al. [32] and Wang et al. [51]) in terms of visual quality of the images and videos. Qualitative results of selected deweathering algorithms are shown in Fig. 3.5. Fig. 3.5 (a) shows the original weather degraded color images followed by enhanced images of the various dehazing algorithms. The dehazed image obtained by Tan [27] is shown in Fig. 3.5 (b). This algorithm is applicable for both color and gray images. However, it does not recover the original color of the scenes. Fig. 3.5 (c) shows dehazed image by Fattal [28] algorithm. Fattal [28] algorithm yields more natural results. However, this approach cannot well handle heavy haze images. Again the Fattal [28] algorithm is based on the color information; hence, this method cannot be applied to the gray image. Fig. 3.5 (d) shows dehazed image by He et al. [30] algorithm. He et al. [30] have introduced a novel dark channel prior method. This method gives better results, but the processing time is high as transmission map is refined by using soft matting. Fig. 3.5 (e) shows dehazed image by Tarel et al. [32] algorithm. Tarel et al. [32] proposed a fast visibility restoration algorithm using minimum channel and median filter. So, this algorithm is computationally less complicated and less processing time as compared to other conventional method, but it changes color tone and exhibits halo artifacts. The enhanced image by our proposed method is given in Fig. 3.5 (f). The visual analysis of the enhanced images in Figs. 3.5 (a)- 3.5 (f) indicates that the proposed method gives better result in comparison to other proposed algorithm.

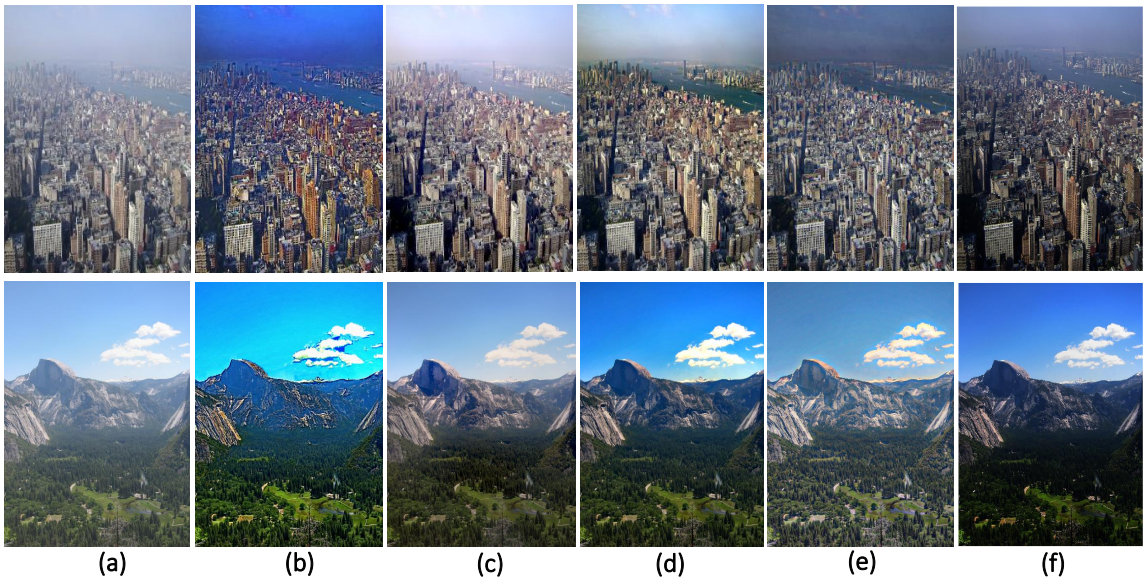


FIGURE 3.5: (a) Original color image (b) Tan algorithm [27], (c) Fattal algorithm [28], (d) He et al. algorithm [30], (e) Tarel et al. [32], and (f) the proposed algorithm (from top to bottom image name ny17, y01).

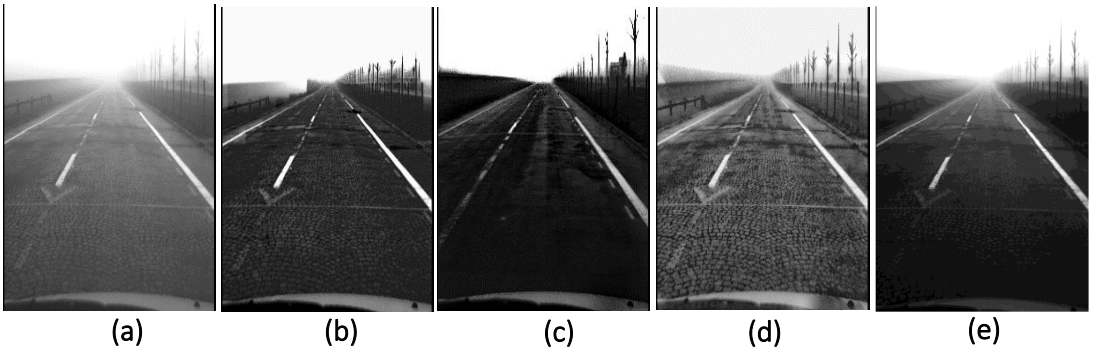


FIGURE 3.6: (a) Original gray image (b) Tan algorithm [27], (c) He et al. algorithm [30], (d) Tarel et al. [32], and (e) the proposed method.

For comparing our dehazing approach for gray images, a gray image is processed by other best algorithms and using our proposed method. The performance of various approaches is shown in Fig. 3.6. Fig. 3.6 (a) shows original gray image. Figs. 3.6 (b), (c) and (d) are dehazed images by Tan [27], He et al. [30] and Tarel et al. [32] respectively. These three algorithms are applicable for gray images. Fattal [28] algorithm is not applied for grayscale images because this method is basically a statistic interpretation that requires variance to estimate the depth map. Fig. 3.6 (e) is enhanced image by using our approach. The visual analysis of the enhanced

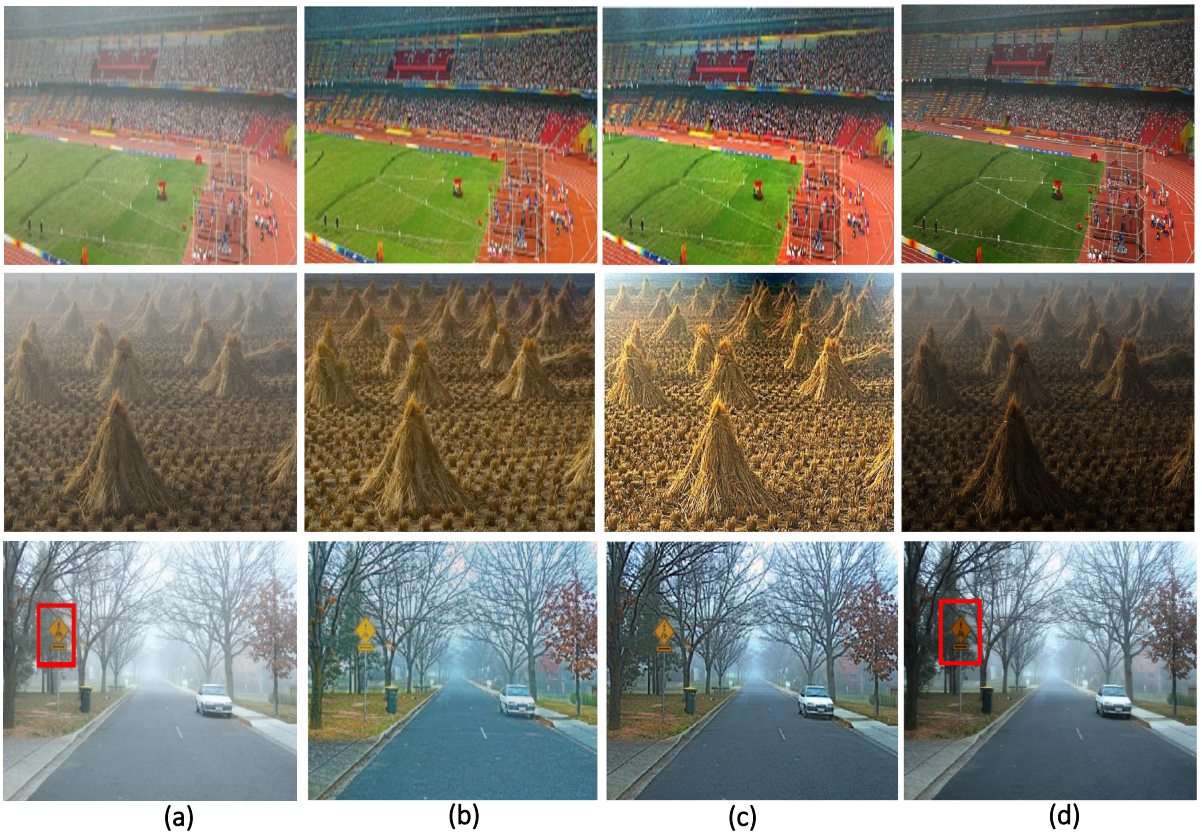


FIGURE 3.7: (a) Original color image, (b) Tarel et al. [32], and (c) Wang et al. method [51], (d) the proposed method.

images in Figs. 3.6 (a)-(e) indicates that the proposed method gives better result in comparison to other proposed algorithm for gray image. So we can conclude that our approach is suitable for both color and gray images.

Next, Our approach is compared with Tarel et al. [32] and most recent Wang et al. [32] method. Recently, Wang et al. [51] proposed a fast dehazing method which is based on a fusion and image enhancement method. This method is slightly faster than Tarel et al. [32] method. In Fig. 3.7 (a) original images are shown. The enhanced images by Tarel et al. [32] are shown in Fig. 3.7 (b). Fig. 3.7 (c) shows dehazed image by Wang et al. [51] method. Fig. 3.7 (d) shows deweathering image by our proposed method. In Fig. 3.7, it is observed that the yellow color sign board in "road" image is more faithfully reconstructed using our method, similarly for "cone" and "stadium" images.

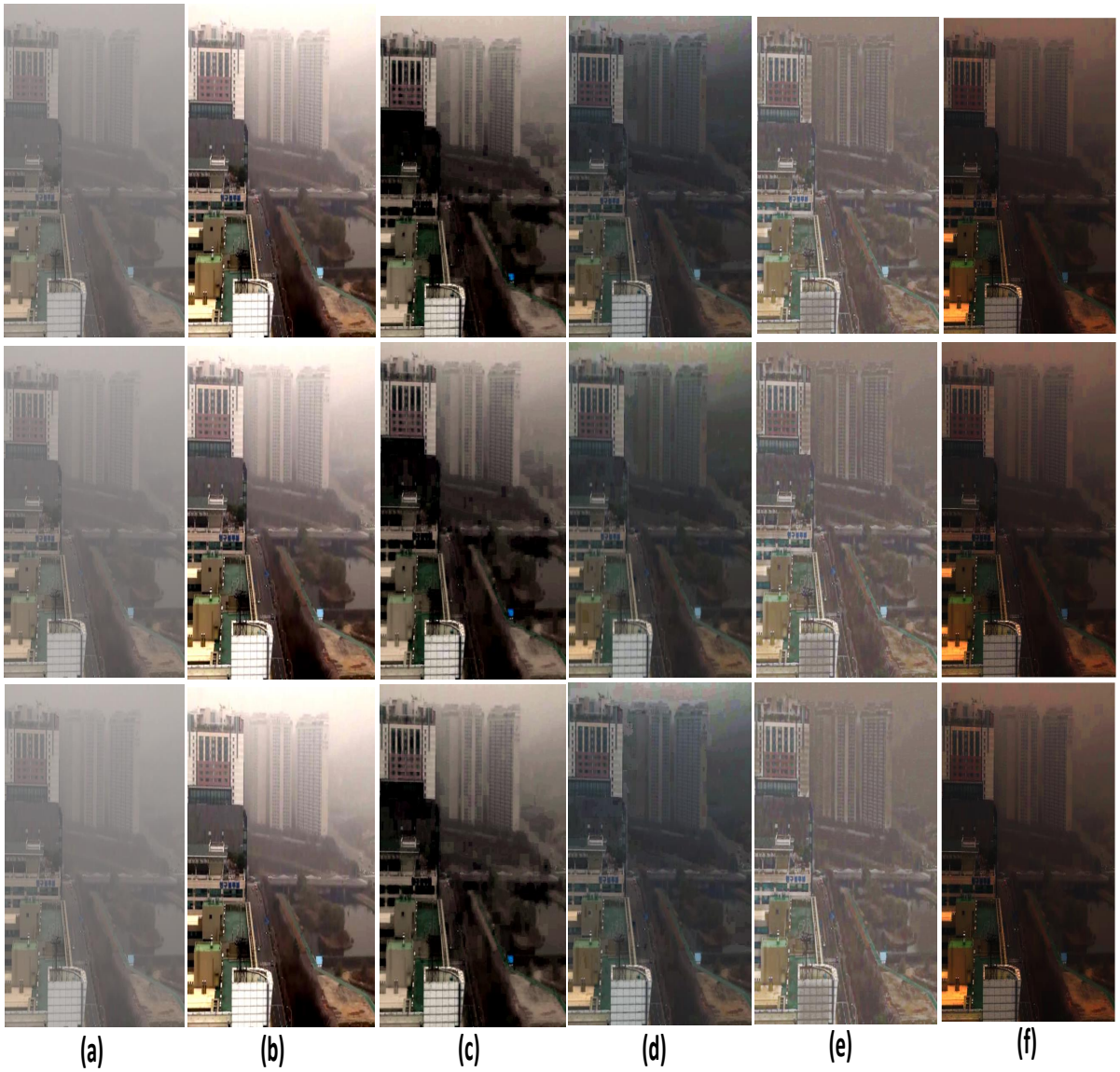


FIGURE 3.8: Video deweathering on the "Riverside" sequence. (a) Three frames in a foggy video, (b) The result using Tan method (c) The result using Fattal method (d) The result using He et al.method (e) The result using Tarel et al. method and (f) The result using the proposed method. From top to bottom, the frame numbers are 10, 12, and 14, respectively.

After a thorough analysis of static images we worked on videos. We have taken weather degraded videos, "Riverside," and "Road View," sequences from Kim's project page [52] and applied our approach to it. To the best of our knowledge, there is no algorithm specifically given for foggy and hazy videos. However, in prior work [32], it is mentioned that the existing methods (Tan [27], Fattal [28], He et al. [30] and Tarel et al. [32]) can be extended for video by making use of the temporal correlation present among frames. We have extended the existing methods

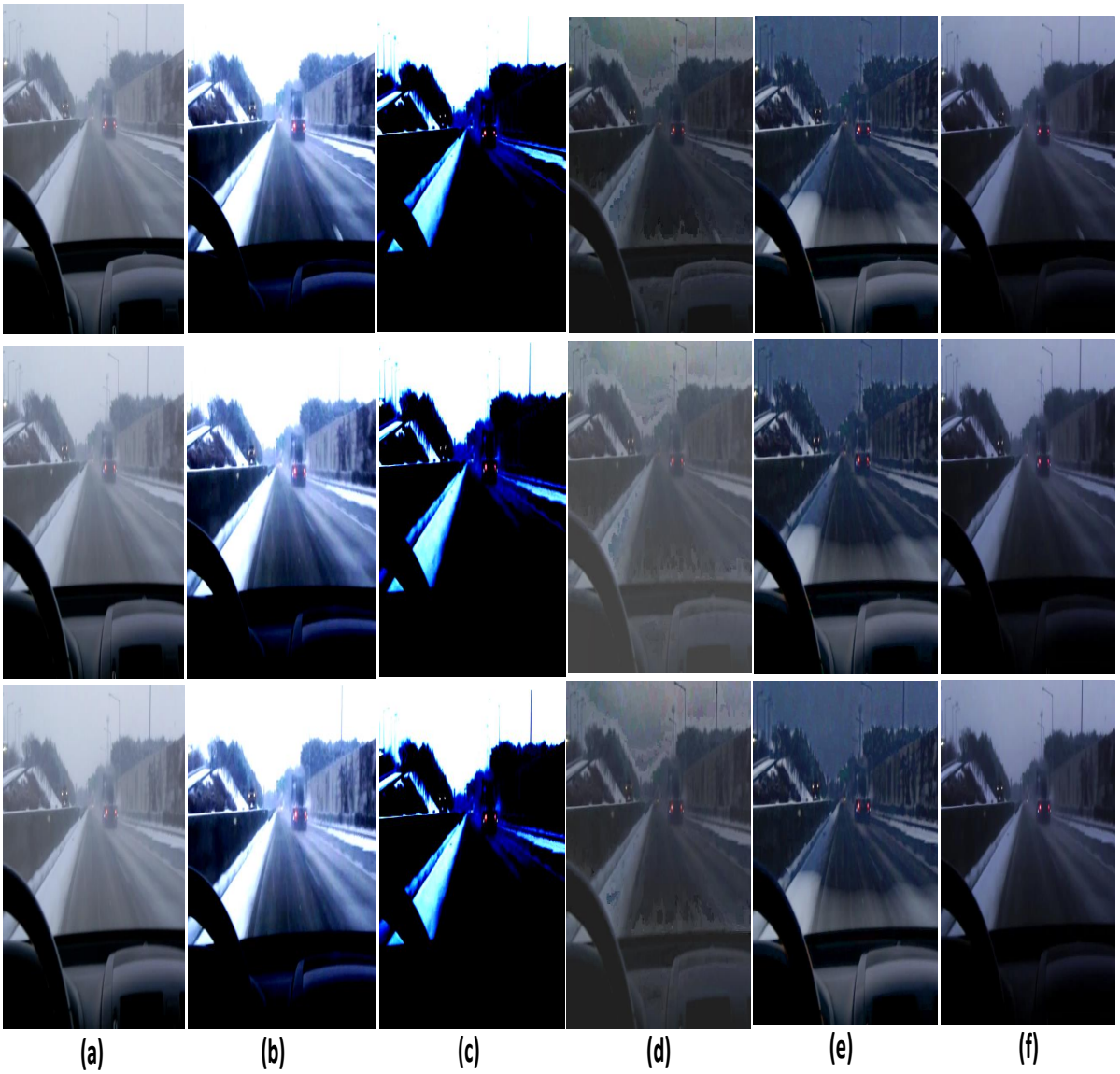


FIGURE 3.9: Video deweathering on the "Road View" sequence. (a) Three frames in a foggy video, (b) The result using Tan method (c) The result using Fattal method (d) The result using He et al. method (e) The result using Tarel et al. method and (f) The result using the proposed method. From top to bottom, the frame numbers are 7, 9, and 11, respectively.

as well as our proposed approach for two standard videos for fare comparison. First, we compare our approach with Tan [27] method. Figs. 3.8 (b) and 3.9 (b) show the restored video frame using Tan method. This method even though maximizing the contrast of the images but due to the overstretching of the contrast it contains halo artifacts. We also compare our result with Fattal [28] method. The results of the video frame using Fattal method are shown in Figs. 3.8 (c) and 3.9 (c). This method gives more natural results, but it cannot adequately remove haze

and fog in some regions which is visible in the restore frames. Next, in Figs. 3.8 (d) and 3.9 (d), we compare the proposed method with He et al. [30] method. This method depends only the dark pixel values, the information loss is more if bright pixels are present in images. Tarel et al. [32] method cannot completely eliminate the halos which can be seen from Figs. 3.8 (e) and 3.9 (e). Figs. 3.8 (f) and 3.9 (f) show the restored deweathering, video frame using the proposed method. The proposed method provides more reliable deweathering performance than existing work. Our method diminishes halo artifacts and gives more natural results as compared with existing methods. The deweathering results are appreciably improved by using the method which we proposed. The processing speed of the video which can validate that the proposed method is more suitable for real time processing is discussed next.

### 3.3.2 Quantitative Evaluation for Image and Video

For the quantitative analysis, blind contrast restoration assessment proposed by Hautieren et al. and PSNR is used. The blind contrast restoration assessment method $e$ and $r$ are discussed in equs. (2.29) and(2.30). To determine the overall quality of the images, PSNR indicator is used. PSNR is a statistical measurement used for image or video quality assessment. PSNR is defined as the mean square error (MSE) of two $M \times N$ images $x$ and $x'$, where one of the image is considered a noisy counterpart of the other. The PSNR is calculated as follows [15].

$$PSNR = 10log\frac{(2^s - 1)}{MSE} \tag{3.2}$$

where, MSE is given by:

$$MSE = \frac{1}{MN}\sum_{i=0}^{M-1}\sum_{j=0}^{N-1}\left(x_{ij} - x'_{ij}\right)^2,\ 0 \leq i \leq M-1,\ 0 \leq j \leq N-1 \tag{3.3}$$

TABLE 3.1: **Quantitative and Processing Time Comparison for Image**

| Image | Method | e | r | PSNR | Time/second |
|---|---|---|---|---|---|
| **ny17** | Tan | 0.0356 | 2.0234 | 59.0426 | 19.79 |
| | Fattal | 0.0340 | 1.4094 | 69.2153 | 2.92 |
| | He et al. | 0.0155 | 1.5448 | 66.0207 | 28.79 |
| | Tarel et al. | -0.0139 | 1.5311 | 59.1575 | 2.80 |
| | Proposed method | 0.1056 | 1.1879 | 56.0229 | 0.88 |
| **y01** | Tan | 0.0190 | 2.2723 | 56.7941 | 19.79 |
| | Fattal | 0.0171 | 1.1682 | 66.5738 | 2.92 |
| | He et al. | 0.0141 | 1.3740 | 58.9532 | 28.79 |
| | Tarel et al. | -0.0098 | 1.8463 | 63.9328 | 2.80 |
| | Proposed method | -0.0264 | 1.1749 | 59.2802 | 0.73 |
| **Road image** | Tan | 0.838 | 1.8976 | 62.0133 | 9.76 |
| | He et al. | 0.7060 | 1.7915 | 58.4418 | 20.16 |
| | Tarel et al. | 0.5875 | 2.7153 | 66.2975 | 2.10 |
| | Proposed method | 0.7604 | 1.917 | 59.0297 | 0.45 |

where $x_{ij}$ is the original image, $x'_{ij}$ is the dehazed image, $M$ and $N$ represent the image size, $(2^s - 1)$ corresponds to the theoretical maximum intensity value of the image and s is the depth of the image ($s = 8$).

Table 3.1 shows the comparison results of the existing methods and proposed method in terms of $e$, $r$, PSNR value and processing time. In Table 3.1 three standard images (i.e. ny17, y01 and Road image) are considered. Our method is compared with Tan [27], Fattal [28], He et al. [30] and Tarel et al. [32]. Generally, a larger PSNR values implies a better visual quality of the images. In our case, comparable PSNR results along with e and r show the enhanced contrast deweathering image without losing any visual appearance. The resultants are shown in Figs. 3.5 (f), 3.6 (e), 3.8 (f) and 3.9 (f), respectively, where it is evident that the proposed approach is capable of enhancing the quality of the images.

Next, the processing time comparison of different algorithms are considered. Analyzing the results of Table 3.1, Tan [27] and He et al. [30] method need more than 10 and 20 second per image. Fattal [28] method needs more than 2 second for processing the images. Tarel et al. [32] method takes 2 second per image. It is clear that the computational complexity of the proposed method is very less along with enhance the contrast of the restored image.

Computational complexity plays an important role for real time processing and this complexity varies with different image sizes. We have compared processing time with the best reported dehazing algorithms such as Tarel et al. [32] and Wang et al. [51] method by simulating all of them on the same hardware platform. For fare comparison, three images of size 465 x 384, 600 x 400 and 1000 x 327 are taken as input original image. The processing time for different image sizes using Tarel et al. [32] and Wang et al. [51] method is obtained as 1.57 sec, 2.08 sec, 2.86 sec and 1.46 sec, 1.87 sec, 2.49 sec respectively. The processing time for our method for same three figures are obtained as 0.659 sec, 0.997 sec and 1.159 sec. So as compared with Tarel et al. [32] and Wang et al. [51], our method takes less processing time. For a quantitative comparison, the speed improvement over Tarel and Wang are obtained and summarized in the last two columns of Table 3.2. It is found that the proposed approach is faster by up to 48% and 53% in comparison to Tarel and Wang methods respectively. The speed improvement of our method is better because of the use of only one median filter and look-up-table method which take less computation time as compared to Tarel et al. [32] and Wang et al. [51] method. Tarel et al. [32] need to apply a median filtering on the median. This means that their method must

TABLE 3.2: **Processing time comparison (in sec) with Tarel and Wang for different image sizes**

| **Image Sizes** | **Tarel** | **Wang** | **Our** | **% improvement w.r.t. Tarel** | **% improvement w.r.t. Wang** |
|---|---|---|---|---|---|
| | **Time/second** | | | | |
| **465x384 (s)** | 1.57 | 1.46 | 0.659 | 41.9 | 45.1 |
| **600x400 (s)** | 2.08 | 1.87 | 0.997 | 48.0 | 53.3 |
| **1000x327 (s)** | 2.86 | 2.49 | 1.159 | 41 | 46.5 |

TABLE 3.3: **Quantitative Estimation of Video Deweathering**

| Weather degraded input sequence | | Tan | | | | Fattal | | | |
|---|---|---|---|---|---|---|---|---|---|
| | | **e** | **r** | **PSNR** | **Time** | **e** | **r** | **PSNR** | Time |
| **River side** | **Frame no. 10** | 0.1051 | 2.1055 | 59.3692 | | 1.0954 | 1.2103 | 55.5941 | |
| | **Frame no. 12** | 0.1378 | 2.1052 | 59.3716 | 14.4536 | 0.0995 | 1.9499 | 55.5579 | 8.18442 |
| | **Frame no. 14** | 0.1652 | 2.1059 | 59.3627 | | 0.1302 | 1.9433 | 55.5454 | |
| **Road View** | **Frame no. 7** | 1.3857 | 1.4352 | 56.6065 | | 0.1096 | 1.2681 | 56.2881 | |
| | **Frame no. 9** | 1.2680 | 1.4364 | 56.6223 | 15.9270 | 0.0850 | 1.2895 | 57.8902 | 10.6871 |
| | **Frame no. 11** | 1 | 1.4641 | 56.6105 | | 0.1616 | 1.2875 | 58.0679 | |

| Weather degraded input sequence | | He et al. | | | | Tarel et al. | | | | Proposed method | | | |
|---|---|---|---|---|---|---|---|---|---|---|---|---|---|
| | | **e** | **r** | **PSNR** | **Time** | **e** | **r** | **PSNR** | **Time** | e | **r** | **PSNR** | **Time** |
| **River side** | **Frame no. 10** | 0.1308 | 1.4110 | 58.2038 | | 0.0318 | 1.8352 | 61.5819 | | -0.0857 | 1.4414 | 64.2456 | |
| | **Frame no. 12** | 1.5689 | 0.6947 | 55.9097 | 740.662 | 0.0587 | 1.8391 | 61.5809 | 3.4220 | -0.0756 | 1.4114 | 64.3277 | 1.775 |
| | **Frame no. 14** | -0.1239 | 1.4930 | 58.7705 | | 0.0638 | 1.8464 | 61.5586 | | -0.0700 | 1.3231 | 64.2390 | |
| **Road View** | **Frame no. 7** | -0.9967 | 1.0211 | 57.1285 | | 0.8140 | 1.3918 | 56.1858 | | 0.3555 | 0.9679 | 60.2669 | |
| | **Frame no. 9** | -0.9967 | 0.8449 | 58.2099 | 852.713 | 0.8268 | 1.4023 | 56.1966 | 4.879 | 0.2876 | 0.9599 | 60.2392 | 2.270 |
| | **Frame no. 11** | 0.2195 | 0.9759 | 57.6657 | | 0.6128 | 1.4075 | 56.2080 | | 0.0152 | 0.9606 | 60.2593 | |

be carried out by two median filters. So the processing time of Tarel et al. [32] is more than our computational time. The computational complexity of Wang et al. [51] method is the minimum filter approach. The processing time is less than Tarel et al. [32] method and it is almost close to it. Therefore, our method is better than Tarel et al. [32] and Wang et al. [51].

Table 3.3 shows the comparison results for video deweathering in terms of $e$, $r$, PSNR value and processing time. In Table 3.3 two standard videos ("Riverside," and "Road View,") are investigated. We have compared our method with Tan [27], Fattal [28], He et al. [30] and Tarel et al. [32]. Here, Figs. 3.8 (f) and 3.9 (f) show the video deweathering frames using our approach. Furthermore, our algorithm achieves higher PSNR values for these videos. If the excessive contrast is present in the restored video frame by Tan [27], the color of the fog free is often oversaturated and looks unnatural, e and r value will be very high and artifacts are present in the recovered images and video frames.

For obtaining average processing time, the same two standard videos of 30 frames per second are taken. The existing methods as well as our proposed approach are applied to both

the videos. The processing time obtained for both the videos of one second duration consisting of 30 frames are listed in Table 3.3 and gives here for ready reference. The result shows, Tan [27] algorithm takes almost 14 to 15 second for processing one second duration video. So, this method is not suitable for real time processing. Fattal [28] method also takes 8 to 10 second for processing the average of 30 frames. He et al. [30] approach is computationally expensive. Tarel et al. [32] method is computationally less complicated and a good candidate for the video application in future. But in comparison with this method, our approach is taking almost half the processing time. This results approves that the significant improvement in speed of the proposed algorithm. Thus, the proposed method is more suitable for real time implementation of the fog and haze removal of restored videos without losing any visual quality.

## 3.4 Conclusion

In this chapter, we propose a new method for enhancing the image and video by using look-up-table method. The main contribution of our method is in terms of less processing time as compared with other existing methods without sacrificing the enhanced quality. Less processing time allows the LUT based weather degraded image enhancement method to be applied in real-time processing applications. We apply a median filter and gamma correction using look-up-table method to enhance the weather degraded images. Our approach is giving a better result with speed improvement up to 48 % and 53 % as compared with the references [32] and [51]. Experimental results demonstrate that the proposed algorithm has a significant effect on deweathering, as well as achieving real-time video processing. However, this approach may fail when handling heavy foggy image and video. So, in order to balance between processing time and handling of heavy foggy images and videos, image restoration methods are investigated and which are discussed in following chapters.

# Chapter 4

# Visibility Restoration for Haze and Fog Affected from Image and Video

In the hazy and foggy conditions, the color and contrast of outdoor scene decreases. This significantly reduces the quality of captured images and videos, which is essential for all outdoor imaging and video recording systems. To overcome this problem, a real-time image and video dehazing and defogging is extremely important. In this chapter, we present restoration based approach for real time haze and fog removal from a single input image and video. The process of removing haze and fog from an image and video requires the knowledge of physical characteristics of the scene. One of the characteristics is the airlight. This is light coming from the environmental illumination and scattered by the atmospheric and coming towards camera. Another important characteristic is a transmission map or depth map of the scene. This depth is measured from the camera to the objects in the scene. If airlight and depth map are known, then the problem of removing haze or fog can be resolved with ease.

## 4.1 Introduction

Road accidents are common during bad weather conditions. As per National Highway Traffic Safety Administration (NHTSA), few of the most usual reasons for road accidents are distracted driving, bad weather conditions and driving at a speed that is greater than the legal limit. Among all these, one of the primary reasons is inclement weather conditions. According to the World Health Organization (WHO), India deteriorated to the highest number of road accidents in the world in the year 2010. In India, nearly 10-15% of car accidents occurred during foggy, hazy and rainy conditions. Driving in foggy weather is more difficult than clear weather. In bad weather conditions, visibility can be degraded due to the presence of particles such as haze and fog. The degraded images and videos always have less brightness and bad color quality. These degraded images and videos reduce the visibility and make the vision-based analysis more difficult.

Fog detection is a difficult task because degradation varies spatially, i.e., it depends on local weather conditions. Furthermore, if only single foggy and hazy image is available, then the problem is more complicated and challenging. Many haze removal techniques have been proposed to restore the hazy images and videos. Kopf et al. [53] introduced an interactive method of manually registering the hazy image with existing 3D geometrical model. This approach requires additional information provided by user interaction. He et al. [29] proposed a method based on dark channel prior for single image dehazing. This method may be invalid when the scene object is almost similar to the airlight. Though all these dehazing methods based on a single input image can get good results, but it is difficult to obtain for video dehazing due to the limitation of the processing time. John et al. [31] proposed a novel method which is based on the wavelet fusion method. This method provides better visibility results and high contrast. But this method is not tested and verified for real time video processing for fog and haze removal.

Tarel et al. [32] proposed an algorithm based on median filter. This method may be used for real time system. But the restored image quality is not good when there are discontinuities present in the scene depth.

In this chapter is that a new approach based on restoration for real time deweathering of images and videos is proposed. The real time dehazing and defogging are accomplished by three major steps: atmospheric light estimation, transmission map estimation and scene restoration. These three steps make it possible to produce a real time image and video deweathering. There are six sections in this chapter, including this section. Section 4.2 presents a detailed description of the atmospheric dichromatic model. Section 4.3 introduces contrast restoration approaches for foggy and hazy image and video. In this section, we have discussed about the state-of-the-art and also proposed method for contrast restoration based on estimating the airlight and transmission map. In section 4.4, we recover the scene radiance. In section 4.5 experimental results are discussed in terms of performance metrics. It is observed that the performance of the proposed algorithm compares with the state of the art. Section 4.6 concludes this chapter.

## 4.2 Atmospheric Dichromatic Model

In atmospheric dichromatic model, the captured image is degraded by two components. One is the direct transmission and other is airlight. The reflected light beam coming straight from an object point to the camera is direct transmission and the light which is coming from the environmental illumination is scattered by the atmospheric particle and coming towards camera is airlight. The dichromatic model is described as follows [54]:

$$I(x, y, \lambda) = J(x, y, \lambda)t(x, y, \lambda) + A(\lambda)(1 - t(x, y, \lambda)) \tag{4.1}$$

where, $I(x, y, \lambda)$ is the hazy pixel at location $(x, y)$ with wavelength $\lambda$, $J(x, y, \lambda)$ is the image intensity without haze and fog, $A(\lambda)$ is the atmospheric light, and $t(x, y, \lambda)$ is the medium transmission. The medium transmission map is an exponentially decaying function. This term is described by:

$$t(x, y, \lambda) = e^{-\beta(x,y,\lambda)d(x,y)} \tag{4.2}$$

where, $d(x, y)$ is depth of the scene and $\beta(x, y, \lambda)$ is the scattering coefficient. Since equation (4.1) has three unknown parameters, to get the deweathered image is an ill posed problem. To overcome this, we assume that the atmosphere is homogeneous, so that $\beta(x, y, \lambda) = \beta(\lambda)$. For hazy and foggy images Narasimhan et al. [1] make an additional assumption that the scattering is color independent. By this assumption the estimated transmission map is $t(x, y) = e^{-\beta d(x,y)}$. The atmospheric dichromatic model is simplified to:

$$I(x, y) = J(x, y)t(x, y) + A(1 - t(x, y)) \tag{4.3}$$

Haze and fog removal is achieved by calculating the $J(x, y)$, $A$, $t(x, y)$ from Eq.(4.3). Apparently, it is ill-posed problem because $A$ is the first unknown and the transmission $t(x, y)$ is second unknown for recovering the scene radiance. In this work, we will estimate airlight and transmission map accurately in order to remove fog and haze from images. Therefore, the key problem in single image defogging and dehazing are estimating airlight and transmission map given a foggy and hazy images.

## 4.3 Contrast Restoration for Foggy and Hazy Image and Video

The fog and haze removal of images and videos are possible by two methods; estimation of atmospheric light, estimation and refinement of transmission map. A combination of these

two approaches can also be used for contrast restoration. In this section, we present a new approach for fog and haze removal from images and videos based on estimation and refinement of atmospheric light and transmission map. In the first subsection, we discuss the state-of-the-art techniques for contrast restoration based on atmospheric light. In the next subsection, we discuss the state-of-the-art techniques for estimating and refining the transmission map. Finally, we present our approach for deweathering the images and videos.

### 4.3.1 Review of the Atmospheric Light based Contrast Restoration Techniques

In state-of-the-art methods, the algorithms to estimate the atmospheric light were based on the dark channel prior method proposed by He et al. [30]. The prior knowledge of dark channel is obtained from the observation of the image without fog and haze in outdoor condition. In most of the non-sky patches, at least one color channel has very low intensity at some pixels. In other words, the minimum intensity in such a patch should have a very low value. Therefore, for an image I, dark channel is given by,

$$J^{dark}(x,y) = \min_{c\varepsilon\{r,g,b\}} ( \min_{(x,y)\varepsilon\Omega} (J^c(\Omega))) \tag{4.4}$$

where, $J^c$ is a color channel of $J$, $c\varepsilon\{r,g,b\}$ is color channel index and $\Omega$ is a local patch in the image. In most of the single image methods, the atmospheric light component $A$ is usually estimated from the most fog-opaque pixel, such as the pixel with the max intensity value. Therefore, the top 0.1% brightest pixels in the dark channel are first selected. Among these pixels, the pixels with highest intensity in the input image are selected as the atmospheric light. In [36], the top 0.2% brightest pixels in the dark channel are selected. But, this method leads an incorrect selection of atmospheric light when the white object are present in the image. To estimate atmospheric light reliably, Kim et al. [43] presented a hierarchical searching method

based on the quad-tree subdivision. This method can recognize the brightest region in the image. However, this method also does not produce satisfactory results if the brightest pixels are also the objects of the image. To address this problem, we have proposed thresholding based atmospheric light estimation.

### 4.3.2 Review of Techniques for Estimation and Refinement of Transmission map

To remove fog and haze from a single image is a challenging task in computer vision, because insufficient information is available for estimating the transmission map. In traditional state-of-the-art methods, single fog image contains sufficient information to directly estimate the depth map, while single image defogging is still ill-posed and needs fog priors to resolve it [55]. This method supposes that the transmission and the surface shading are not locally correlated. But this method is not valid for dense fog. He et al. method [30] used dark channel prior method for estimating the transmission map and refined by soft matting method, which could be computationally intensive. To overcome this problem He et al. [41] proposed a guided filter which is an approximate solution of the soft matting method. This method greatly reduced the computational complexity. Other approaches such as median of median filter [23], guided joint bilateral filtering [36] and bilateral filter [37] are also used for replacing time consuming soft matting method. Currently guided filter is one of fastest edge preserving filter. It is derived from a local linear model which generates the filtering output by considering the guidance image. This filter has the edge smoothing property like the bilateral filter, but suffers from the gradient reversal artifacts.

Next, Nishino et al. [56, 57] proposes a probabilistic dehazing method, which models the image with a factorial Markov Random Filed to estimate the scene radiance and the depth

information. This approach can recover most details from the hazy image, but the result suffers from oversaturation. In [58] Zhang et al. proposed a local albedo insensitive image dehazing method. This method is based on an iterative bilateral filter. This algorithm gives good results. Due to the use of iterative bilateral filter this technique is computationally intensive and requires a choice of number of parameters for optimal results. To overcome these issues, we have proposed median dark channel prior (MDCP) based approach for refining the transmission map.

### 4.3.3 Visibility Restoration by Thresholding and Median Dark Channel Prior based Approach

For optimal solution of enhancing the contrast and reducing the computational complexity of the outdoor images taken in bad weather conditions a combination of thresholding and MDCP based method is proposed for estimating and refining the atmospheric light and transmission map. Fig. 4.1 shows the corresponding flow chart for haze and fog removal from images. We obtained

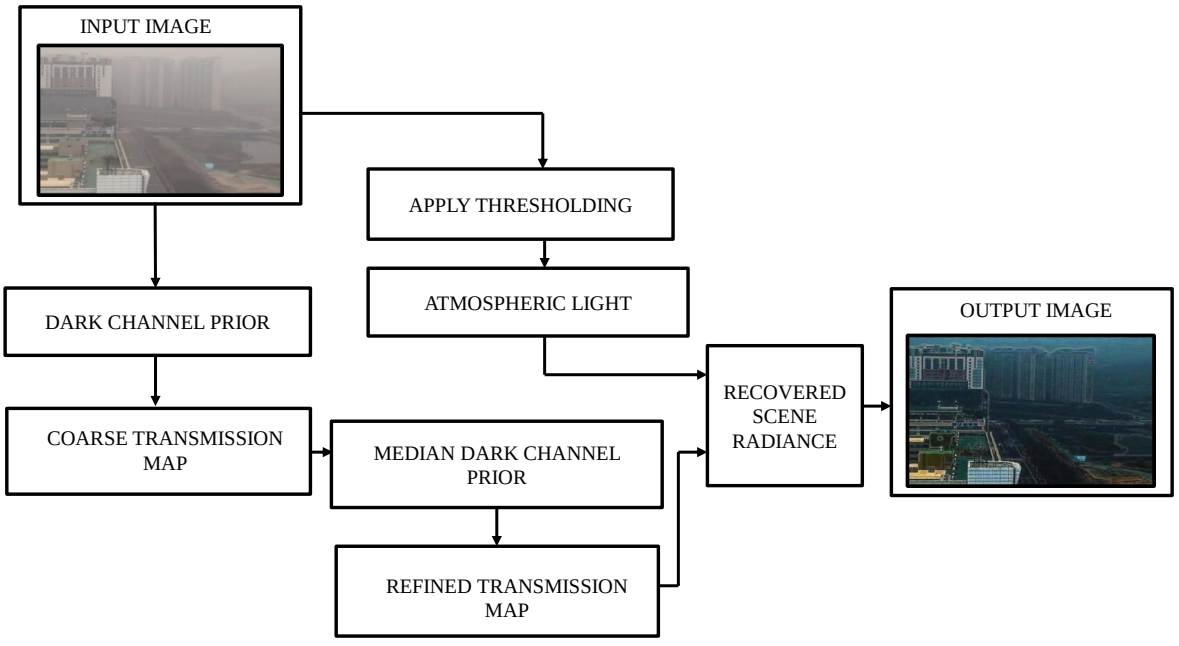


FIGURE 4.1: Flow diagram for estimating atmospheric light and transmission map using thresholding and median dark channel prior metod

hazy and foggy images. Firstly, we estimated the atmospheric light by applying the thresholding method. Coarse transmission map is calculated by using dark channel prior method. The estimated coarse transmission map still contains artifacts. For refining the coarse transmission map, MDCP is used. Finally the fog-free image is recovered. The detailed description of this process is given below.

#### 4.3.3.1 Estimating the Atmospheric light using Thresholding method

Thresholding is a simple but effective method for image processing, especially in the fields where real time processing is needed. It is useful for extracting foreground from the background by proper selection of threshold value. This method can be expressed as:

$$g(x,y) = \begin{cases} 1 \quad if \quad f(x,y) > T \\ \\ 0 \quad if \quad f(x,y) \leq T \end{cases} \tag{4.5}$$

where, $g(x,y)$ is threshold image, $f(x,y)$ is the gray level image pixels and $T$ is the threshold value.

We proposed a new approach to find the atmospheric light directly from the images rather than from the dark channel prior. We first give a threshold to the intensity values to eliminate the non-atmospheric light intensities. After this, from the obtained set of high intensity values, we find the mode of the set, i.e., the number to be repeating the maximum number of times in the set. This is observed to be the atmospheric light value of that particular channel. By this method we obtain three atmospheric light values for the three channels. This method has been formulated with the view that atmospheric light intensity could be considered as that which is most spread in the high intensity area, rather than the maximum intensity or the average intensity.

#### 4.3.3.2 Estimating the Coarse transmission map using Dark Channel Prior method:

The coarse transmission map is calculated using He et al. [30] which uses dark channel prior method. The coarse transmission map is given by following equation

$$\tilde{t}(x) = 1 - w \min_{(i,j)\varepsilon\Omega(x,y)} ( \min_{c\varepsilon\{r,g,b\}} (\frac{I^c(i,j)}{A^c})) \tag{4.6}$$

where $w$ is a weighting factor and its value is application based. The parameter $w$ is used to prevent removing the haze thoroughly and keep the feeling of depth, it is set to be 0.95. The transmission obtained by equation (4.7) is only a coarse transmission map. The recovered image using the coarse transmission contains halo artifacts. So, we need to refine this coarse transmission map.

#### 4.3.3.3 Refining the transmission map using Median Dark Channel Prior method:

The dark channel prior is a state-of-the-art image restoration technique to remove haze from a single image [30]. This method gives comparatively better haze free images, however it overlaps occlusion edges which result in halo effects in the dehazed image. MDCP [54] has the ability to preserve edges with minimizing the artifacts present in the images and videos. This filtering operation reduces the processing time and also preserve edges which is useful for image and video processing. This method can be expressed as:

$$J^{dark}(x,y) = \underset{(i,j)\varepsilon\Omega(x,y)}{med} ( \min_{c\varepsilon\{r,g,b\}} (J^c(i,j))) \tag{4.7}$$

The MDCP method has been used for refining the transmission map. This reduces the overlaps of edges and artifacts. Hence fog free image has been achieved. The MDCP on the

estimated transmission map is given by,

$$t(x,y) = 1 - w \underset{(i,j)\varepsilon\Omega(x,y)}{med}(\min_{c\varepsilon\{r,g,b\}}(\frac{I^c(i,j)}{A^c})) \tag{4.8}$$

#### 4.3.3.4 Estimating the Scene radiance

In order to restore the contrast of the foggy and hazy images estimation of scene radiance is necessary. Therefore scene radiance is an important factor, which is estimated on the basis of airlight and transmission map. The scene radiance is obtained by equation (4.3):

$$J(x,y) = \frac{I(x,y) - A^c}{max(T(x,y), t_o)} + A^c \tag{4.9}$$

According to He et al. [30] the direct attenuation term $J(x,y)\ T(x,y)$ can be very close to zero when the transmission map $T(x,y)$ is close to zero. Since the recovered scene radiance $J(x,y)$ is prone to noise, the transmission $T(x,y)$ is restricted to a lower bound $t_o$ (typically 0.1) so that some amount of fog is preserved.

## 4.4 Experimental Results

In this section, the results obtained after the simulation of the proposed algorithm are analyzed and compared with the previous methods to remove the blur edges. The results are compared based on the below performance metrics.

### 4.4.1 Performance Metrics

Aim of the dehazing algorithms is to increase the contrast while preserving the details in the image/video. Processing time is an important performance metric while considering a real time application. Therefore, performance metrics like processing time, $e$ and $r$ values are used for showing the effectiveness of our method. Processing time is the time taken to process a particular algorithm. The time taken to process depends on the processor, the simulator and time complexity of the algorithm itself. Next, we used Hautiere method ($e$ and $r$) to assess the performance of the algorithms on each of the test images.

### 4.4.2 Comparisons with Previous Methods

The accomplishment of the proposed approach is estimated both qualitatively and quantitatively on various foggy and hazy videos. This estimation is also valid for hazy and foggy images without loss of generality, since video is only a sequence of images. We compare our approach with He et al. [30] and bilateral filter [59] method using various videos. To evaluate the accuracy of the proposed method, we have chosen two sets of videos frames i.e hazy and foggy. The proposed method is simulated in MATLAB R2013a (8.1.0.430) 64-bit with 2.60GHz Intel(R) Core(TM) i5-3230 CPU @ along with 4GB RAM.

Fig. 4.2 (a) and 4.3 (a) are the original hazy and foggy video frame. Figs. 4.2 (b) and 4.3 (b) show the output video frame using He et al. method. But, this method produces dark frames with noticeable color distortion and contain artifacts. In the bilateral filter method, the contrast of the video is low and the edges are also not visible in Figs. 4.2 (c) and 4.3 (c). In Fig. 4.2 (d) and 4.3 (d), we observe that the proposed approach removes the haze in the input video frame and recovers the fine details of the building clearly. Our method is capable of removing

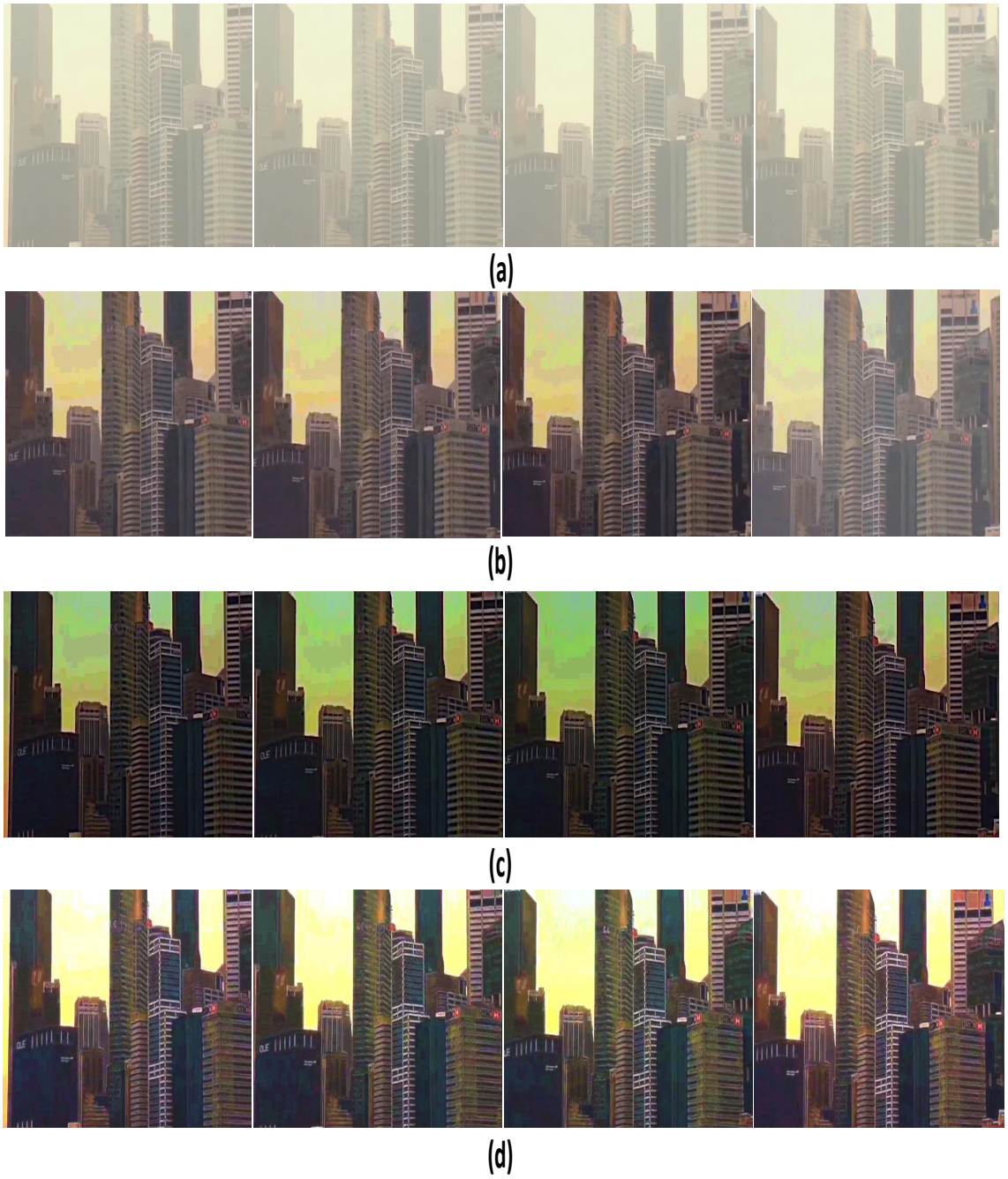


FIGURE 4.2: (a) Original hazy video sequence. (b) Dehazy video frame using He et al. method, (c) Dehazy video frame using Bilateral filter method, (d) Dehazy video frame using the proposed method. The frame numbers from left to right columns are 905, 910, 915 and 920, respectively.


FIGURE 4.3: (a) Original hazy video sequence. (b) Dehazy video frame using He et al. method, (c) Dehazy video frame using Bilateral filter method, (d) Dehazy video frame using the proposed method. The frame numbers from left to right columns are 610, 620, 630 and 660, respectively.

the halo artifacts near the scene depth discontinuities in hazy and mild fog conditions. However, for dense fog conditions few artifacts remain.

Tables 4.1 and 4.2 show the quantitative measurement results for Figs. 4.2 and 4.3 respectively. From Table 4.1, using He et al. method it is found that $e$ values are high for frame

TABLE 4.1: **Quantitative measurement result (Fig. 4.2)**

| Frame Number | He et al. | | Bilateral filter Method | | Proposed Method | |
|---|---|---|---|---|---|---|
| | e | r | e | r | e | r |
| **905** | 0.3311 | 1.4414 | -0.0254 | 2.8528 | 0.2401 | 3.3636 |
| **910** | 0.2730 | 1.5086 | -0.0390 | 2.7063 | 0.2451 | 3.3798 |
| **915** | 0.3492 | 1.5083 | -0.1270 | 2.9086 | 0.2857 | 3.4765 |
| **920** | -0.9974 | 1.3338 | -0.0488 | 2.8356 | 0.2391 | 3.6204 |

TABLE 4.2: **Quantitative measurement result (Fig. 4.3)**

| Frame Number | He et al. | | Bilateral filter Method | | Proposed Method | |
|---|---|---|---|---|---|---|
| | e | r | e | r | e | r |
| **610** | -0.0573 | 1.064 | 0.1227 | 1.8406 | 0.3456 | 2.9818 |
| **620** | 0.4304 | 0.9176 | 0.1196 | 1.7146 | 0.4000 | 2.7905 |
| **630** | 0.4905 | 0.7783 | 0.1263 | 1.7785 | 0.4821 | 2.8768 |
| **660** | 0.4066 | 0.9216 | 0.0541 | 1.5602 | 0.3665 | 2.4986 |

numbers 905, 910 and 915, but it shows negative results for frame number 920. Here, $r$ values are fewer for all the frames. By using the bilateral filter method, $e$ values are negative for all the frames even though $r$ values are more. From Table 4.2, $e$ value is negative for frame number 610 and $r$ is less for He et al. method. These values are also less for the bilateral filter method. But, in the proposed method $e$ and $r$ is comparatively high. From Tables 4.1 and 4.2, we can conclude that our approach is better in terms of $e$ and $r$.

Another very important parameter is computational complexity. This is the execution time taken by algorithms to remove fog and haze from the video. Lower computational complexity indicates faster algorithm. This is a good indicator when we consider real-time fog and haze removal applications. We compare our result with He et al. method and bilateral filter method in terms of computational complexity.

In the case of He et al. algorithm, the dark channel can be computed in $O(MN)$ time, but the problem with this method is its soft matting method. The time taken by bilateral filter is

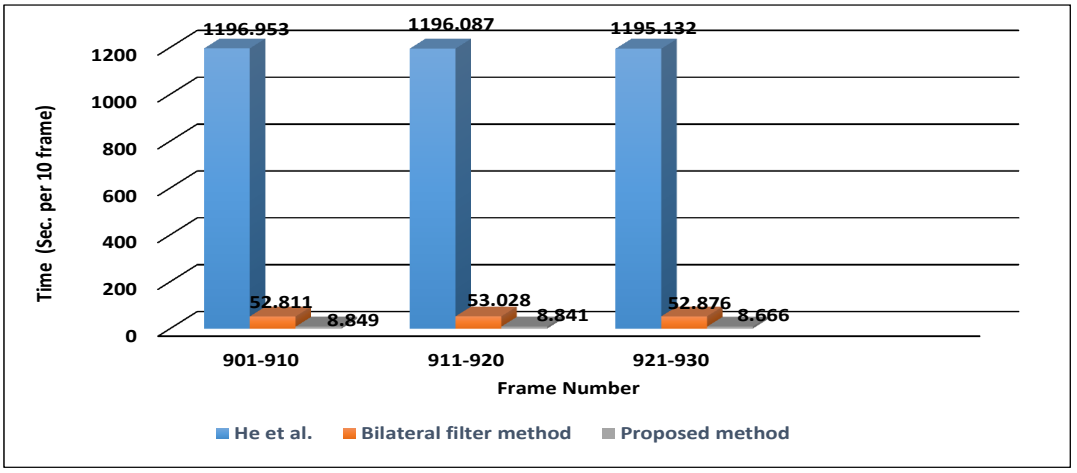


FIGURE 4.4: Computational complexity comparison (Fig. 4.2)

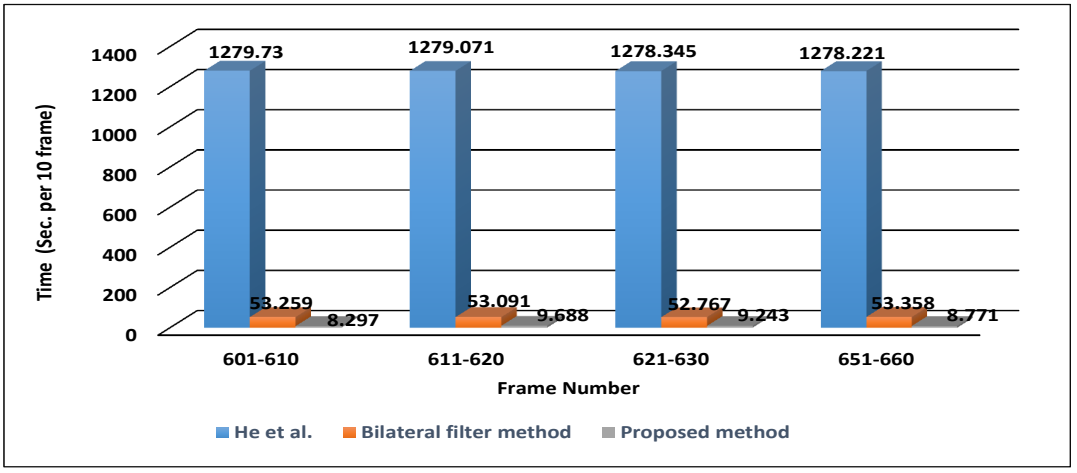


FIGURE 4.5: Computational complexity comparison (Fig. 4.3)

$O(MN^2)$. In the proposed method, the computation complexity is $O(MN)$ time. Figs. 4.4 and 4.5 show the computational complexity comparison with He et al. method, bilateral filter and proposed method. It is apparent that He et al. method and bilateral filter method are much more time consuming than our method. The proposed approach takes less than one second per video frame while the He et al., Bilateral filter method take 2 min and approximetly 5 second, respectively. Hence, the proposed method is able to produce precise results while maintaining the color and contrast of the video frame with least computational time.

## 4.5 Conclusion

In this chapter, we have presented restoration based approach for recovering the fog and haze free images and videos. The approach is developed for effectively balancing the contrast improvement and processing time. The performance of these approaches is compared with He et al. method and bilateral filter method. Experimental results show that the proposed approaches are able to achieve high efficiency and dehazing/defogging effect as well. However, in this image and video restoration based approach some artifacts are present which affects the edges of the images and videos. In the next chapter, optimized method for hardware realization of real time image and video deweathering is discussed. Optimization is required to remove the artifacts while retaining the benefits of the above methods.

# Chapter 5

# Fast and Efficient Visibility Restoration for Weather Degraded Image and Video

Many outdoor computer vision applications demand visibility restorations techniques for information recovery of weather degraded images. Estimation of transmission depth is an essential task of visibility restoration techniques. But, traditional state-of-the-art restoration techniques often suffer from either the generation of halo artifacts or reduce the contrast of the observed object in the restored images due to unequal distribution of transmission depth. For accurately and effectively estimating the transmission depth from different objects in the scene is the most challenging aspect of these techniques. In response to this problem, this chapter proposes a novel visibility restoration approach that is based on gamma transformation and median filtering. To meet the requirement of real-time applications, a 9-stage pipelined hardware accelerator has been implemented with field programmble gate array (FPGA) and 75.39 MHz operating frequency was obtained which compares favorably with existing methods of state-of-the-art and has lower

computational complexity. By conducting layout optimization an operating frequency of 200 MHz with 10.4k gate count is achieved using UMC 65-nm technology.

## 5.1 Introduction

Nearly all outdoor machine vision applications require images to be of utmost quality for processing as degradation in the image features can limit the performance of the intended application. There are various reasons for degradation of outdoor scene images, but one of the prior reasons is foggy weather conditions. Fog is caused by the presence of water droplets, formed from condensation of water vapor in the atmosphere. Such a common and natural weather condition can obscure visibility to a great extent, thus limiting the performance of outdoor surveillance systems. Therefore, it is essential to remove the effect of fog from images to increase the efficiency of computer vision algorithms.

Many researchers have proposed various techniques to enhance the visibility of foggy and hazy images. He et al. [30] proposed a dark channel prior method. For improving the quality of transmission map, the soft matting method is used. But, the soft matting algorithm requires huge amount of data for calculating the exact transmission at discontinuous edge of the depth map. Therefore, it is not suitable for real time applications. In order to overcome this difficulty, Xie et al. [60], yeh et al. [61], Tripathi et al. [59], He et al. [41] and Tarel and Hautiere [32] have proposed improved algorithms using the multiscale retinex technique, pixel based dark channel prior, bilateral filtering method, guided image filtering and median filtering, respectively. Xu et al. [62] used fast bilateral filtering method for refining the transmission map. Fang et al. [63] estimate the transmission map using a graph-based segmentation method, and refined this map using the bilateral filter. Meng et al. [64] estimate the unknown transmission map by employing the boundary constraint for an efficient regularization. Tang et al. [65] presented a learning

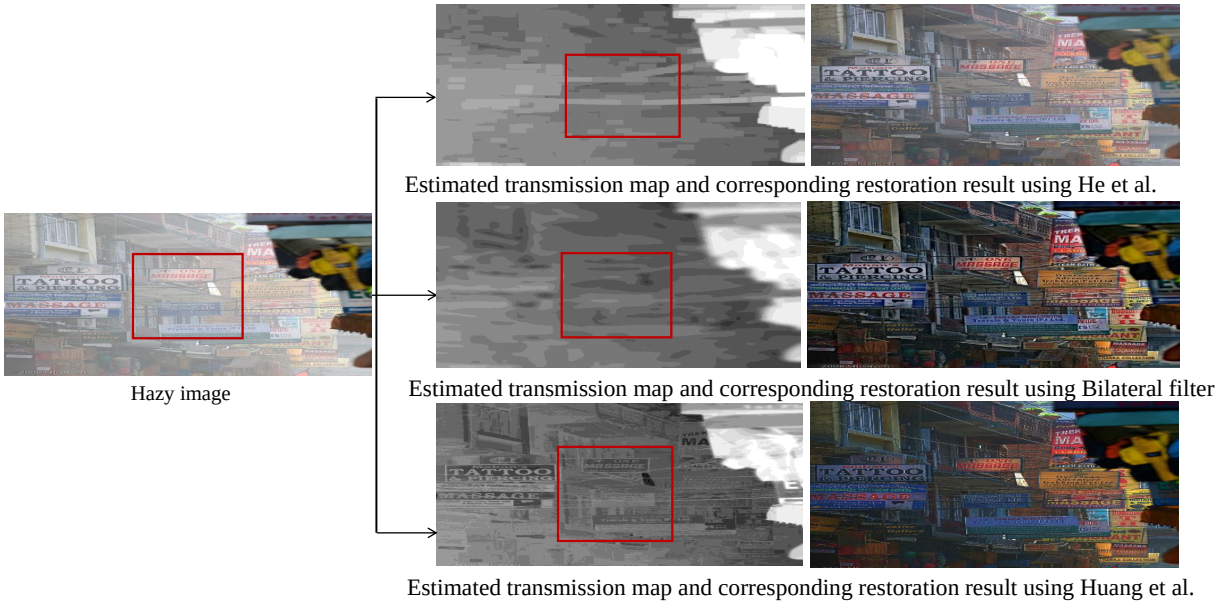


FIGURE 5.1: Estimated transmission map and corresponding restoration results of He et al., Bilateral filter, and Huang et al. method.

method for haze removal with Random Forest [66] to estimate the transmission. Ancuti et al. [67] proposed a fusion based method for dehazing based on single input image. Huang et al. [68] developed a visibility restoration technique for removing haze from a single image. Despite all these methods achieving remarkable results, they produce unwanted artifacts in the refined transmission map. Fig. 5.1 manifests that the inequitable transmission map using some of the well known algorithms ( He et al. method, Bilateral filter method and Huang et al. method) for dehazing the images. So, proper depth estimation is essential for accurate visibility restoration.

In the proposed work a novel fog removal algorithm which is less prone to artifacts and produces better perceptual quality with less complex computation is given. This work utilizes the concept of gamma transformation, median filter operation and the dark channel prior method. The main contribution of this work is the unification of gamma transformation and median filtering for intensifying the quality of the images and reduce the computational complexity. Gamma correction is a process to achieve the correct reproduction of relative luminance by compensating for the non-linearity in luminance. In various simple cases gamma correction can

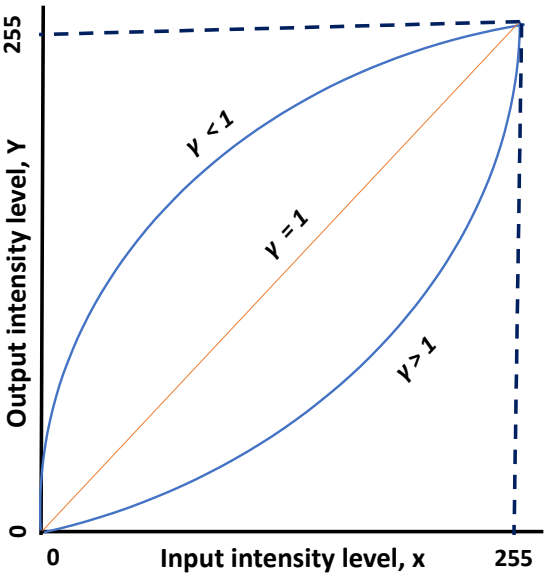


FIGURE 5.2: Gamma correction curve

be defined using the following power-law expression :

$$Y = c(x)^{\gamma} \tag{5.1}$$

where, $c$ is a positive constant parameter and $\gamma$ is the exponent. The intensity $x$ at each pixel of the input image is transformed to $Y$, by equation (5.1). Fig. 5.2 presents the principle of gamma correction. There are various enhancements possible by varying different levels of $\gamma$. Gamma correction curves with fractional values of $\gamma$ map a narrow range of dark input values into a wider range of output values, with the opposite being true for higher values of input levels. In order to smoothen transmission map median filter has been used. The algorithm which has been proposed saves pre/post processing steps and saves time, but in order to get best results a proper calibration to set the parameter for gamma transformation is needed. A few halo artifacts are expected to be found in the results due to the undertaken assumptions.

The rest of this chapter is organized as follows. Section 5.2 describes a complete description of our proposed fog and haze removal method. Performance metrics are presented in section 5.3. Section 5.4 shows experimental results as well as comparisons with prior methods. Section

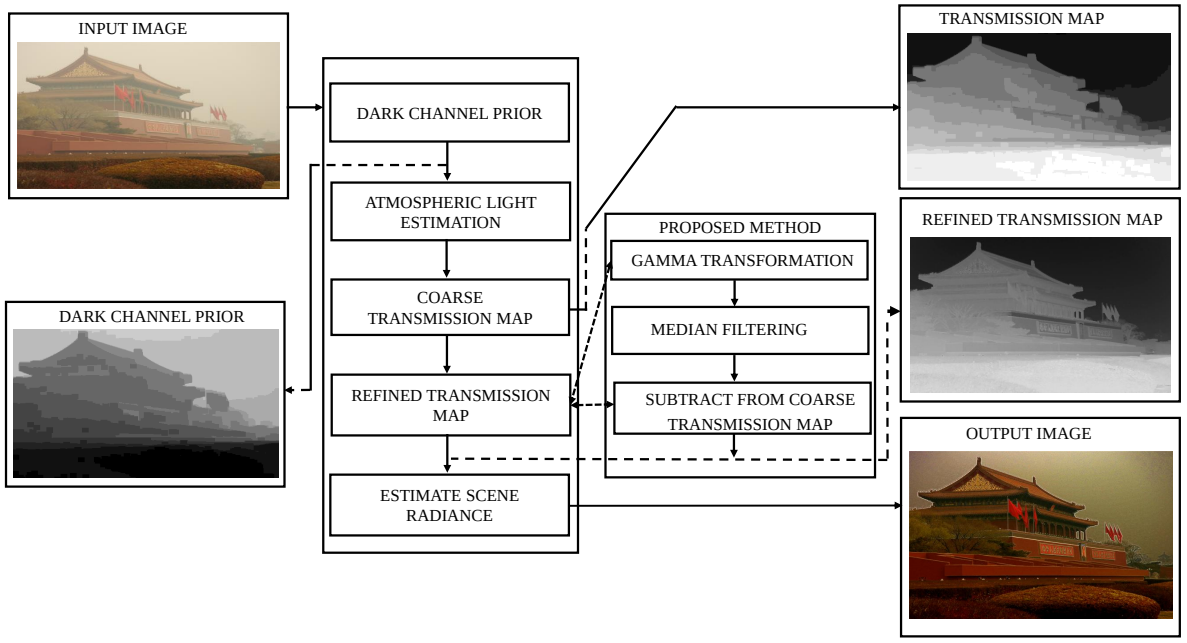


FIGURE 5.3: Flow chart of gamma transformation and median filtering for image deweathering.

5.5 describes the hardware implementation of our method in detail. Section 5.6 illustrates the comparison and simulation results for hardware implementation. Finally, the conclusion is presented in section 5.7.

## 5.2 The Proposed Algorithm

In this section, the proposed methodology for estimating the transmission map and hence resulting fog free image recovery is described. The main aim of the proposed method is to compensate the inequitable transmission map from which visibility of foggy images can be recovered with high efficacy. Fig. 5.3 shows the block diagram of the proposed defoggying algorithm. First, we estimate the atmospheric light using the dark channel prior method for the input foggy image. Then, the coarse transmission map is estimated using a dark channel prior method which provides appreciated results but contains halos effects. Hence refining of transmission map is imperative. The transmission map has been refined using gamma transformation and for

smoothening, median filtering is used. Finally, we restore the scene radiance by substituting the refined transmission map and the atmospheric light. The detail description of the proposed method is given in the following subsections.

### 5.2.1 Estimating the Atmospheric light

The primary stage of defogging is to estimate atmospheric light. In various single image methods the atmospheric light component is commonly estimated on the basis of fog-opaque pixel like pixel with maximum intensity value. On the contrary brightest pixel could be any other object other than the sky. Therefore, we have to improve the estimation of atmospheric light $A$ by selecting the top 0.1% brightest pixels in the dark channel method as shown in Fig. 5.3. Among these pixels, the pixels with highest intensity in the input image are selected as the atmospheric light in the atmospheric light estimation stage.

### 5.2.2 Estimating the Coarse transmission map

After calculating the airlight $A$, proper selection of transmission is predominant for the restoring the scene radiance. The dark channel prior provides a method to estimate transmission in a hazy image. The atmospheric light $A$ is a given constant value. At first, equation (4.3) is normalized by the atmospheric light $A$ as

$$\frac{I^c(x)}{A^c} = t(x)\frac{J^c(x)}{A^c} + 1 - t(x) \tag{5.2}$$

The normalization operation is independently applied to the three color channels. Then, the dark channel operation is calculated on the both sides of (5.2) as

$$\min_{y\varepsilon\Omega(x)}(\min_{c\varepsilon(r,g,b)}(\frac{I^c(y)}{A^c})) = \tilde{t}(x)\min_{y\varepsilon\Omega(x)}(\min_{c\varepsilon(r,g,b)}(\frac{J^c(x)}{A^c})) + 1 - \tilde{t}(x) \tag{5.3}$$

According to the dark channel prior, the minimum intensity in such a patch should have a very low value, even close to zero mainly due to shadows and dark objects. Since the scene radiance J is a haze-free image, the dark channel of J is close to zero. It is defined as follows:

$$J^{dark}(x) = \min_{y\varepsilon\Omega(x)}(\min_{c\varepsilon(r,g,b)}(J^c(y))) = 0 \tag{5.4}$$

Because $A^c$ is always positive, this leads to

$$J^{dark}(x) = \min_{y\varepsilon\Omega(x)}(\min_{c\varepsilon(r,g,b)}(\frac{J^c(y)}{A^c})) = 0 \tag{5.5}$$

Substituting equation (5.5) into (5.3), the estimated transmission map is

$$\tilde{t}(x) = 1 - \min_{y\varepsilon\Omega(x)}(\min_{c\varepsilon(r,g,b)}(\frac{I^c(y)}{A^c})) \tag{5.6}$$

Some haze is always present, even on a clear day. If we thoroughly remove the haze from the captured images, the image may appear somewhat unnatural. For this reason, He et al. [30] introduced a constant parameter $w$ to retain a portion of the haze for distant objects as

$$\tilde{t}(x) = 1 - w\min_{c}(\min_{(y)\varepsilon\Omega(x)}(\frac{I^c(y)}{A^c})) \tag{5.7}$$

where, $w$ is a weighting factor and its value is application based. For our work, $w$ is set to be 0.95. The transmission obtained by equation (5.7) is a coarse transmission map. We can observe in Fig. 5.4, the recovered image using the coarse transmission map contains halo artifacts. To remove these halo artifacts in the recovered image, He et al. [30] used soft matting to optimize the transmission map and reduce the tendency for generation of halo effects in the recovered

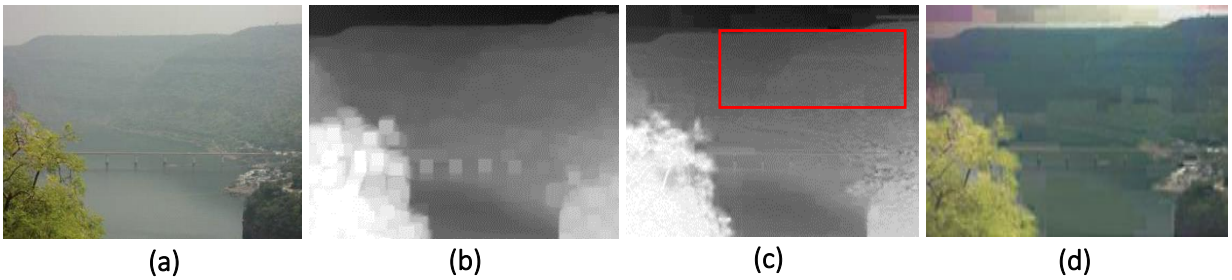


FIGURE 5.4: (a) Original image (b) Coarse transmission map without soft matting (c) refined transmission map with soft matting and (d) recovered image.

image. The matting Laplacian matrix is

$$\sum_{k|(i,j)\varepsilon w_k} \left( (\delta_{ij} - \frac{1}{|w_k|} \left( 1 + (I_i - \mu_k)^T \times (\Sigma_k + \frac{\epsilon}{w_k} U_3)^{-1} (I_i - \mu_k) \right) \right) \tag{5.8}$$

where $\delta_{ij}$ is the Kronecker delta, $\mu_k$ is the mean matrix of the colors in window $w_k$, $\Sigma_k$ is the covariance matrix of the colors in window $w_k$, $U_3$ is an identity matrix of size 3 x 3, $\epsilon$ is a regularizing parameter, and $|w_k|$ is the total number of pixels in window $w_k$.

The refined transmission map $t$ can be obtained by the following sparse linear system:

$$(L + \lambda U)t = \lambda \tilde{t} \tag{5.9}$$

where $L$ is the matting Laplacian matrix, $U$ is an identity matrix of the same size as $L$, and $\lambda$ is $10^{-4}$.

This method is not able to remove artifacts near the complex edge structures which can be seen in Fig. 5.4. Fig. 5.4 (a) shows the original hazy image. Fig. 5.4 (b) shows the coarse transmission map without soft matting. Fig. 5.4 (c) shows the refined transmission map with soft matting; Fig. 5.4 (d) shows the recovered image. From the above figures, it is noticeable that the coarse transmission map in Fig. 5.4 (b) has severe halo artifacts near the edges. The refined transmission map using the soft matting method eliminates the halo artifacts near the edges shown in Fig. 5.4 (c). However the image recovered by the refined transmission map still

contains halo artifacts near the edges, as shown in Fig. 5.4 (d).

Therefore, in order to improve the accuracy and eliminate the halo artifacts, we need to refine transmission map. So, we have proposed gamma transformation and median filter based transmission refinement. It will be discussed along with existing methods that can verify the estimation of refined transmission map. Generally, filtering in image processing and computer vision aims at improving the contrast of the image and suppressing the artifacts. Recently, for removing the artifacts and retaining the edge information of the transmission map many filtering approaches are presented such as bilateral filtering method and guided filtering method. To the best of our knowledge we are the first who consider and discuss about the trilateral filter based approach for refining the transmission map.

### 5.2.3 Refining the Transmission map

Tomasi and Manduchi proposed the bilateral filtering, which was an alternative of anisotropic diffusion. Bilateral filtering is a combination of domain as well as range filtering which preserves the edges while averaging the homogeneous intensity regions. It is calculated by,

$$BF[I]_p = \frac{1}{W_p} \sum_{q \epsilon \rho} g_{\sigma_d}(\|q - p\|)\ g_{\sigma_r}(f(q) - f(p))\ (f(q)) \tag{5.10}$$

where,

$$W_p = \sum_{q \epsilon \rho} g_{\sigma_d}(\|q - p\|)\ g_{\sigma_r}(f(q) - f(p)) \tag{5.11}$$

where, $\sigma_d$ and $\sigma_r$ denote the standard deviation for the domain and range kernel, $W_p$ is the the normalization factor, $g_{\sigma_d}$ values decreases with increase in pixel distance and $g_{\sigma_r}$ decreases with the influence of intensity difference i.e. $(f(q) - f(p))$ between pixels $p$ and $q$. The refined transmission map using bilateral filter is:

$$T_b = BF[I]_p\ \tilde{T} \tag{5.12}$$

As shown by the zoom-in regions in Fig. 5.5 (c), the refined transmission map and recovered deweathering images by bilateral filtering method have the edge blurring effects such as gradient reversal artifacts across the edge in the leaf. To overcome this, a trilateral filter [69] was introduced as a means to reduce gradient reversal artifacts. This is an extension of the bilateral filter. The trilateral filter is a gradient-preserving filter. This filter requires the specification of one parameter $\sigma_r$. The bilateral filter can be written as derivatives of $f$ (i.e., the gradients):

$$g_f(x) = \frac{1}{k_\nabla(x)} \int_\Omega \nabla f(x+a) \; . \; w_1(a) \; . w_2 \; (\parallel \nabla f(x+a) - \nabla f(x) \parallel) \; da \tag{5.13}$$

$$k_\nabla(x) = \int_\Omega w_1(a) \; . \; w_2 \; (\parallel \nabla f(x+a) - \nabla f(x) \parallel) \; da \tag{5.14}$$

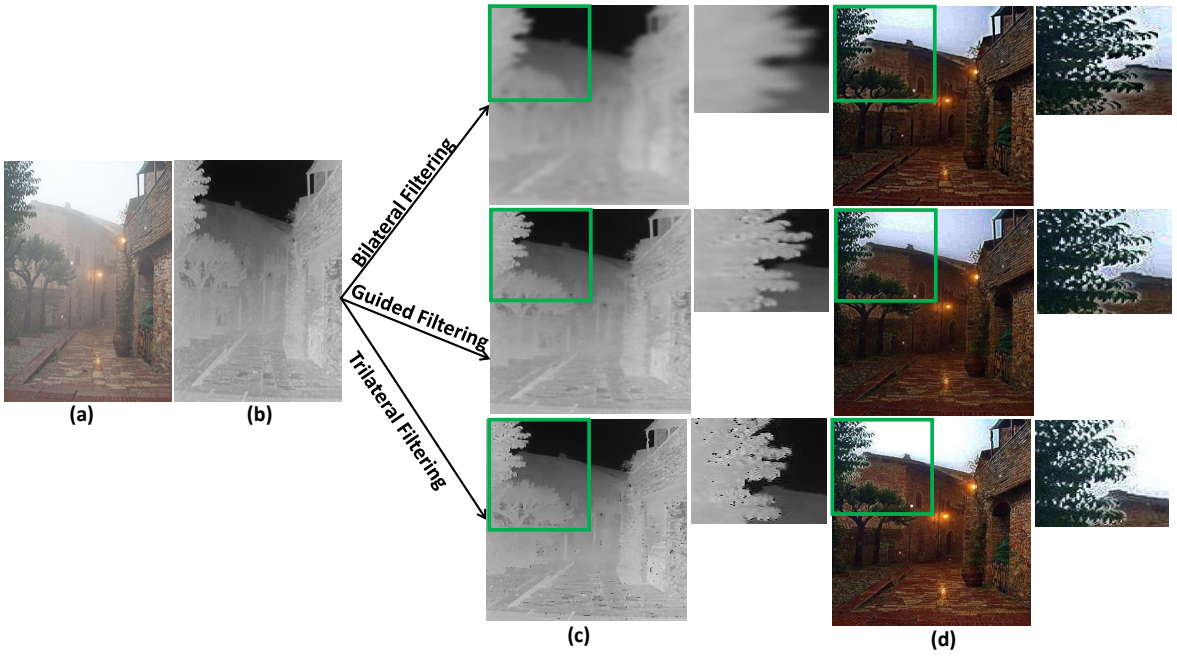


FIGURE 5.5: (a) Original image (b) Coarse transmission map; from top to bottom, (c) refined transmission map using Bilateral filtering, Guided filtering and Trilateral filtering methods (d) recovered image using Bilateral filtering, Guided filtering and Trilateral filtering methods.

For the subsequent second bilateral filter, Choudhury et al. suggested the use of the smoothed gradient $g_f(x)$ instead of $\nabla f(x)$ for estimating an approximate plane,

$$p_f(x,a) = f(x) + g_f(x)\ .a \tag{5.15}$$

Let $f_\triangle(x,a) = f(x+a)$ - $p_f(x,a)$. Furthermore, a neighbourhood function

$$M(x,a) = \begin{cases} a & if\ |g_f(x+a) - g_f(x)| < c \\ 0 & otherwise \end{cases} \tag{5.16}$$

is used for the second weighting. Where, $c$ specifies the adaptive region. Finally,

$$t_T(x) = f(x) + \frac{1}{k_\triangle(x)} \int_\Omega f_\triangle(x,a)\ .\ w_1(a)\ . \\ w_2\ (f_\triangle(x,a)\ .\ M(x,a))\ da \tag{5.17}$$

$$k_\triangle(x) = \int_\Omega w_1(a)\ .\ w_2\ (f_\triangle(x,a))\ .\ M(x,a)\ da \tag{5.18}$$

$w_1$ and $w_2$ are assumed to be Gaussian functions, with standard deviations $\sigma_1$ and $\sigma_2$, respectively. The parameter for $w_2$ is defined as follows:

$$\sigma_2 = \beta\ .\ |\max_{x\epsilon\Omega} \bar{g}_f(x) - \min_{x\epsilon\Omega} \bar{g}_f(x)\ | \tag{5.19}$$

$\beta = 0.15$ is used. The refined transmission map using trilateral filter is:

$$T_T = t_T(x)\ \tilde{T} \tag{5.20}$$

The input foggy and hazy image and its corresponding refined transmission map and restored images are shown in Figs. 5.6 (a), (b) and (c), respectively. It is observed that the trilateral filter

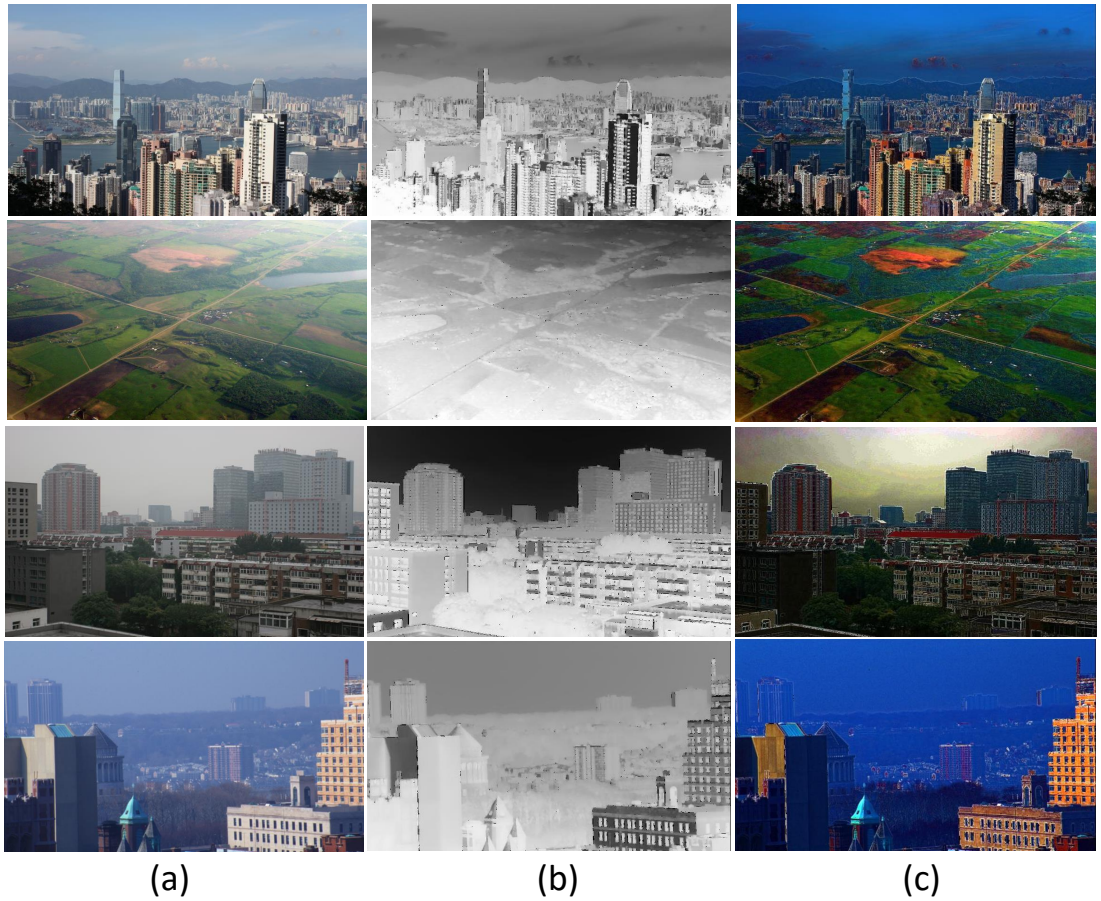


FIGURE 5.6: (a) Original image; from top to bottom,(b) refined transmission map and (c) restored image.

reduces irregular gradient artifacts along with preserving the edges. Unfortunately, this filter takes high computational cost. This issue will get worse when the size of the image increases, due to the fact that the processing time increases super quadratically with image size. The processing time of this algorithm is given in Table 5.1. As it is notable from Table 5.1 that trilateral filter takes a lot of processing time and hence looses its performance credibility, therefore it has not been considered for the obvious reason.

TABLE 5.1: **Algorithm processing results (Trilateral Filter)**

| **Image** | **Size** | **Time (second)** |
|---|---|---|
| **Hongkong** | 1036x692 | 12831.01 |
| **Aerial** | 622x442 | 1905.01 |
| **Bulding** | 600x400 | 1539.79 |
| **Schechner** | 768x434 | 3615.88 |

From literature we observe that to speed up the transmission map refinement, a guided filter is used. It is derived from a local linear model which generates the filtering output by considering the guidance image. The refined transmission map using guided filter is:

$$T_i = \sum_j W_{ij}(G)\ \tilde{T}_j \tag{5.21}$$

$$W_{ij}(G) = \frac{1}{|\omega|^2} \sum_{k:(i,j)\varepsilon\omega_k} \left(1 + \frac{(G_i - \mu_k)(G_j - \mu_k)}{\sigma_k^2 + \epsilon}\right) \tag{5.22}$$

where, $G$ is the guidance image, $\mu_k$ and $\sigma_k^2$ are the mean and variance of $G$ in $\omega_k$, $|\omega|$ is the number of pixels in $\omega_k$ and $\epsilon$ is a regularization parameter. This filter has the edge smoothing property, but still suffers from the gradient reversal artifacts shown in Fig. 5.5.

So, in order to balance between processing time and handling of hazy and foggy images, we have presented gamma transformation and median filter based transmission refinement. In order to achieve optimum haze and fog removal results, we apply gamma transformation method and median filtering for enhancing and smoothening the transmission map. Transmission map is a function of the distance of the scene from the camera. It should vary smoothly with different objects in the scene at different distances. The gamma transformation on the estimated transmission map is given by,

$$t(x) = c \cdot (\tilde{t}(x))^{\gamma} \tag{5.23}$$

where, $c$ is positive constant, $\tilde{t}(x)$ is the coarse transmission map. The refined transmission map is the output extracted by subtracting coarse transmission map from that obtained after smoothening by median filter. The output of the refined transmission map is shown in Fig. 5.3. This refined transmission map is finally used to estimate the scene radiance.

### 5.2.4 Estimating the Scene radiance

With the transmission map and airlight, the scene radiance can be restored by solving equation (4.3):

$$J^c(x) = \frac{I^c(x) - A^c}{max(t(x), t_o)} + A^c \tag{5.24}$$

As per He et al. [30] the direct attenuation term $J(x)t(x)$ can be very close to zero as transmission map $t(x)$ is close to zero. As the scene radiance $J(x)$ which has been recovered is directly prone to noise, the transmission $t(x)$ has to be restricted to lower bound of $t_o$ (typically 0.1) in order to preserve some amount of fog. Also, we include a brightness factor to the scene radiance to obtain the final fog-free image in scene radiance estimation stage as shown in Fig. 5.3.

## 5.3 Performance Metrics

In this section, some performance metrics like processing time, contrast gain and number of saturated pixels are used to compare our results with He et al. method [30], Bilateral filter method [59], Guided filter method [41] and Huang et al. method [68].

### 5.3.1 Processing time

Processing time is the time taken to process a specific algorithm. It depends on the simulator, the processor and computational complexity of the algorithm itself. This is an important performance metric while considering real-time applications.

### 5.3.2 Contrast gain

In order to differentiate a foggy and fog-free image a standard method can be used. A foggy image has lower contrast in comparison with fog-free image [70]. Therefore contrast gain can be a measuring or comparative parameter to quantitatively analyse fog removal algorithms. Contrast gain is parameterized as the mean contrast difference between de-foggy and foggy image. A good algorithm should have a positive contrast gain. Hence contrast gain is specified as,

$$C_{gain} = \bar{C}_{Idefog} - \bar{C}_{Ifog} \tag{5.25}$$

where, $C_{Idefog}$ and $C_{Ifog}$ are the mean contrast of the de-foggy a foggy images respectively.

For an image of size $M \times N$ denoted by $I(x, y)$, the mean contrast is given by,

$$\bar{C}_I = \frac{1}{MN} \sum_{y=0}^{N-1} \sum_{x=0}^{M-1} C(x, y) \tag{5.26}$$

where, $C(x, y) = \frac{S(x,y)}{m(x,y)}$

$$m(x, y) = \frac{1}{(2p+1)^2} \sum_{k=-p}^{p} \sum_{l=-p}^{p} I(x+k, y+l) \tag{5.27}$$

and

$$S(x, y) = \frac{1}{(2p+1)^2} \sum_{k=-p}^{p} \sum_{l=-p}^{p} |I(x+k, y+l) - m(x, y)| \tag{5.28}$$

In equs. (5.27) and (5.28), the quantity $\frac{1}{(2p+1)^2}$ is the size of a square window in pixels.

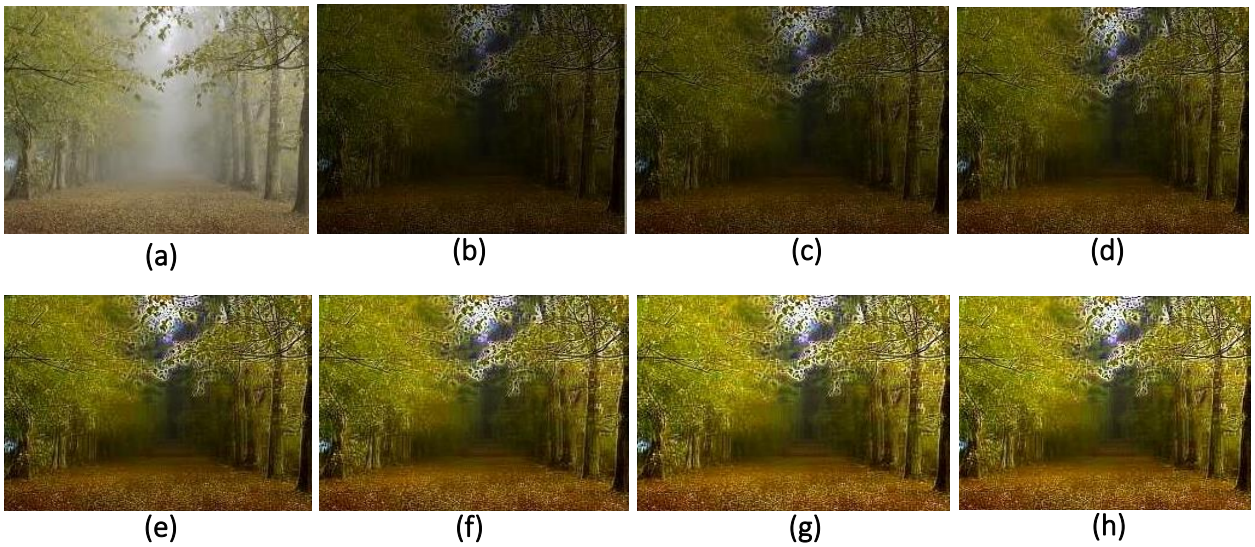


FIGURE 5.7: (a) input image and corresponding output results with different $\gamma$ values (b) $\gamma = 0.6$ (c) $\gamma = 0.8$ (d) $\gamma = 1$ (e) $\gamma = 1.3$ (f) $\gamma = 1.5$ (g) $\gamma = 1.7$ (h) $\gamma = 2$.

### 5.3.3 Percentage of saturated pixels

The pixels of the output image become saturated if the contrast gain is very high. Hence, along with the high contrast gain, it is also required to measure the number of saturated pixels. The percentage of the saturated pixels $\sigma$ is given by,

$$\sigma = \frac{m}{MN} \times 100 \tag{5.29}$$

where, $m$ is the number of saturated pixels. % of saturated pixels ($\sigma$) are low which indicates better performance of fog and haze removal algorithm.

## 5.4 Comparison and Experimental Results

This section provides a comparison of the proposed method with other methods, namely He et al. method [30], Bilateral filter method [59], Guided filter method [41] and Huang et al. method [68]. The simulations tool used for analyses is MATLAB R2012b (8.0.0.783) 64-bit and the algorithms were processed on Intel (R) Core (TM) i5-3337U CPU @ 1.80GHz along with 8Gb

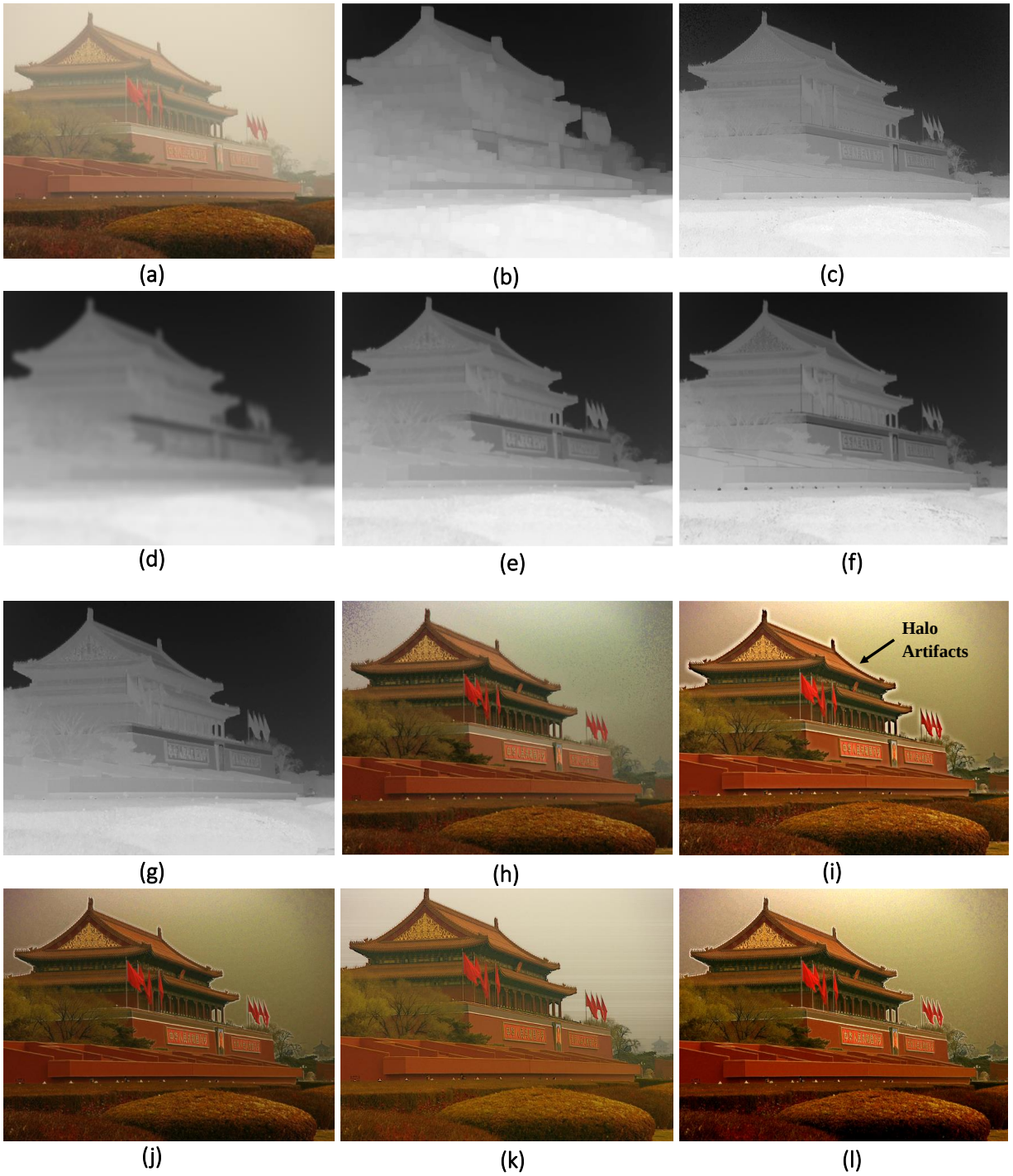


FIGURE 5.8: Tiananmen image. **(a)** Original image. **(b)** Transmission map of original image. **(c to g)** Refined transmission map using He et al. method, Bilateral filter method, Guided filter method, Huang et al. method and Proposed method respectively. **(h to l)** Defogged images using **(c to g).**

RAM. As already mentioned earlier, the constant parameters $c$ and $\gamma$ are application specific and the best values of these constants have to be determined using some optimal calibration method which is mentioned in Fig. 5.7. From this figure it can be observed that in proposed method different values of $\gamma$ has been applied and as the gamma values exceed 2 halo artifacts starts to appear prominently. The approach to make the proposed method independent of this kind of estimation we use possible enhancement techniques which increases brightness of images. The results are compared based on the above mentioned performance metrics.

### 5.4.1 Qualitative Comparison

In general, bad weather conditions affect the quality of the images. Therefore, we used several images taken in bad weather conditions to evaluate each method along with our proposed method. We have taken 9 sets of foggy and hazy images (Tiananmen, y01, y16, Pumpkin, Stadium, Swan, Cone, House and Mountain) as representations of weather degraded images for restoration experiments. The above mentioned nine sets of images used for the purpose of simulating the algorithms are shown in figures (Figs. 5.8 - 5.16). Fig. 5.8 shows the foggy image and restoration results from each method. Fig 5.8 (a) shows the original weather degraded images. Fig. 5.8 (b) shows the transmission map of original images. Fig. 5.8 (c) shows the refined transmission map using He et al. method and corresponding fog free images in Fig. 5.8 (h). However, a small amount of fog and halo artifacts are still present due to insufficient transmission map produced. This halo artifact is suppressed by using the bilateral filter method. Figs. 5.8 (d) and 5.8 (i) show the transmission map refinement and recovered image using bilateral filter method. Unfortunately, this method produces gradient reversal artifacts near edges. The guided filter method slightly eliminates this problem. Fig. 5.8 (e) shows the refined transmission map using the guided filter method. The recovered image is shown in Fig. 5.8 (j). This method is an approximate solution of the soft matting method which may lead to image blur. Huang et al.

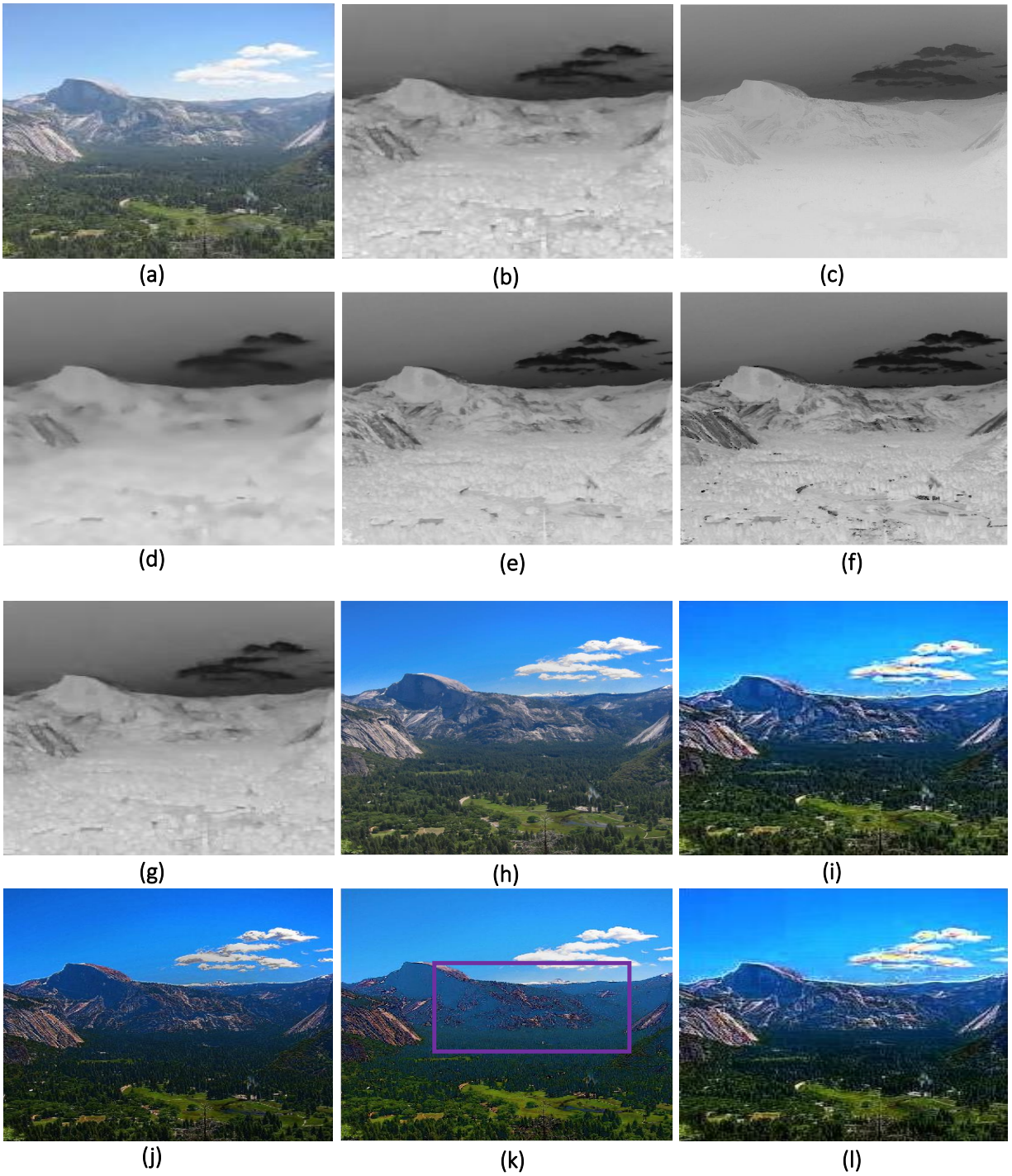


FIGURE 5.9: y01 image. **(a)** Original image. **(b)** Transmission map of original image. **(c to g)** Refined transmission map using He et al. method, Bilateral filter method, Guided filter method, Huang et al. method and Proposed method, respectively. **(h to l)** Defogged images using **(c to g).**

uses a visibility restoration technique to avoid halo effects and color distortion in different scenes captured during bad weather conditions. Figs. 5.8 (f) and 5.8 (k) show the refined transmission map and fog free images. But the contrast of the fog free image, shown in Fig. 5.8 (k), was not adequately improved. The proposed method preserve the edges and significantly improved the contrast of the image. Figs. 5.8 (g) and 5.8 (l) show the refined transmission map and recovered images.

Figs. 5.9 and 5.10 show the hazy image and restoration results from each method. The original weather degraded images shown in Figs. 5.9 (a) and 5.10 (a). Figs. 5.9 (b) and 5.10 (b) show the transmission map of original images. Fig. 5.9 (c) and Fig. 5.10 (c) show the refined transmission map using He et al. method. This method gives good results and maintain the high quality haze free images as shown in Figs. 5.9 (h) and 5.10 (h). This method uses a soft matting technique to refine the transmission map. It cannot efficiently optimize the transmission near complex regions. For optimization, bilateral filter method is used. Figs. 5.9 (d) and 5.10 (d) show the refined transmission map and corresponding deweathering images are shown in Figs. 5.9 (i) and 5.10 (i). This method needs to calculate a weighted average of neighboring pixels for preserving the edges of processed images. The guided filter method has better behavior near the edges which we can see in Figs. 5.9 (e) and 5.10 (e). The recovered enhanced images are shown in Figs. 5.9 (j) and 5.10 (j). However, as Figs. 5.9 (j) and 5.10 (j) show, a good quality image, but halo artificats were still generated. Figs. 5.9 (f) and 5.10 (f) show the refined transmission map using Huang et al. method. This method even though preserving the edges of the image, but cannot efficiently avoid the artifact generated in the recovered images as shown in Figs. 5.9 (k) and 5.10 (k). The above interpretation can be observed from Figs. 5.9 (k) and 5.10 (k), wherein there is color distortion in the mountain area. In contrast to the deficiencies of these methods, the proposed method is effectively preserving the edges of the images as shown in Figs. 5.9 (g) and 5.10 (g). Figs. 5.9 (l) and 5.10 (l) show the recovered images by using our method.

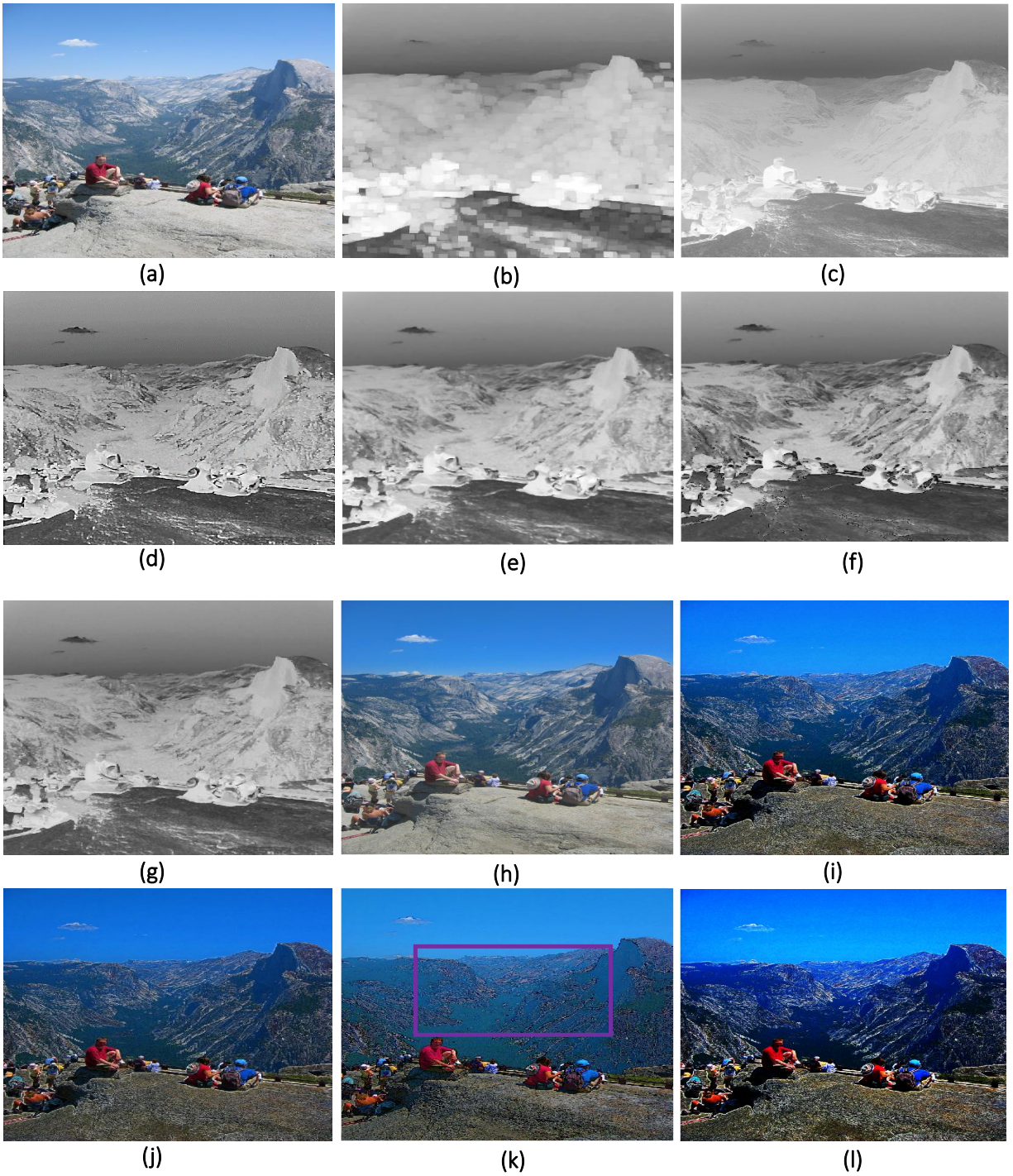


FIGURE 5.10: y16 image. **(a)** Original image. **(b)** Transmission map of original image. **(c to g)** Refined transmission map using He et al. method, Bilateral filter method, Guided filter method, Huang et al. method and Proposed method, respectively. **(h to l)** Defogged images using **(c to g).**

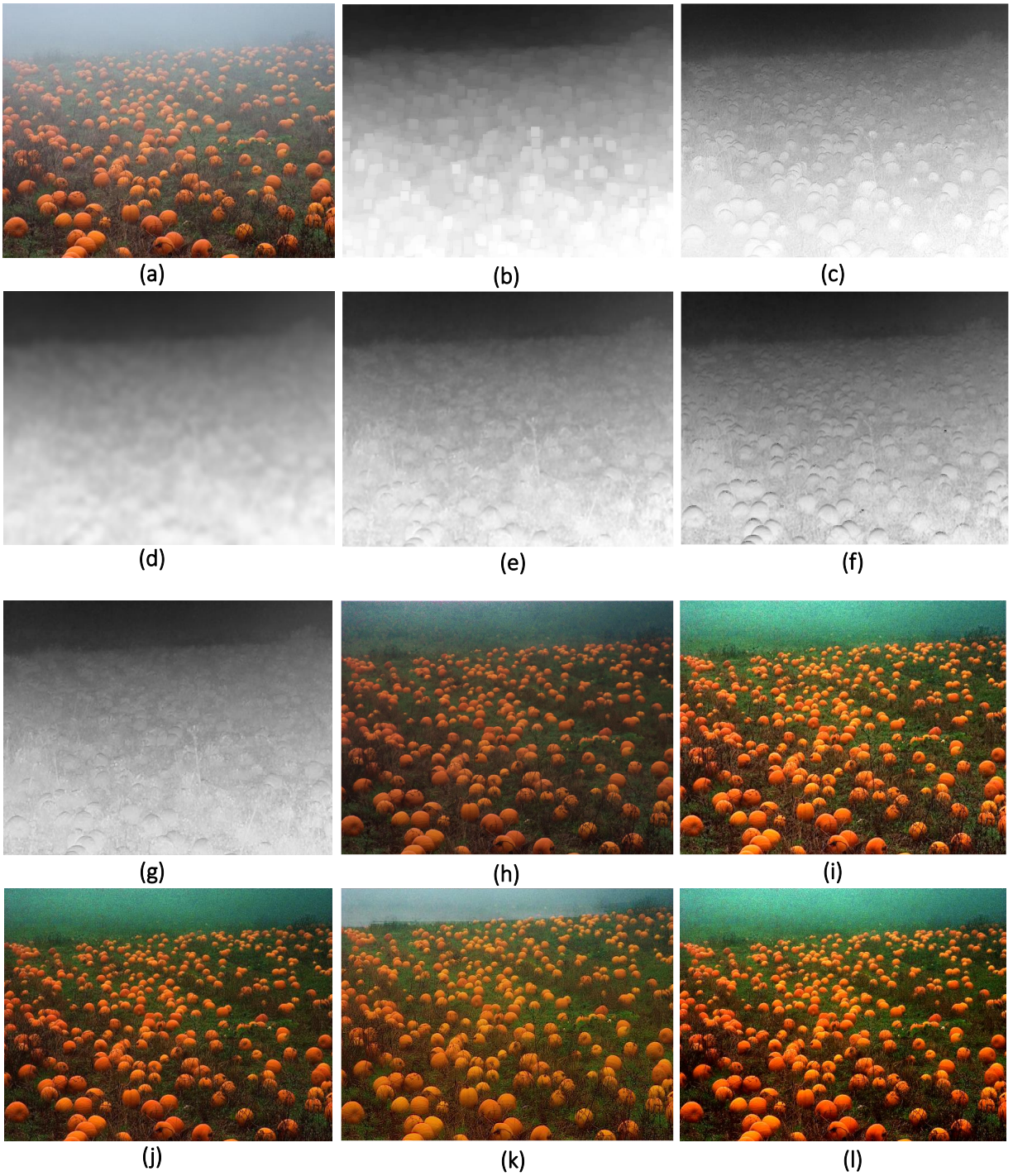


FIGURE 5.11: Pumpkin image. **(a)** Original image. **(b)** Transmission map of original image. **(c to g)** Refined transmission map using He et al. method, Bilateral filter method, Guided filter method, Huang et al. method and Proposed method, respectively. **(h to l)** Defogged images using **(c to g).**

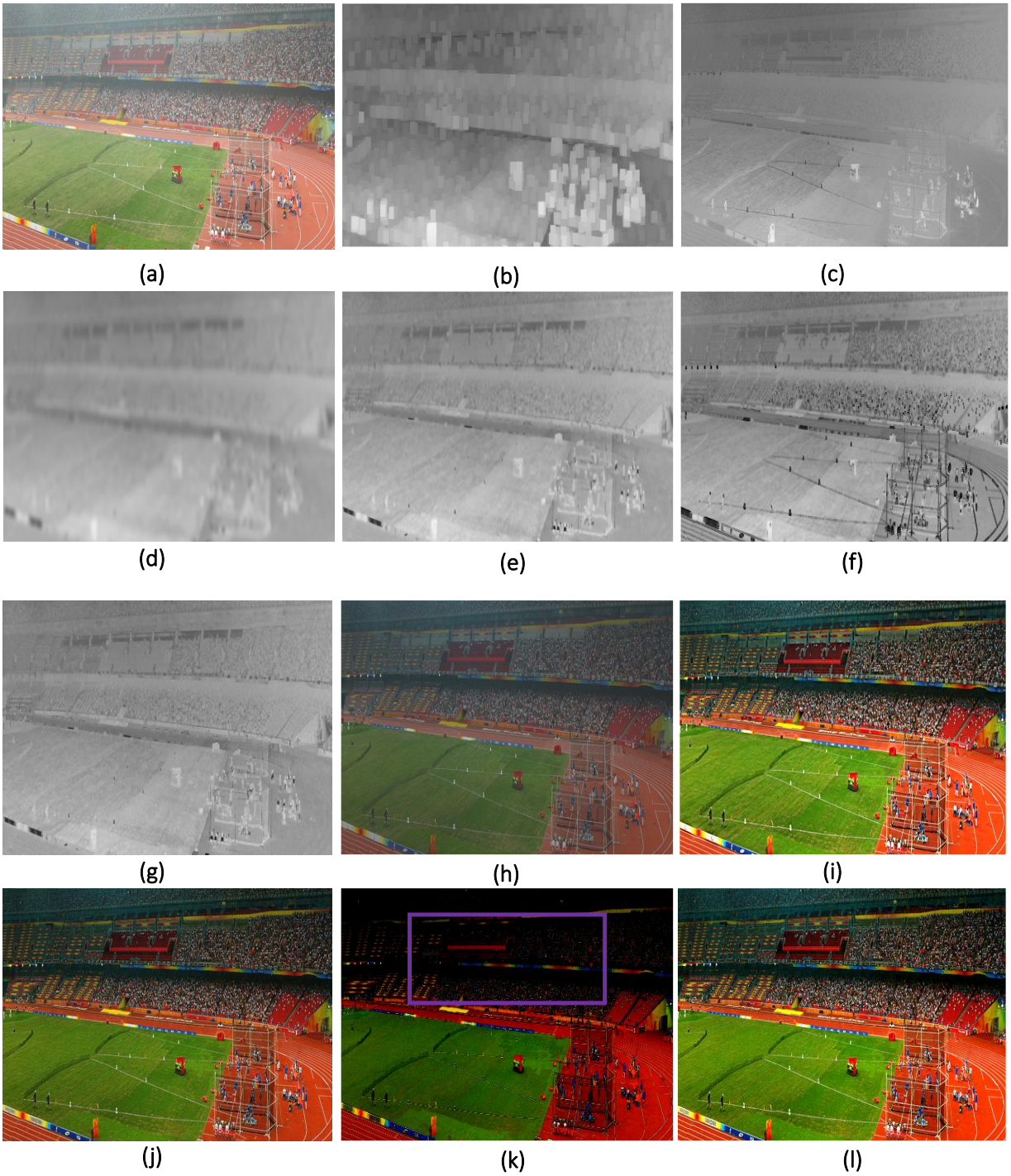


FIGURE 5.12: Stadium image. **(a)** Original image. **(b)** Transmission map of original image. **(c to g)** Refined transmission map using He et al. method, Bilateral filter method, Guided filter method, Huang et al. method and Proposed method, respectively. **(h to l)** Defogged images using **(c to g).**

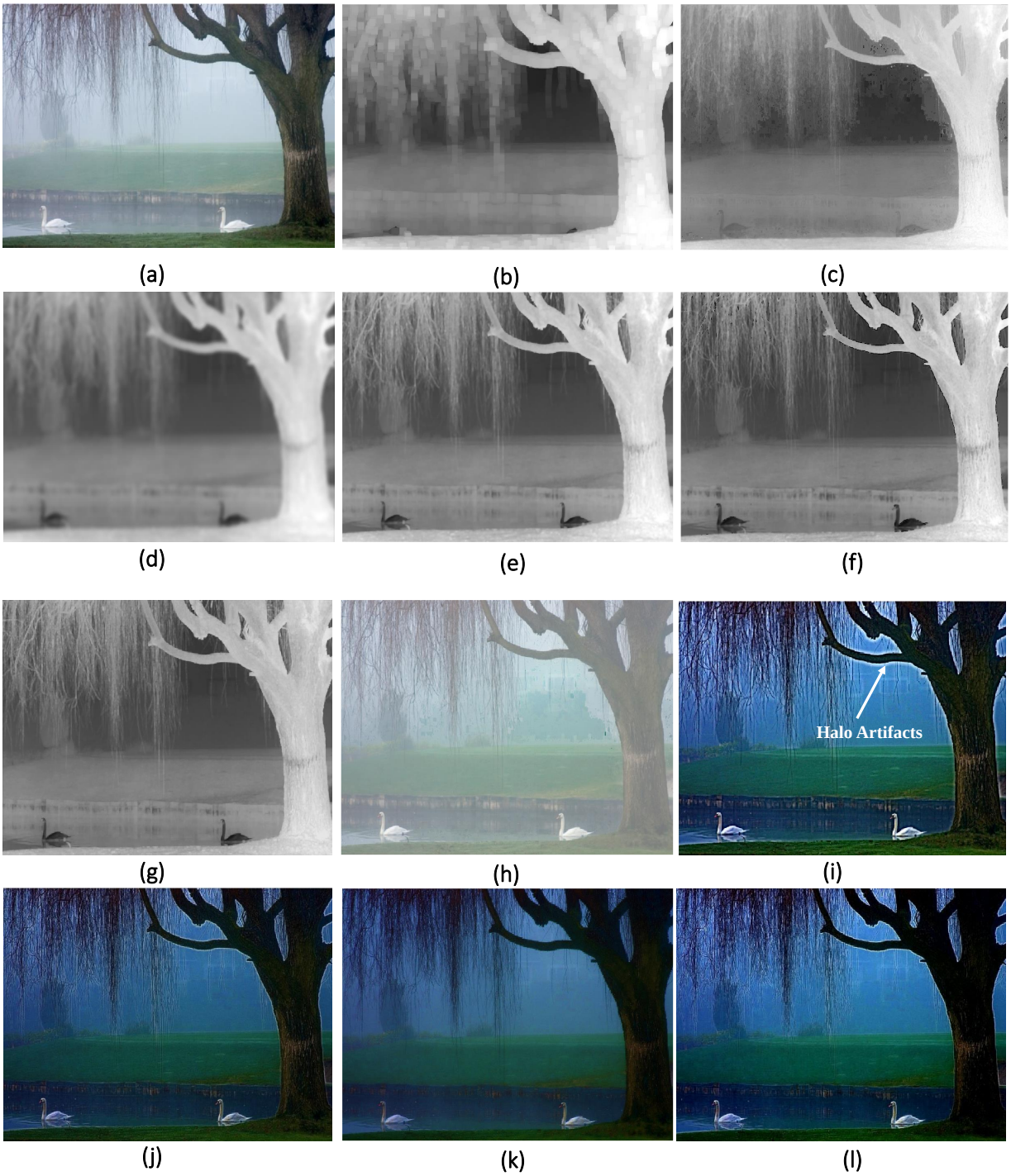


FIGURE 5.13: Swan image. **(a)** Original image. **(b)** Transmission map of original image. **(c to g)** Refined transmission map using He et al. method, Bilateral filter method, Guided filter method, Huang et al. method and Proposed method, respectively. **(h to l)** Defogged images using **(c to g).**

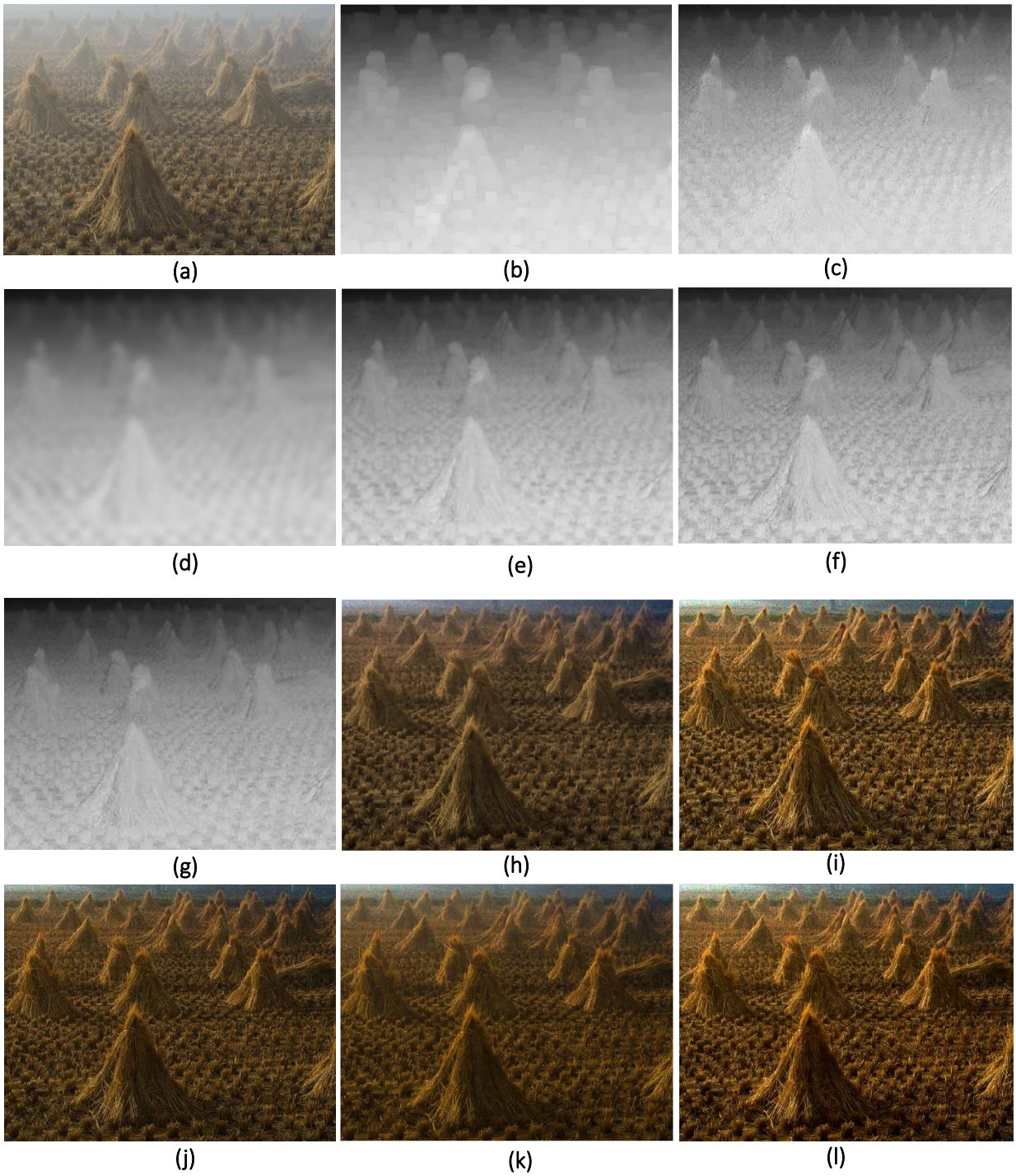


FIGURE 5.14: Cone image. **(a)** Original image. **(b)** Transmission map of original image. **(c to g)** Refined transmission map using He et al. method, Bilateral filter method, Guided filter method, Huang et al. method and Proposed method, respectively. **(h to l)** Defogged images using **(c to g).**

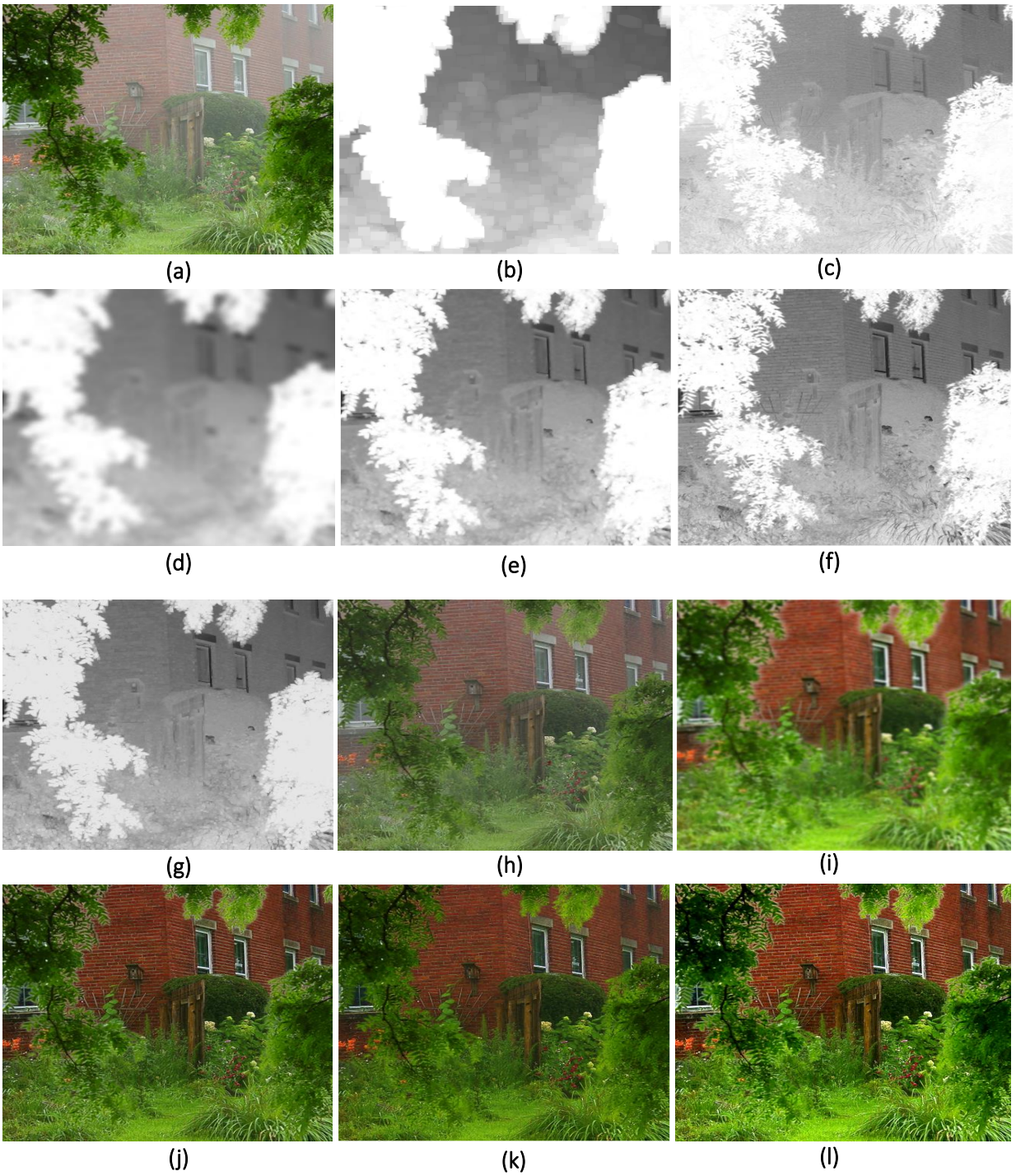


FIGURE 5.15: House image. **(a)** Original image. **(b)** Transmission map of original image. **(c to g)** Refined transmission map using He et al. method, Bilateral filter method, Guided filter method, Huang et al. method and Proposed method, respectively. **(h to l)** Defogged images using **(c to g).**

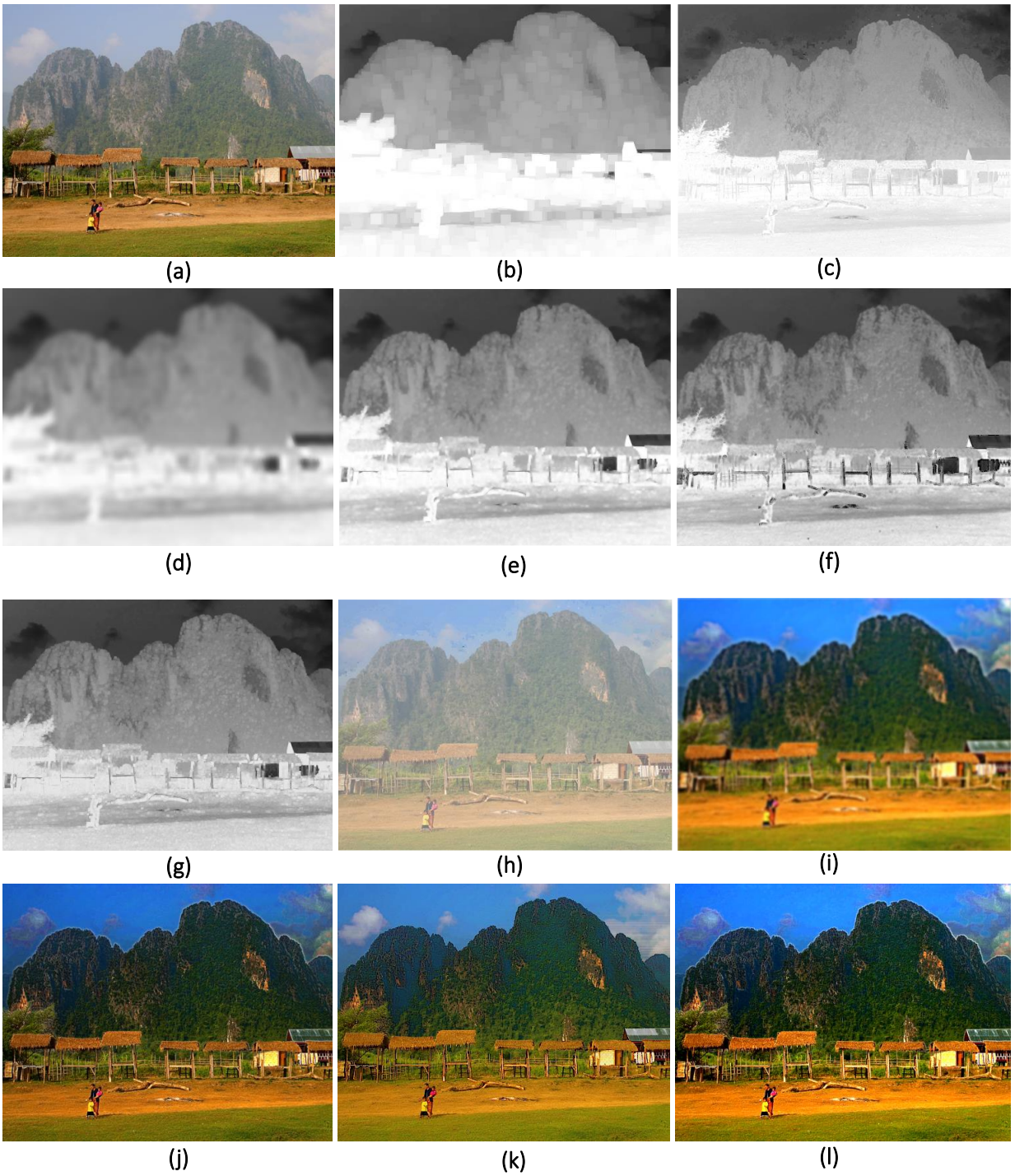


FIGURE 5.16: Mountain image. **(a)** Original image. **(b)** Transmission map of original image. **(c to g)** Refined transmission map using He et al. method, Bilateral filter method, Guided filter method, Huang et al. method and Proposed method, respectively. **(h to l)** Defogged images using **(c to g).**

Figs. 5.11 (a) and 5.12 (a), show the original images. Figs. 5.11 (b) and 5.12 (b) show the transmission map of original images. For these images, all methods generated acceptable refined transmission map except Huang et al. method. Figs. 5.11 (c)-(g) and Figs. 5.12 (c)-(g) show the refined transmission map and corresponding deweathering images are shown in Figs. 5.11 (h)-(l) and Figs. 5.12 (h)-(l). In Fig. 5.12 (k), it can be seen that the recovered image has more contrast. However, the percentage of saturated pixels are very high. Figs. 5.13 (a) and 5.14 (a) show the original foggy images, along with five refined transmission map and defoggy images by each method. He et al. method, bilateral filter, Guided filter method and Huang et al. method are not suitable for foggy images. Therefore, the restored images produced by these methods contain serious halo artifacts. Conversely, our method is giving better perceptual quality images.

Figs. 5.15 (a) and 5.16 (a) show the original hazy images. All methods are significantly preserving the edges and increasing the contrast of the images. It is noteworthy that the Huang et al. and proposed method enhanced the contrast of the images as well and preserving its complex edges, as shown in Figs. 5.15 (k)-(l) and Figs. 5.16 (k)-(l). It can be seen from the recovered images, our method works for dense haze and foggy images.

### 5.4.2 Quantitative Comparison

In this section, we have used performance metrics such as contrast gain and percentage of saturated pixels for evaluating the image quality. For the simulation of Figs. 5.8, 5.11, 5.12, 5.13, 5.14, 5.15 and 5.16 the value of $c = 0.1$ and $\gamma = 2$ whereas for Figs. 5.9 and 5.10 the value of $c = 0.1$ and $\gamma = 1.3$. Therefore it is an agreement of both parameters in order to obtain best results. The final image is not as bright as atmospheric light. So, in order to make it better a factor of 1.3 has been applied to all the results described in this chapter. In every illustrated results the window size has been taken as $3 \times 3$ for median filtering. Table 5.2 compares existing methods with our approach based on performance metrics. From the Table 5.2 it is clear that

TABLE 5.2: **Quantitative results and Computational complexity comparison**

| Indicator | Input and Image sizes | Method | Processing time (second) | Cgain | sigma |
|---|---|---|---|---|---|
| **Figure 5.6** | **Tiananmen (600x400)** | He et al. method (h) | 56.237 | 0.0180 | 0.000 |
| | | Bilateral filter method (i) | 5.166 | 0.0454 | 0.046 |
| | | Guided filter method (j) | 2.176 | 0.0392 | 0.039 |
| | | Huang et al. method (k) | 3.241 | 0.0439 | 0.000 |
| | | Proposed method (l) | 1.250 | 0.0816 | 0.032 |
| **Figure 5.7** | **y01 (576x768)** | He et al. method (h) | 97.081 | 0.0013 | 0.000 |
| | | Bilateral filter method (i) | 3.479 | 0.0452 | 0.002 |
| | | Guided filter method (j) | 3.174 | 0.0403 | 0.005 |
| | | Huang et al. method (k) | 4.643 | 0.0797 | 0.000 |
| | | Proposed method (l) | 1.225 | 0.0471 | 0.001 |
| **Figure 5.8** | **y16 (576x768)** | He et al. method (h) | 98.116 | 0.0679 | 0.000 |
| | | Bilateral filter method (i) | 3.470 | 0.0432 | 0.002 |
| | | Guided filter method (j) | 3.128 | 0.0468 | 0.047 |
| | | Huang et al. method (k) | 4.697 | 0.0897 | 0.012 |
| | | Proposed method (l) | 1.215 | 0.0481 | 0.001 |
| **Figure 5.9** | **Pumpkin (600x400)** | He et al. method (h) | 51.242 | -0.0110 | 0.000 |
| | | Bilateral filter method (i) | 9.315 | 0.0450 | 0.003 |
| | | Guided filter method (j) | 3.047 | 0.0412 | 0.001 |
| | | Huang et al. method (k) | 3.443 | 0.0751 | 0.001 |
| | | Proposed method (l) | 1.172 | 0.0765 | 0.012 |
| **Figure 5.10** | **Stadium (1000x327)** | He et al. method (h) | 70.366 | -0.0074 | 0.000 |
| | | Bilateral filter method (i) | 11.124 | 0.0912 | 0.484 |
| | | Guided filter method (j) | 3.551 | 0.0840 | 0.083 |
| | | Huang et al. method (k) | 13.346 | 0.5806 | **36.406** |
| | | Proposed method (l) | 2.404 | 0.1298 | 0.067 |
| **Figure 5.11** | **Swan input (835x557)** | He et al. method(h) | 106.064 | -0.0378 | 0.000 |
| | | Bilateral filter method (i) | 16.241 | 0.0748 | 1.075 |
| | | Guided filter method (j) | 5.516 | 0.0845 | 0.053 |
| | | Huang et al. method (k) | 7.032 | 0.0648 | 0.041 |
| | | Proposed method (l) | 3.491 | 0.2631 | 0.074 |
| **Figure 5.12** | **Cone (465x384)** | He et al. method (h) | 36.400 | 0.0090 | 0.000 |
| | | Bilateral filter method (i) | 6.336 | 0.0673 | 0.005 |
| | | Guided filter method (j) | 2.252 | 0.0572 | 0.003 |
| | | Huang et al. method (k) | 2.349 | 0.0929 | 0.001 |
| | | Proposed method (l) | 1.228 | 0.0944 | 0.142 |
| **Figure 5.13** | **House (441x450)** | He et al. method (h) | 44.064 | -0.0530 | 0.000 |
| | | Bilateral filter method (i) | 6.955 | 0.0177 | 0.259 |
| | | Guided filter method (j) | 2.351 | 0.0125 | 0.004 |
| | | Huang et al. method (k) | 2.302 | 0.0451 | 0.004 |
| | | Proposed method (l) | 1.628 | 0.0463 | 0.048 |
| **Figure 5.14** | **Mountain (512x384)** | He et al. method (h) | 41.367 | -0.0646 | 0.000 |
| | | Bilateral filter method (i) | 6.933 | 0.0382 | 0.284 |
| | | Guided filter method (j) | 2.428 | 0.0277 | 0.029 |
| | | Huang et al. method (k) | 2.337 | 0.0551 | 0.022 |
| | | Proposed method (l) | 1.426 | 0.0552 | 0.037 |

TABLE 5.3: **Quantitative measurement results based on the indicator e and r**

| Indicator | Input | Method | | | | | | | | | |
|---|---|---|---|---|---|---|---|---|---|---|---|
| | | He et al. method | | Bilateral filter method | | Guided filter method | | Huang et al. method | | Proposed method | |
| | | e | r | e | r | e | r | e | r | e | r |
| **Figure 5.6** | Tiananmen | -0.9983 | 1.1819 | -0.2796 | 2.4814 | -0.2586 | 1.8716 | -0.0480 | 1.365 | -0.1244 | 2.3240 |
| **Figure 5.7** | y01 | 0.0146 | 1.3740 | 0.0202 | 2.0143 | -0.0043 | 1.4764 | -0.0177 | 0.8812 | -0.0093 | 1.7455 |
| **Figure 5.8** | y16 | 0.0653 | 1.3338 | -0.1430 | 2.5303 | -0.2501 | 1.6329 | -0.1026 | 0.8469 | -0.1350 | 2.0392 |
| **Figure 5.9** | Pumpkin | 0.4483 | 1.3387 | 0.0287 | 2.0178 | -0.0067 | 1.4922 | -0.2543 | 1.2074 | -0.0053 | 1.9576 |
| **Figure 5.10** | Stadium | -0.0462 | 0.5515 | 0.2390 | 1.5051 | 0.2569 | 1.1768 | 0.2697 | 0.8654 | 0.2775 | 1.4607 |
| **Figure 5.11** | Swan input | -0.1730 | 0.6284 | -0.0680 | 2.3329 | -0.0512 | 1.4645 | -0.1575 | 0.8805 | 0.0173 | 1.6640 |
| **Figure 5.12** | Cone | -0.9987 | 0.8069 | 0.0068 | 2.1129 | -0.0584 | 1.5472 | -0.0149 | 1.1918 | -0.0530 | 2.0123 |
| **Figure 5.13** | House | -0.9988 | 0.5183 | 0.1151 | 1.7492 | 0.0918 | 1.3458 | 0.0159 | 0.9716 | 0.0734 | 1.7444 |
| **Figure 5.14** | Mountain | -0.9987 | 0.3848 | 0.0053 | 1.8068 | -0.0134 | 1.3344 | -0.1136 | 1.0483 | -0.0101 | 1.7144 |

TABLE 5.4: **% improvement in processing time and quantitative measurement results (Proposed method)**

| Indicator | Input | % improvement w.r.t He et al. method | | | | | % improvement w.r.t Bilateral filter method | | | | | % improvement w.r.t Guided filter method | | | | | % improvement w.r.t Huang et al. method | | | | |
|---|---|---|---|---|---|---|---|---|---|---|---|---|---|---|---|---|---|---|---|---|---|
| | | Processing time | Cgain | e | r | sigma | Processing time | Cgain | e | r | sigma | Processing time | Cgain | e | r | sigma | Processing time | Cgain | e | r | sigma |
| **Figure 5.6** | Tiananmen | 97.77 | 77.94 | 87.53 | 96.63 | -50 | 75.80 | 44.36 | -55.50 | -6.77 | 30.43 | 42.55 | 51.96 | -51.89 | 24.17 | 17.94 | 61.43 | 46.20 | 61.41 | 70.25 | -50 |
| **Figure 5.7** | y01 | 98.73 | 97.23 | -36.30 | 27.03 | -50 | 64.78 | 4.33 | -53.96 | -13.34 | 50 | 61.40 | 14.22 | 53.76 | 18.22 | 80 | 73.61 | -40.9 | -47.45 | 98.08 | -50 |
| **Figure 5.8** | y16 | 98.76 | -41.16 | -51.62 | 52.57 | -50 | 64.98 | 10.18 | -5.59 | -19.40 | 50 | 61.15 | 2.70 | -46.01 | 24.88 | 97.87 | 74.13 | -46.37 | 31.57 | 56.78 | 91.66 |
| **Figure 5.9** | Pumpkin | 97.71 | 85.62 | -83.58 | 46.23 | -50 | 87.4 | 41.17 | -81.53 | -2.98 | -75 | 61.53 | 46.14 | -20.89 | 31.18 | -40.74 | 65.95 | 1.83 | -46.98 | 62.13 | -91.66 |
| **Figure 5.10** | Stadium | 96.58 | 94.29 | 83.35 | 62.24 | -50 | 78.38 | 29.73 | 16.10 | -2.94 | 86.17 | 32.30 | 35.28 | 8.01 | 24.12 | 19.27 | 81.98 | -77.64 | 2.89 | 68.78 | 99.81 |
| **Figure 5.11** | Swan input | 96.70 | 53.35 | 90 | 62.23 | -50 | 78.50 | 71.56 | 74.55 | -28.67 | 93.11 | 36.71 | 67.88 | 66.21 | 13.62 | -39.62 | 50.35 | 75.37 | 89 | 88.98 | -44.59 |
| **Figure 5.12** | Cone | 96.62 | 90.46 | 94.69 | 99.66 | -50 | 80.61 | 28.70 | -87.16 | -4.76 | -27.4 | 45.47 | 39.40 | -9.24 | 30.06 | -46.33 | 47.72 | 1.61 | 71.88 | 68.84 | -99.29 |
| **Figure 5.13** | House | 96.30 | 68.20 | 92.65 | 70.28 | -50 | 76.59 | 61.77 | -36.29 | -0.27 | 81.46 | 30.75 | 73 | -20.04 | 29.61 | -40.74 | 29.05 | 2.66 | 78.33 | 79.53 | -40.74 |
| **Figure 5.14** | Mountain | 96.55 | 68.45 | 98.98 | 77.55 | -50 | 79.43 | 30.79 | -90.56 | -5.11 | 86.97 | 41.26 | 49.81 | 24.62 | 28.47 | -27.58 | 38.98 | 0.18 | 91.10 | 63.54 | -40.54 |

the proposed algorithm takes lesser time compared to other methods. Moreover, the contrast gain is comparable when using the proposed method and the percentage of saturated pixels is also comparatively less. Therefore, the advantage of the proposed method over the method of He et al., Bilateral filter, Guided filter and Huang et al. are verified through this quantitative comparison of restoration efficacy in images captured in different bad weather conditions. We can observe that the contrast gain of Huang et al. method is highest for the Figure 5.10, however the percentage of saturated pixels is also high. We have added more well-known quantitative metrics such as $e$ and $r$ to evaluate the restoration efficacy of each method [45] in Table 5.3.

Analyzing the results of Table 5.3, measured restoration results obtain via $e$ and $r$ are improved in this proposed method and Bilateral filter method. Therefore, the advantage of our method over the method of He et al., Bilateral filter, Guided filter and Huang et al. are justified through the quantitative comparison of restored images. Table 5.4 indicates the % improvement in processing time and quantitative measurement results. In this Table 5.4, the performance improvements of our proposed method w.r.t all other methods in terms of five parameters (processing time, contrast gain, sigma, e and r) are given. It is clear that even if we are getting some negative results for few parameters in some figures, the overall performance is better. To conclude, by a visual inspection our technique is shown to be less prone to halo artifacts. Compared with the He et al. method, Bilateral filter method, Guided filter method and Huang et al. method a significant reduction in processing time was achieved. From the experimental results, the processing time of proposed method takes very less time for processing image with different sizes that is suitable for real-time applications.

In Table 5.4, He's Cgain and e is higher only for Fig. 5.10 and percentage saturated pixels are lower for all the figures than proposed method. In Fig. 5.10 (h), we found that even sigma value is lower, contrast gain and e is higher using He et al. method, but, importantly, our effect is better in terms of the visibility of all the figures. In Table 5.4, bilateral filter method e and r are larger, the contrast gain is smaller and percentage of saturated pixels are higher than ours. There is no difference in the visibility. But this method produces gradient reversal artifacts near edges as shown in Fig. 5.8 (i). From the Table 5.4, only a few values of e are larger and sigma is lower for guided filter method than ours. But, most of the parameters of our method are better than the guided filter method which suggests that we produced the better image quality results. In Table 5.4, the contrast gain and e for Figs. 5.9, 5.10 and 5.12 of Huang et al. method is larger than ours and percentage saturated pixels are also less. This method produced the detailed information of the images, but the effect is not good in terms of visibility. In Fig.

5.10, contrast gain of Huang et al. method is highest, but the e, r and sigma value are lowest. Obviously, the restored image is seriously distorted by Huang et al. method. In figure number 5.10, this method has more Cgain. But, the sigma is very high and highlighted by red color in Table 5.2. The red highlighted values are not acceptable. The most number of saturated pixels making its quality bad. In contrast, our results have better visual quality and retain fine details of recovered images. The proposed method performs faster than the state-of-the-art techniques.

## 5.5 Hardware Implementation of Gamma transformation and Median filtering for Image Deweathering

As proof-of-concept of this method being suitable for real time image/video application, we have designed an FPGA based hardware architecture and tested with weather degraded images for contrast improvement along with power consumption, processing time, energy per megapixel (EPM) and throughput. The proposed hardware architecture for fog and haze removal from weather degraded images and videos is designed using VHSIC Hardware Description Language (VHDL). We implemented our design using Altera Stratix EP1S10F780C6 FPGA, since it offers adequate speed and resources for performance verification and evaluation purpose. These test results can be fairly compared with shiau et al. [44] method which is also based on Altera Stratix EP1S10F780C6 FPGA.

The design concept for the hardware implementation of the proposed work is divided into five units: Register Bank (RB), Dark channel prior, atmospheric light estimation, transmission map estimation, and scene recovery are shown in Fig. 5.17. The input data marked by $I^c$ are read line by line and arranged for further processing in the register bank. The second unit is the dark channel prior which gives the lowest intensity pixel value present in the RGB channel. Then, the atmospheric light and transmission map are estimated. Finally, the scene radiance is

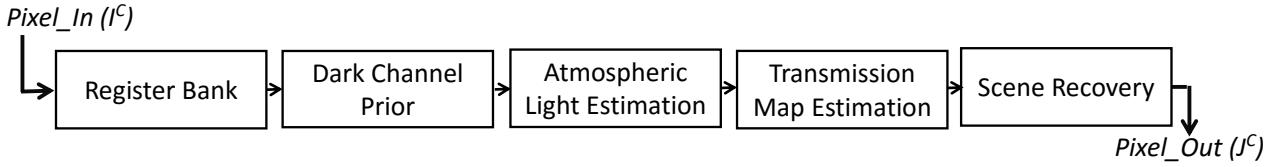


FIGURE 5.17: Order of the functional units of hardware architecture of Proposed method

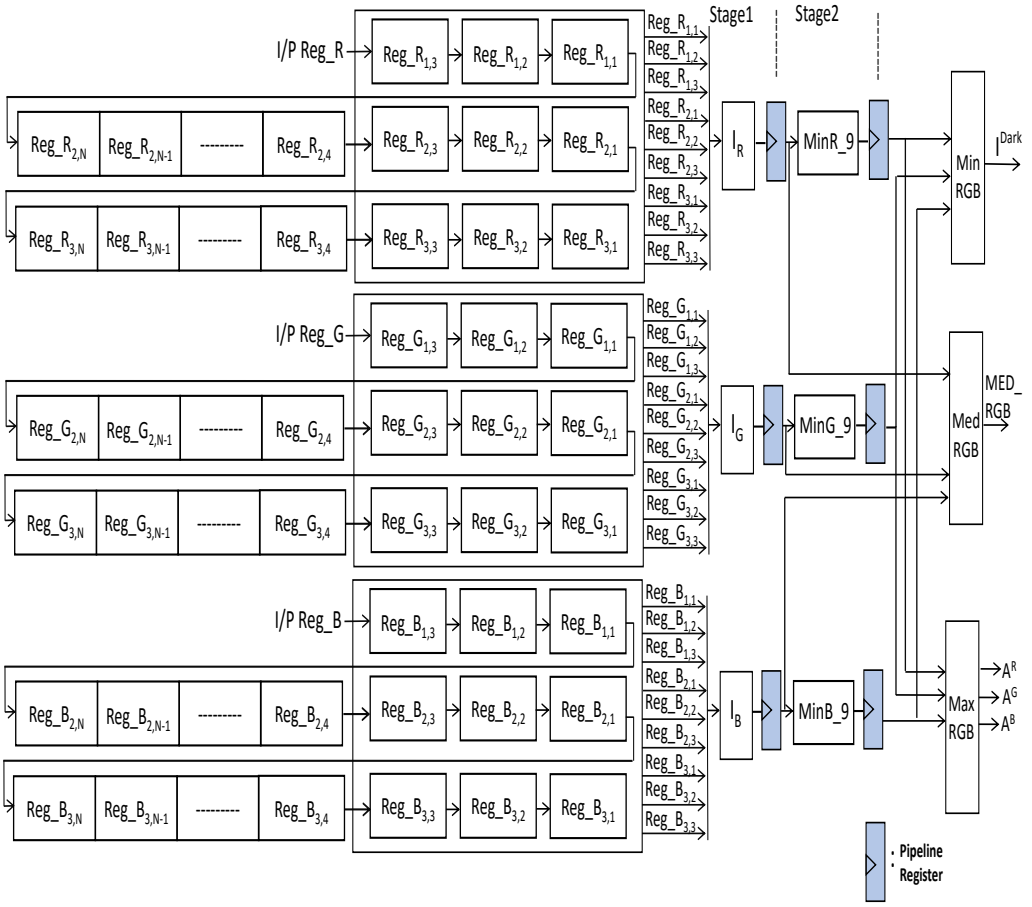


FIGURE 5.18: Architecture of dark channel prior method and atmospheric light estimation

recovered and marked by $J^c$. To improve the performance of our design, the 9-stage pipelined hardware architecture for the fog removal algorithm is presented and implemented as a hardware core. The details of dark channel prior, atmospheric light estimation, transmission estimation, and scene recovery unit are described in the following subsections.

### 5.5.1 Dark Channel Prior

Fig. 5.18 shows the hardware architecture of the dark channel prior method. The first stage is the RB unit which provides nine pixel values of the current $3 \times 3$ window using the smart buffer based sliding window memory architecture. The pixel values are taken row by row. This architecture provides the access to entire pixel neighborhood every clock cycle once the buffer is filled. The complete architecture uses three processing elements in parallel (R, G and B). For storing the two rows of the three color components, three smart buffer based sliding window memories are used. These memories uses First-in First-out (FIFO) shift registers along with 9 registers. In total 6 FIFOs and 27 registers are required for designing sliding window buffer memory. For calculating the dark channel prior for $600 \times 400$ size color images, it takes 1200 $(600 \times 2)$ clock cycles to fill the two rows of image data in buffer memory. After this, with every clock cycle, each color component of the new pixel is moved to its respective computing window. In the second stage, MinR_9, MinG_9 and MinB_9 units determine a minimum value of nine pixels using a $3 \times 3$ minimum filter. The MinRGB unit determines a minimum value among three color channels.

### 5.5.2 Atmospheric Light Estimation

Fig. 5.18 shows the hardware architecture of atmospheric light estimation. Atmospheric light is usually assumed to be the maximum pixel intensity value of the dark channel.

### 5.5.3 Transmission Map Estimation

Fig. 5.19 shows the hardware architecture of refined transmission map. We have used gamma transformation and median filter based approach for enhancing and smoothening the transmission map. The proposed algorithm requires calibration to set the parameters for gamma transformation

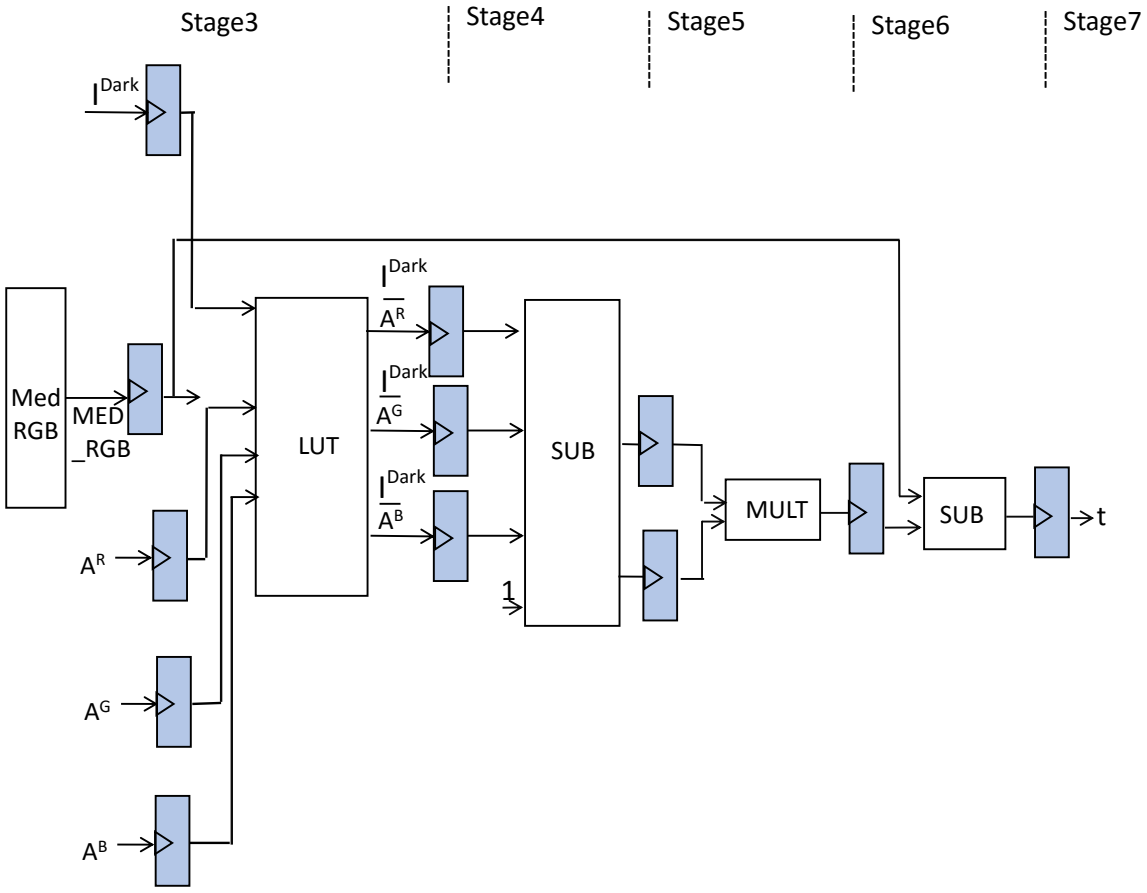


FIGURE 5.19: Architecture of refined transmission map

to attain the best results. The value of $c = 0.1$ and $\gamma = 2$ are chosen because of suitability for low-cost hardware implementation by using multiply operations. In stage 6, MULT unit is used. The MULT unit determines gamma transformation for each color channel. Then SUB unit provides the refined transmission map.

### 5.5.4 Estimating the scene radiance

Fig. 5.20 shows the hardware architecture of scene radiance of the equation (4.3). Where, we used LUT for providing the value of $1/t$. In stage 9, a high quality fog-free image is recovered.

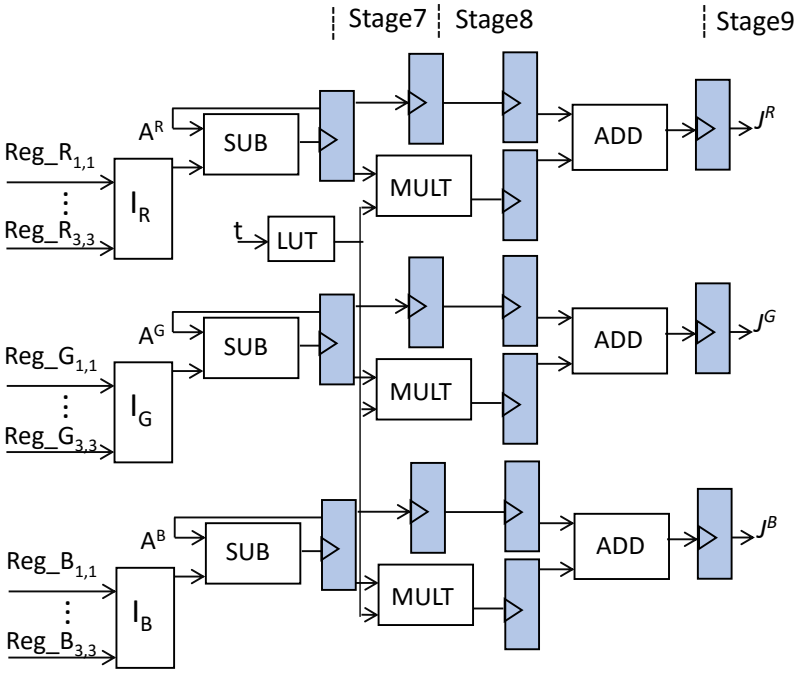


FIGURE 5.20: Architecture of scene radiance

TABLE 5.5: **Comparative Execution Time (Second)**

| **Image size** | **Tan's** | **Fattal** | **He et al.** | **Tarel et al.** | **Shiau et al.** | **Proposed method** |
|---|---|---|---|---|---|---|
| **600x400** | 129.845 | 10.090 | 55.186 | 6.940 | 4.466 | 1.172 |
| **465x384** | 115.095 | 5.314 | 42.050 | 3.328 | 2.936 | 1.028 |
| **265x190** | 90.765 | 2.729 | 5.236 | 1.264 | 1.050 | 0.324 |

## 5.6 Hardware Implementation Results and Performance Comparison

In this section, the results obtained after the simulation of the proposed algorithm are analyzed and compared with the results of Tan [27], Fattal [28], He et al. [30], Tarel et al. [32] and Shiau et al. [44]. The simulations were done using MATLAB R2012b (8.0.0.783) 64-bit and the algorithms were processed on Intel (R) Core (TM) i5-3337U CPU @ 1.80GHz with 8Gb RAM. From the Table 5.5, it can be noted that the proposed method takes least execution time for image with different dimension up to $600 \times 400$ pixels. The 9-stage hardware architecture for

TABLE 5.6: **Comparison of FPGA Implementation Results**

| **FPGA Device (Altera Stratix EP1S10F780C6)** | **Total Logic Elements** | **Filp Flops** | **Frequency (MHz)** | **Throughput (Mpixels/s)** |
|---|---|---|---|---|
| **Shiau et al. method** | 1607 | 454 | 58.43 | 58.43 |
| **Proposed Method** | 1586 | 452 | 75.39 | 75.39 |
| **Percentage Improvement(%)** | 1.306 | 0.440 | 29.026 | 29.026 |

TABLE 5.7: **Comparison of ASIC Implementation Results**

| **ASIC Library** | **Gate Counts** | **Frequency (MHz)** | **Throughput (Mpixels/s)** |
|---|---|---|---|
| **TSMC's 0.13-$\mu$m (Shiau et al. method)** | 12816 | 200 | 200 |
| **UMC 65-nm (Proposed Method)** | 10401 | 200 | 200 |

proposed method was implemented on the Altera Stratix EP1S10F780C6 platform using VHDL for verification. The main advantage of our design is in reduction of the number of filters in comparison to Shiau et al. [44] method. This design does not require mean filter and uses only one edge preserving filter for refining the transmission map. Table 5.6 shows the comparison results of hardware implementation using FPGA of Shiau et al. [44] method and our method. The proposed implementation shows improvement in performance by 29% compared with Shiau et al [44] with slightly less hardware resource utilization. Furthermore, the architecture was also synthesized for ASIC implementation using SYNOPSYS Design Vision with UMC 65-nm cell library. From post synthesis results, the cell count, power consumption at 200MHz frequency of operation with 1.8-V supply voltage are obtained and noted in Table 5.7.

As it works with a clock period of 5 ns, the circuit can also achieve a throughput rate of 200 Mpixels/s. The gate count comparison shows, the proposed implementation uses almost 18% less gates than Shiau et al [44] for ASIC implementation. This ASIC core is operated at different reduced clock frequencies and the power consumption are noted in Table 5.8. This core can be used for low power application with reduced speed. Figs. 5.21 - 5.23 show the simulation

TABLE 5.8: **Synthesis Results of Proposed Method and Shiau et al. method**

| **Clock Period (ns)** | **Throughput (Mpixels/s)** | **Power Consumption (mW) (Shiau et al. method)** | **Power Consumption (mW) (Proposed method)** | **EPM (pJ) (Shiau et al. method)** | **EPM (pJ) (Proposed method)** |
|---|---|---|---|---|---|
| 5 | 200 | 11.9 | 1.91 | 59.5 | 9.55 |
| 10 | 100 | 4.87 | 1.17 | 48.7 | 11.7 |
| 20 | 50 | 2.41 | 0.76 | 48.2 | 15.2 |
| 40 | 25 | 1.15 | 0.59 | 46 | 23.6 |
| 80 | 12.5 | 0.58 | 0.49 | 46.4 | 39.2 |

Energy per Mpixel (EPM)=Power Consumption x Clock Period


FIGURE 5.21: (a) Original image (b) Tan's method (c) Tarel et al. method (d) Shiau et al. and (e) Proposed method


FIGURE 5.22: (a) Original image (b) Fattal method (c) Tarel et al. method (d) Shiau et al. method and (e) Proposed method

results compared with Tan [27], Fattal [28], He et al. [30], Tarel et al. [32] and Shiau et al. [44] methods, respectively. It can be observed that the recovered image from the proposed method does not contain any halo artifacts. It can be seen that the proposed method gives comparable results to existing state-of-the-art approaches by using the least execution time.


FIGURE 5.23: (a) Original image (b) He et al. method (c) Tarel et al. method (d) Shiau et al. method and (e) Proposed method

## 5.7 Conclusion

In this chapter, we have presented a better, efficient and faster image restoration method. This proposed method makes use of gamma transformation and median filter to refine and smoothening of the transmission map. The advantage can be explicitly notable in contrast which is relatively high and the percentage number of saturated pixels is less in comparison with other methods. The proposed algorithm being faster and producing outputs with enhanced contrast and lesser percentage of saturated pixels, is thus qualitatively and quantitatively better than the previous methods. Our method can acquire comparable results with previous methods as well as at the least execution time. As proof-of-concept of this method being suitable for real time image/video application, we designed a 9-stage pipelined hardware accelerator implemented using FPGA for low-cost high-performance fog removal. This method can be profitably applied to real-time systems like surveillance, intelligent vehicles, remote sensing and terrain classification and so on.

# Chapter 6

# Conclusions and Scope for Future Work

Current vision systems are performing well in normal weather conditions. However, these systems are not able to handle problems produced by bad weather conditions. Recently, the video/image dehazing and defogging algorithms have received much attention and are widely used in driving and military fields, such as vehicle driving, remote sensing, target detection, and traffic surveillance. These deweathering algorithms are physically sound and produce qualitatively better results. But, these algorithms are concerned about the dehazing and defogging quality rather than the real-time processing. For video deweathering, persuasiveness and real-time processing are equally essential. It is difficult to concurrently ensure better dehazing and defogging results and real-time processing. In this thesis, we addressed these issues and presented a different method based on enhancement and restoration, which maintain the dehazing and defogging image/video quality as well as real-time deweathering of image/video.

## 6.1 Specific Contributions of the Research Work

We summarize the main contributions of this thesis in the following.

Based on the review of literature on real-time image and video deweathering, the current research work presents a new methodology for removing haze and fog from image/video. In chapter 3, we propose an approach of gamma correction using look-up-table method to obtain higher contrast images. The use of look-up-table (LUT) in these images makes our approach appreciably faster. We extend the static image to real-time video deweathering. By applying our method, the processing rate is greatly improved and color distortion is avoided. Experimental results show the effectiveness and robustness of our proposed method.

We presented in chapter 4 a new approach for restoring the scene radiance of foggy and hazy image/ video based on estimation and refinement of atmospheric light and transmission map. In this chapter, atmospheric light is estimated using a thresholding method. We estimated the atmospheric light for each channel. Next, transmission map is estimated and refined by dark channel prior and median dark channel prior method. Median dark channel prior method is used to reduce the overlaps of edges and hence an artifact and fog free video has been achieved. Experiments show that it is advantageous in real-time deweathering, in terms of both quality and efficacy.

In chapter 5, we propose a novel and simple restoration-based approach for fog and haze removal. The coarse transmission map is refined using Gamma transformation and Median filter. Our results excel previous visibility restoration approaches in terms of processing time. To meet the requirement of real-time applications, a 9-stage pipelined hardware accelerator has been implemented with field programmable gate arrays (FPGA) which compares favorably with existing methods of state-of-the-art and has lower computational complexity. The proposed algorithm, due to its speed, compatibility with both color and gray images and the ability to

improve visibility will be effective in machine vision systems ranging from tracking and navigation, surveillance, consumer electronics, intelligent vehicles to remote sensing.

## 6.2 Future Scope

The work presented in this thesis is suitable for static bad weather condition in clear and bright conditions. Future scope lies in adapting this work for low light conditions and dynamic weather conditions. Dynamic weather conditions such as rain and snow degrade vision systems. Mathematical modeling is not robust for dynamic weather condition. Static weather algorithms do not work for dynamic weather conditions. This is still a challenging problem to solve. We also believe that there is enough scope for hardware implementation for real-time dehazing and defogging. In this thesis, we did a hardware implementation for achieving the real-time scenario of deweathering the image/video. In the future, work can be done on optimizing hardware for real-time image/video dehazing and defogging.

# Bibliography


[1] Srinivasa G Narasimhan and Shree K Nayar. Vision and the atmosphere. *International Journal of Computer Vision*, 48(3):233–254, 2002.

[2] Srinivasa G Narasimhan and Shree K Nayar. Chromatic framework for vision in bad weather. In *Computer Vision and Pattern Recognition, 2000. Proceedings. IEEE Conference on*, volume 1, pages 598–605. IEEE, 2000.

[3] Kenneth T Whitby. The physical characteristics of sulfur aerosols. *Atmospheric Environment (1967)*, 12(1):135–159, 1978.

[4] J. N. Myers. *FOG*. 1968. Scientific American, pp. 75-82.

[5] Gordon Manley. Bj mason. clouds, rain and rainmaking. cambridge, university press, 1962. 149 p., illus. *Journal of Glaciology*, 4:821–822, 1963.

[6] W. E. K. middleton. Vision through the atmosphere. Univ. of toronto press, 1952.

[7] Tae Keun Kim, Joon Ki Paik, and Bong Soon Kang. Contrast enhancement system using spatially adaptive histogram equalization with temporal filtering. *IEEE Transactions on Consumer Electronics*, 44(1):82–87, 1998.

[8] J Alex Stark. Adaptive image contrast enhancement using generalizations of histogram equalization. *Image Processing, IEEE Transactions on*, 9(5):889–896, 2000.

[9] Joung-Youn Kim, Lee-Sup Kim, and Seung-Ho Hwang. An advanced contrast enhancement using partially overlapped sub-block histogram equalization. *Circuits and Systems for Video Technology, IEEE Transactions on*, 11(4):475–484, 2001.

[10] Srinivasa G Narasimhan and Shree K Nayar. Removing weather effects from monochrome images. In *Computer Vision and Pattern Recognition, 2001. CVPR 2001. Proceedings of the 2001 IEEE Computer Society Conference on, vol. 2, pp. II–186*. IEEE, 2001.

[11] Srinivasa G Narasimhan and Shree K Nayar. Contrast restoration of weather degraded images. *Pattern Analysis and Machine Intelligence, IEEE Transactions on*, 25(6):713–724, 2003.

[12] NS Kopeika. General wavelength dependence of imaging through the atmosphere. *Applied Optics*, 20(9):1532–1536, 1981.

[13] Marcel Minnaert. *The nature of light and colour in the open air*. Courier Corporation, 2013.

[14] Earl J McCartney. Optics of the atmosphere: scattering by molecules and particles. *New York, John Wiley and Sons*, vol. 1, 1976.

[15] R. Gonzalez, R. Woods. *Digital Image Processing*. Prentice-Hall, 2007.

[16] Stephen M Pizer, E Philip Amburn, John D Austin, Robert Cromartie, Ari Geselowitz, Trey Greer, Bart ter Haar Romeny, John B Zimmerman, and Karel Zuiderveld. Adaptive histogram equalization and its variations. *Computer vision, graphics, and image processing*, 39(3):355–368, 1987.

[17] Karel Zuiderveld. Contrast limited adaptive histogram equalization. In *Graphics gems IV*. Academic Press Professional, pp. 474–485, 1994.

[18] Jeffrey J Rodriguez and Christopher C Yang. High-resolution histogram modification of color images. *Graphical models and image processing*, 57(5):432–440, 1995.

[19] Iyad F Jafar and Khalid A Darabkh. A modified unsharp-masking technique for image contrast enhancement. In *Systems, Signals and Devices (SSD),8th International Multi-Conference on, pp. 1–6*. IEEE, 2011.

[20] Daniel J Jobson, Zia-ur Rahman, and Glenn A Woodell. Properties and performance of a center/surround retinex. *Image Processing, IEEE Transactions on*, 6(3):451–462, 1997.

[21] Glenn Hines, Zia-ur Rahman, Daniel Jobson, and Glenn Woodell. Single-scale retinex using digital signal processors. 2005.

[22] Zia-ur Rahman, Daniel J Jobson, and Glenn A Woodell. Retinex processing for automatic image enhancement. *Journal of Electronic Imaging*, 13(1):100–110, 2004.

[23] Jean-Philippe Tarel, Nicolas Hautiere, Aurélien Cord, Dominique Gruyer, and Houssam Halmaoui. Improved visibility of road scene images under heterogeneous fog. In *Intelligent Vehicles Symposium (IV), 2010 IEEE, pp. 478–485*. IEEE, 2010.

[24] Paul Scheunders. A multivalued image wavelet representation based on multiscale fundamental forms. *Image Processing, IEEE Transactions on*, 11(5):568–575, 2002.

[25] Lynne L Grewe and Richard R Brooks. Atmospheric attenuation reduction through multisensor fusion. In *Aerospace/Defense Sensing and Controls, pp. 102–109*. International Society for Optics and Photonics, 1998.

[26] Yoav Y Schechner, Srinivasa G Narasimhan, and Shree K Nayar. Instant dehazing of images using polarization. In *Computer Vision and Pattern Recognition (CVPR), Proceedings of the 2001 IEEE Computer Society Conference on, vol. 1, pp. I–325*. IEEE, 2001.

[27] Robby T Tan. Visibility in bad weather from a single image. In *Computer Vision and Pattern Recognition (CVPR), IEEE Conference on, pp. 1–8*. IEEE, 2008.

[28] Raanan Fattal. Single image dehazing. In *ACM transactions on graphics (TOG), 27(3):72*. ACM, 2008.

[29] Kaiming He, Jian Sun, and Xiaoou Tang. Single image haze removal using dark channel prior. In *Computer Vision and Pattern Recognition, Proceedings. IEEE Conference on, pp. 1956–1963*. IEEE, 2009.

[30] Kaiming He, Jian Sun, and Xiaoou Tang. Single image haze removal using dark channel prior. *Pattern Analysis and Machine Intelligence, IEEE Transactions on, vol. 22(12), pp. 2341–2353*, 2011.

[31] Jisha John and M Wilscy. Enhancement of weather degraded video sequences using wavelet fusion. In *Cybernetic Intelligent Systems, 7th IEEE International Conference on, pp. 1–6*. IEEE, 2008.

[32] Jean-Philippe Tarel and Nicolas Hautiere. Fast visibility restoration from a single color or gray level image. In *Computer Vision, IEEE 12th International Conference on, pp. 2201–2208*. IEEE, 2009.

[33] Zhiyuan Xu, Xiaoming Liu, and Xiaonan Chen. Fog removal from video sequences using contrast limited adaptive histogram equalization. In *Computational Intelligence and Software Engineering (CiSE),International Conference on, pp. 1–4*. IEEE, 2009.

[34] Xingyong Lv, Wenbin Chen, and I-fan Shen. Real-time dehazing for image and video. In *Computer Graphics and Applications (PG), 18th Pacific Conference on, pp. 62–69*. IEEE, 2010.

[35] Kaiming He, Jian Sun, and Xiaoou Tang. Guided image filtering. In *Computer Vision–ECCV 2010, pp. 1–14*. Springer, 2010.

[36] Chunxia Xiao and Jiajia Gan. Fast image dehazing using guided joint bilateral filter. *The Visual Computer*, 28(6-8):713–721, 2012.

[37] Carlo Tomasi and Roberto Manduchi. Bilateral filtering for gray and color images. In *Computer Vision, Sixth International Conference on, pp. 839–846*. IEEE, 1998.

[38] Ke Zhang, Jiangbo Lu, Gauthier Lafruit, Rudy Lauwereins, and Luc Van Gool. A cross-based filter for fast edge-preserving smoothing. In *IS&T/SPIE Electronic Imaging, pp. 78710H–78710H*. International Society for Optics and Photonics, 2011.

[39] Zheqi Lin and Xuansheng Wang. Dehazing for image and video using guided filter. *Open Journal of Applied Sciences*, 2(04):123, 2013.

[40] Jing Xu, Wei Zhao, Peng Liu, and Xianglong Tang. Removing rain and snow in a single image using guided filter. In *Computer Science and Automation Engineering (CSAE), IEEE International Conference on, vol. 2, pp. 304–307*. IEEE, 2012.

[41] Kaiming He, Jian Sun, and Xiaoou Tang. Guided image filtering. *Pattern Analysis and Machine Intelligence, IEEE Transactions on*, 35(6):1397–1409, 2013.

[42] Y Xiong, H Yan, and C Yu. Algorithm of removing thin cloud-fog cover from single remote sensing image. *J. Inf. Comput. Sci*, 11(3):817–824, 2014.

[43] Jin-Hwan Kim, Won-Dong Jang, Jae-Young Sim, and Chang-Su Kim. Optimized contrast enhancement for real-time image and video dehazing. *Journal of Visual Communication and Image Representation, vol. 24(3), pp. 410–425*, 2013.

[44] Yeu-Horng Shiau, Hung-Yu Yang, Pei-Yin Chen, and Ya-Zhu Chuang. Hardware implementation of a fast and efficient haze removal method. *Circuits and Systems for Video Technology, IEEE Transactions on*, 23(8):1369–1374, 2013.

[45] Nicolas Hautiere, Jean-Philippe Tarel, Didier Aubert, Eric Dumont, et al. Blind contrast enhancement assessment by gradient ratioing at visible edges. *Image Analysis & Stereology Journal, vol. 27(2), pp. 87–95*, 2008.

[46] Simon Perreault and Patrick Hébert. Median filtering in constant time. *IEEE transactions on image processing*, 16(9):2389–2394, 2007.

[47] Mohammad Abdullah-Al-Wadud, Md Hasanul Kabir, M Dewan, and Oksam Chae. A dynamic histogram equalization for image contrast enhancement. *Consumer Electronics, IEEE Transactions on*, 53(2):593–600, 2007.

[48] Andrea Polesel, Giovanni Ramponi, V John Mathews, et al. Image enhancement via adaptive unsharp masking. *IEEE transactions on image processing*, 9(3):505–510, 2000.

[49] Daniel J Jobson, Zia-ur Rahman, and Glenn A Woodell. A multiscale retinex for bridging the gap between color images and the human observation of scenes. *Image Processing, IEEE Transactions on*, 6(7):965–976, 1997.

[50] Bin-Na Yu, Byung-Sung Kim, and Kwae-Hi Lee. Visibility enhancement based real–time retinex for diverse environments. In *Signal Image Technology and Internet Based Systems (SITIS), Eighth International Conference on, pp. 72–79*. IEEE, 2012.

[51] Zhongliang Wang and Yan Feng. Fast single haze image enhancement. *Computers & Electrical Engineering*, 40(3):785–795, 2014.

[52] http://mcl.korea.ac.kr/projects/dehazing/.

[53] Johannes Kopf, Boris Neubert, Billy Chen, Michael Cohen, Daniel Cohen-Or, Oliver Deussen, Matt Uyttendaele, and Dani Lischinski. Deep photo: Model-based photograph enhancement and viewing. In *ACM Transactions on Graphics (TOG), vol. 27(5), pp. 116*. ACM, 2008.

[54] Kristofor Gibson, Dung Vo, and Truong Nguyen. An investigation in dehazing compressed images and video. In *IEEE OCEANS, pp. 1–8*, 2010.

[55] Yuan-Kai Wang and Ching-Tang Fan. Single image defogging by multiscale depth fusion. *Image Processing, IEEE Transactions on*, 23(11):4826–4837, 2014.

[56] Louis Kratz and Ko Nishino. Factorizing scene albedo and depth from a single foggy image. In *Computer Vision, 12th International Conference on, pp. 1701–1708*. IEEE, 2009.

[57] Ko Nishino, Louis Kratz, and Stephen Lombardi. Bayesian defogging. *International journal of computer vision*, 98(3):263–278, 2012.

[58] Jiawan Zhang, Liang Li, Guoqiang Yang, Yi Zhang, and Jizhou Sun. Local albedo-insensitive single image dehazing. *The Visual Computer*, 26(6-8):761–768, 2010.

[59] Arvind K Tripathi and Saibal Mukhopadhyay. Single image fog removal using bilateral filter. In *Signal Processing, Computing and Control (ISPCC), IEEE International Conference on, pp. 1–6*. IEEE, 2012.

[60] Bin Xie, Fan Guo, and Zixing Cai. Improved single image dehazing using dark channel prior and multi-scale retinex. In *Intelligent System Design and Engineering Application (ISDEA), 2010 International Conference on, vol. 1, pp. 848–851*. IEEE, 2010.

[61] Chia-Hung Yeh, Li-Wei Kang, Ming-Sui Lee, and Cheng-Yang Lin. Haze effect removal from image via haze density estimation in optical model. *Optics express*, 21(22):27127–27141, 2013.

[62] Haoran Xu, Jianming Guo, Qing Liu, and Lingli Ye. Fast image dehazing using improved dark channel prior. In *Information Science and Technology (ICIST), International Conference on, pp. 663–667*. IEEE, 2012.

[63] Shuai Fang, Jiqing Zhan, Yang Cao, and Ruizhong Rao. Improved single image dehazing using segmentation. In *Image Processing (ICIP), 17th IEEE International Conference on, pp. 3589–3592*. IEEE, 2010.

[64] Gaofeng Meng, Ying Wang, Jiangyong Duan, Shiming Xiang, and Chunhong Pan. Efficient image dehazing with boundary constraint and contextual regularization. In *Proceedings of the IEEE International Conference on Computer Vision, pp. 617–624*, 2013.

[65] Ketan Tang, Jianchao Yang, and Jue Wang. Investigating haze-relevant features in a learning framework for image dehazing. In *Computer Vision and Pattern Recognition (CVPR), IEEE Conference on, pp. 2995–3002*. IEEE, 2014.

[66] Leo Breiman. Random forests. *Machine learning*, 45(1):5–32, 2001.

[67] Codruta O Ancuti and Cosmin Ancuti. Single image dehazing by multi-scale fusion. *Image Processing, IEEE Transactions on*, 22(8):3271–3282, 2013.

[68] Shih-Chia Huang, Bo-Hao Chen, and Wei-Jheng Wang. Visibility restoration of single hazy images captured in real-world weather conditions. *Circuits and Systems for Video Technology, IEEE Transactions on*, 24(10):1814–1824, 2014.

[69] Prasun Choudhury and Jack Tumblin. The trilateral filter for high contrast images and meshes. In *ACM SIGGRAPH 2005 Courses, pp. 5*. ACM, 2005.

[70] Abhishek Kumar Tripathi and Sudipta Mukhopadhyay. Removal of fog from images: A review. *IETE Technical Review*, 29(2):148–156, 2012.

# List of Publications

## Journal Publications

- Kumari, Apurva, and Subhendu Kumar Sahoo."Fast single image and video deweathering using look-up-table approach." AEU-International Journal of Electronics and Communications 69, no. 12 (2015): 1773-1782.

- Kumari, Apurva, and Subhendu Kumar Sahoo."Real time image and video deweathering: The future prospects and possibilities." Optik-International Journal for Light and Electron Optics 127, no. 2 (2016): 829-839.

- Kumari, Apurva, Philip Joseph Thomas, and Subhendu Kumar Sahoo."Fast and Efficient Visibility Restoration Technique for Single Image Dehazing and Defogging." (under review in Computers & Electrical Engineering)

- Kumari, Apurva, Subhendu Kumar Sahoo, Pramod K. Meher, and Ravi Saini."Hardware implementation of a Single Image Fog Removal Using Gamma transformation and Median filtering." (under review in IEEE Transactions on Circuits and Systems for Video Technology)

## Conference Publications

- Kumari, Apurva, Philip Joseph Thomas, and Subhendu Kumar Sahoo."Single image fog removal using gamma transformation and median filtering." In India Conference (INDICON), 2014 Annual IEEE, pp. 1-5, 2014 Dec 11, Pune.

- Kumari, Apurva, Sidharth Sahdev, and Subhendu Kumar Sahoo."Improved single image and video dehazing using morphological operation." In VLSI Systems, Architecture, Technology and Applications (VLSI-SATA), 2015 International Conference on, pp. 1-5. IEEE, 2015 Jan 8, Banglore.

- Kumari, Apurva, and Subhendu Kumar Sahoo."Real Time Visibility Enhancement for Single Image Haze Removal." Procedia Computer Science 54 (2015): 501-507.

- Kumari, Apurva, Himaja Kodati, and Subhendu Kumar Sahoo."Fast and Effecient Contrast Enhancement For Real time Video Dehazing and Defogging" In 2015 IEEE Workshop on Computational Intelligence: Theories, Applications and Future Directions (WCI) 2015 Dec 14, pp. 1-5, IIT Kanpur.

# Biography

## Candidate Biography

Apurva Kumari, received her M. Tech degree in VLSI Design from Banasthali University, Rajasthan, India in 2011. She has been working as a research scholar at BITS Pilani, Hyderabad Campus from 2013-2016 under the supervision of Prof. Subhendu Kumar Sahoo. Her research interests focus on Image and Video processing.

## Supervisor Biography

Subhendu Kumar Sahoo completed his B.E. in Electronics and telecommunication engineering from Utkal University, Orissa, India in the year 1994 with honors securing fifth position in the university. He obtained his M.E. in Electronic Systems and Communication from R.E.C.(NIT) Rourkela in 1998. He received the Ph. D. degree in electrical engineering from Birla Institute of Technology and Science, Pilani, in 2006. He was working as a faculty in Electrical and Electronics Engineering department from 2009 till 2011. Presently he is working as associate professor in Birla Institute of Technology and Science, Pilani Hyderabad campus. His areas of research are high performance arithmetic circuits and VLSI circuits for digital signal processing and image processing applications.